

Hall A Annual Report 2013

arXiv:1402.7028v1 [nucl-ex] 27 Feb 2014



Edited by Mark M Dalton

Hall A Annual Report 2013

M.M. Dalton¹, K. Allada², K. Aniol³, W. Boeglin⁴, E. Chudakov¹, M. Cummings⁵,
D. Flay⁶, M. Friedman⁷, O. Glamazdin⁸, J. Gomez¹, C. Keppel¹, H.P. Khanal⁴,
R. Lindgren⁹, E. Long¹⁰, R. Michaels¹, M. Mihovilović¹¹, C. Muñoz Camacho¹²,
R. Pomatsalyuk⁸, S. Riordan¹³, S. Širca¹¹, C. Smith⁹, P. Solvignon^{1,10}, N.F. Sparveris⁶,
V. Vereshchaka⁸, X. Yan¹⁴, Z. Ye⁵, Y.X. Zhao¹⁴ and the Jefferson Lab Hall A
Collaboration¹

¹Thomas Jefferson National Accelerator Facility, Newport News, VA 23606, USA

²Massachusetts Institute of Technology, Cambridge, MA 02139, USA

³California State University Los Angeles, Los Angeles, CA 90032, USA

⁴Florida International University, Miami, FL 33199, USA

⁵College of William and Mary, Williamsburg, VA 23187, USA

⁶Temple University, Philadelphia, PA 19122

⁷Racah Institute of Physics, Hebrew University of Jerusalem, Givat Ram 91904, Israel

⁸National Science Center Kharkov Institute of Physics and Technology, Kharkov 61108,
Ukraine

⁹University of Virginia, Charlottesville, VA 22901, USA

¹⁰University of New Hampshire, Durham, NH 03824, USA

¹¹University of Ljubljana, SI-1000 Ljubljana, Slovenia

¹²Institut de Physique Nucleaire d'Orsay, IN2P3, BP 1, 91406 Orsay, France

¹³University of Massachusetts, Amherst, MA 01003, USA

¹⁴University of Science and Technology of China, Hefei 230026, People's Republic of China

October 10, 2018

Contents

1	Introduction	7
2	General Hall Developments	8
2.1	Status of the Hall A Møller Polarimeter DAQ	8
2.1.1	Møller polarimeter	8
2.1.2	The old DAQ	9
2.1.3	The new DAQ based on FADC	11
2.1.4	Comparison of two DAQs results	13
2.1.5	Conclusion	13
2.2	Compton DAQ	16
3	Summaries of Experimental Activities	18
3.1	E01-020: (e, e'p) Studies of the Deuteron at High Q^2	18
3.1.1	Introduction	18
3.1.2	Experimental Overview	18
3.1.3	Analysis Status	18
3.2	E04-007: Precision Measurements of Electroproduction of π^0 near Threshold	23
3.2.1	Introduction	23
3.2.2	Analysis Status	23
3.3	E05-102: Measurement of A'_x and A'_z asymmetries in the quasi-elastic ${}^3\text{He}(\vec{e}, e'd)$ reaction	25
3.4	E06-010: Transversity	28
3.4.1	Introduction	28
3.4.2	SSA in Inclusive Hadron Production	29
3.4.3	Pretzelosity Asymmetry	29
3.4.4	SSA of Kaon in SIDIS	30
3.4.5	Unpolarized SIDIS Cross-Section	32
3.5	E06-014: A Precision Measurement of d_2^n : Probing the Lorentz Color Force	34
3.5.1	Physics Motivation	34
3.5.2	The Experiment	35
3.5.3	Data Analysis Progress	37
3.5.4	Preliminary Physics Results	40
3.5.5	Current and Future Work	43
3.6	E07-007 and E08-025: Deeply Virtual Compton Scattering	46
3.6.1	Introduction	46
3.6.2	Status of the analysis	46
3.7	E08-005: Target Single-Spin Asymmetry A_y^0 in the Quasi-Elastic ${}^3\text{He}^\uparrow(e, e'n)$ Reaction	49
3.7.1	Progress of ${}^3\text{He}(e, e'n) A_y^0$	49
3.8	E08-007-II: G_E^p at Low Q^2	52
3.8.1	Motivation	52
3.8.2	The Experiment	52
3.8.3	Experimental Progress	52
3.9	E08-009: ${}^4\text{He}(e, e'p){}^3\text{H}$ at $x_b = 1.24$	57
3.9.1	Experimental Conditions	57
3.9.2	Motivation	57
3.9.3	E_{miss} Spectra	57
3.9.4	Simulations	57
3.9.5	SRC target behavior	58
3.9.6	Cross Section Results and Theory	59
3.10	E08-010: Coulomb quadrupole amplitude in $\text{N} \rightarrow \Delta$ at low Q^2	65
3.10.1	Introduction	65
3.10.2	The Experiment	66
3.11	E08-011: \vec{e} - ${}^2\text{H}$ Parity Violating Deep Inelastic Scattering (PVDIS) at CEBAF 6 GeV	70

3.12	E08-014: The $x > 2$ experiment	71
3.12.1	Motivations	71
3.12.2	Analysis status	71
3.13	E08-027: g_2^p	73
3.13.1	Motivation	73
3.13.2	The Experiment	73
3.13.3	Status of Analysis	74
3.14	The Super Bigbite Spectrometer	77
3.14.1	Overview	77
3.14.2	Organization	77
3.14.3	Instrumentation Progress	78
4	Publications	80
5	Theses	80
6	Hall A Collaboration Member List, 2013	81

List of Figures

1	Layout of the Hall A Møller polarimeter. a) side view, b) top view.	8
2	Scheme of the old Møller DAQ.	9
3	Diagram of programmable logic unit based on module CAEN V1495.	10
4	New Møller polarimeter DAQ based on FADC.	11
5	Flash ADC module.	12
6	Data from on-line monitoring program.	13
7	An example of data trigger (pile-up events).	14
8	Result of asymmetry measurement with two Møller polarimeter DAQs.	15
9	Proposed upgrade of the Compton DAQ	17
10	The momentum distribution at low $Q^2 = 0.8$ (GeV/c) ² for different recoil angles θ_{nq}	19
11	The momentum distribution at high $Q^2 = 2.1$ (GeV/c) ² for different recoil angles θ_{nq}	20
12	Comparison of the experimental momentum distributions for $Q^2 = 0.8$ (green), 2.1 (red), and 3.5 (GeV/c) ² [1] (blue) for different values of θ_{nq}	20
13	R as a function of θ_{nq} for $Q^2 = 0.8$ (GeV/c) ² . Red: $p_m = 0.2$ GeV/c , blue: $p_m = 0.4$ GeV/c and magenta: $p_m = 0.5$ GeV/c . The corresponding sold lines represent calculations using Laget's model including FSI	21
14	Like Fig. 13 for $Q^2 = 2.1$ (GeV/c) ²	21
15	E05102: Deviations of p_{miss} in bins used for theory averaging.	25
16	E05102: Averaging of the theoretical asymmetries.	26
17	E06-010: Transverse SSA in inclusive hadron (π^\pm , K^\pm , p) production on a ³ He target.	29
18	E06-010: Transverse SSA (A_N) of inclusive pions as function of p_T for 3He target and extracted for neutron.	30
19	E06-010: The pretzelosity asymmetries of pions for 3He target and extracted for neutron.	30
20	E06-010: Coincidence ToF spectrum between the BigBite and the HRS in E06-010 experiment.	31
21	E06-010: Preliminary results of Collins and Sivers moments on ³ He for kaon electroproduction.	32
22	World data for d_2^2 as a function of Q^2	35
23	Current data for A_1^n , $\Delta d/d$ and $\Delta u/u$	36
24	The E06-014 kinematic coverage in Q^2 and x	37
25	The ³ He Born cross sections.	38
26	Our model of $\Delta\sigma_{\parallel,\perp}$ as compared to JLab E94-010 data.	40
27	The size of the radiative correction on the asymmetries.	41
28	The Born asymmetries for $E = 4.74$ GeV and $E = 5.89$ GeV.	42
29	Preliminary A_1^{3He} for $E = 4.74$ and 5.89 GeV compared to world data and selected models	42
30	Preliminary g_1 and g_2 on ³ He for $E = 4.74$ and 5.89 GeV compared to world data and various models.	43
31	DIS cross section as a function of run number.	46
32	E07-007: DVCS off the proton missing mass squared.	47
33	E07-007: Final DVCS counts and comparison with Monte Carlo.	48
34	E07-025: DVCS off the deuteron missing mass squared.	48
35	A_y^0 calculated on a run-by-run basis at $Q^2 = 0.46$ (GeV/c) ²	49
36	The ³ He [†] (e, e') target single-spin asymmetry was compared to Y. Zhang's analysis of the same dataset. Calculations were done using a) the original analysis script and b) the corrected analysis script, which accounted for minor corrections to the charge and live-time calculations.	50
37	Run-by-run analysis of A_y^0 for Q^2 of a) 0.13 (GeV/c) ² , b) 0.46 (GeV/c) ² , and c) 0.95 (GeV/c) ²	51
38	Background subtraction procedure, 1.7 GeV left arm data. Top-left is the dilution run, and top-right is the production run. The black line represents the fpX limit used for normalization. The separation between hydrogen elastic peak and other events is not clear enough. The bottom-left is the subtraction after normalizing, and the bottom-right is the same in log scale. Two different cuts are show, and used for consistency purposes	53
39	Monte-Carlo simulation of production data at 2.2 GeV (left arm), compared to experimental data. Agreement is not yet good enough for dilution analysis.	53

40	An example for physical asymmetry extraction. This data is for the left arm, 1.7 GeV runs. The uncertainty is extracted by the fit, and the χ^2 values are listed in Table 3.	54
41	E08009: E_{miss} defined by SKxceb.emiss vs y_{tgt} for the 0.153GeV/c kinematic setting.. . . .	58
42	E08009: E_{miss} corrected for the y_{tgt} slope for the 0.153GeV/c kinematic setting.	59
43	E08009: E_{miss} for the 0.153GeV/c kinematic setting.	59
44	E08009: E_{miss} for the 0.353GeV/c kinematic setting.	60
45	E08009: E_{miss} for the 0.500GeV/c kinematic setting.	60
46	E08009: GEANT simulations, Gaussian broadened, of the triton missing energy spectrum. The black curve is for $\sigma = 1. \times 10^{-4}$ and the red curve is offset to match the data with $\sigma = 6.53 \times 10^{-4}$	61
47	E08009: GEANT simulation(black curve) and data(red curve) for the 0.153GeV/c kinematic setting.	61
48	E08009: GEANT simulation(black curve) and data(orange curve) for the 0.353GeV/c kinematic setting.	62
49	E08009: GEANT missing momentum spectra for 0.153GeV/c(black) and 0.353GeV/c(red) as determined at the spectrometer apertures.	62
50	E08009: Computational Fluid Dynamic calculation [6] for the SRC target. drho is the loss in percent of density from the input fluid.	63
51	E08009: Normalized counts per Coulomb(vertical axis) along the beam's path for 4 different beam currents.	63
52	E08009: Cross sections for 0.153GeV/c(closed dots), 0.353GeV/c(open dots) and Madrid Theory(asterisks) [2].	64
53	The effect of the pionic cloud to the resonant amplitudes as predicted by the Sato-Lee calculation [22]. Solid line includes the pion cloud contribution while the dashed line neglects the pion cloud effect.	66
54	Left panel: The missing mass spectrum for the reconstructed (undetected) pion after the subtraction of accidentals. Right panel: Raw and corrected coincidence Time of Flight spectrum; an excellent timing resolution of 1.6 ns has been achieved after the ToF corrections.	66
55	The measured cross section is presented for the parallel cross section measurement at $Q^2 = 0.125 (GeV/c)^2$	67
56	The CMR at the low momentum transfer region. The projected E08-010 uncertainties are presented along with the world data and the theoretical model predictions	68
57	Preliminary results (statistical errors only) on the isospin ratio, i.e. per-nucleon cross section ratio $^{48}\text{Ca}/^{40}\text{Ca}$. Theoretical calculation [11] predicts this ratio to be one in the 2N-SRC region.	72
58	Achieved kinematic coverage during the experimental run period. The vertical axis on the right hand side is the extrapolation to constant Q^2	73
59	Installation of the g_2^p experiment in Hall A. The third arm detector was located on the left-hand side of the bottom target platform.	74
60	Total VDC efficiency for all LHRS runs, after multitrack events have been accounted for. The efficiency is > 99% for most kinematic settings.	75
61	E08-027 Preliminary Results	75
62	E08-027 Preliminary Results	76

1 Introduction

contributed by C. Keppel.

The year 2013 was one of transition to making the 12 GeV upgrade to the Continuous Electron Beam Accelerator Facility a reality, and anticipation of seeing the first beam to an experiment back in Hall A in 2014. The year has been dedicated largely to preparing for two experiments: E12-06-114, a measurement of deeply virtual Compton scattering (DVCS), and E12-07-108, a measurement of the proton magnetic form factor G_M^p . These two experiments will be the first to receive beam in the 12 GeV era. Preparations for E12-07-108 and E12-06-114 have involved significant detector upgrades to both HRSs, a hydrogen target with an improved cell design, and other complimentary equipment. The DVCS collaboration has been hard at work preparing the stand-alone calorimeter necessary to their experiment. Requisite hall beamline modifications for the higher energy beam have included the Moller and Compton polarimeters, higher field mapping of the Hall A arc, a new raster system, and also reviving the Unser and BCMs for precision charge measurement.

The 12 GeV scientific plans for the hall consist of many compelling experiments to utilize the standard Hall A equipment, some with slight modifications, in conjunction with the higher energy beam. Two require a ^3H target, one to measure the F_2^n / F_2^p structure function ratio at large x, and one to continue the successful Hall A studies of short range correlation phenomena. This target and associated systems are in design currently for a run after the E12-07-108 and E12-06-114 experiments. Beyond experiments that will utilize the standard Hall A equipment are ambitious plans involving multiple new experiment installations.

This year brought construction commencement of one of these larger scale installation experiments, the Super Bigbite Spectrometer (SBS) program. The SBS project consists of a set of three form factor experiments centered around somewhat common equipment and new experimental capabilities. First activities to begin this program have included re-design of a magnet from the Brookhaven National Laboratory, delivered this year to JLab, the successful completion of pre-research and development of GEM tracking detectors, and a host of scientific development activities including detector construction projects such as prototyping a standalone hadron calorimeter, data acquisition upgrades, and refined physics projections. Work has continued effectively as well on many other fronts, including infrastructure improvements in data acquisition, offline analysis, and core hall capabilities. Technical preparations are underway for planned experiments such as PREX-II, APEX, A_1^n and others. A new experiment, CREX, was approved to measure the neutron radius of ^{48}Ca .

Moreover, there has been active engagement in analyses of past experiments. Here, twelve new publications related to Hall A experiments were authored by members of the Hall A collaboration, and two new Hall A related doctoral theses were successfully defended. Excitingly, the first APS Topical Group on Hadron Physics Dissertation Award was given in 2013 to Dr. Jin Huang, whose dissertation research was on a Hall A measurement of double spin asymmetries in charged pion production from a transversely polarized ^3He target.

In all, this has been a year of achievements coupled with anticipation and diligent preparations. It is a joy and a privilege to work with the Hall A staff and user community, and I am looking forward to successfully entering into the 12 GeV era together. Please accept my many, many thanks to you all for your expert, industrious, innovative contributions to the hall. I look forward to welcoming the higher energy beam into Hall A with you!

2 General Hall Developments

2.1 Status of the Hall A Møller Polarimeter DAQ

¹O. Glamazdin, ²E. Chudakov, ²J. Gomez, ¹R. Pomatsalyuk, ¹V. Vereshchaka

¹National Science Center Kharkov Institute of Physics and Technology, Kharkov 61108, Ukraine

²Thomas Jefferson National Accelerator Facility, Newport News, VA23606, USA

2.1.1 Møller polarimeter

The Hall A Møller polarimeter is used to measure a beam polarization for Hall A experiments with polarized electron beam. The polarimeter consists of polarized electrons target, a magnetic spectrometer and a detector (see Fig. 1). Møller electrons appear as a result of a polarized electron beam scattering on a polarized electron target. Scattered Møller electrons are analyzed by the magnetic spectrometer. The spectrometer consists of four quadrupole (Q1, Q2, Q3, Q4) and one dipole magnets. Scattered electrons are focused by the quadrupole magnets in the horizontal plane at the entrance gap of the dipole magnet. The dipole magnet deflects Møller electrons down to detector.

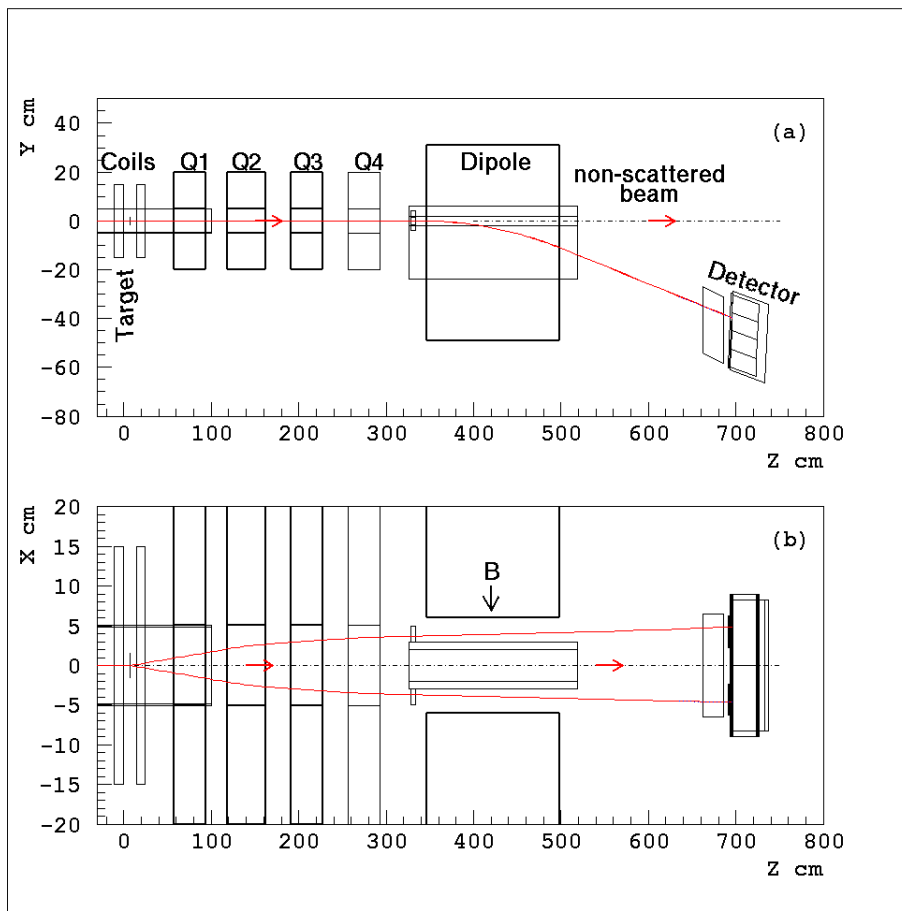


Figure 1: Layout of the Hall A Møller polarimeter. a) side view, b) top view.

The electron detector consists of two total absorption calorimeters, which allow to detect Møller events in coincidences. Each calorimeter has four channels. There is a four channels aperture detector made of plastic scintillator attached to the face panel of each calorimeter. The typical rate of the detector during measurements is 100 - 200 kHz in one arm and 50 kHz in coincidences. The event rate in the coincidence

mode for different signs of the electron beam polarization and known values of the target polarization and the detector analyzing power allow to calculate the measured polarization of the electron beam.

The Hall A Møller polarimeter has been upgraded in accordance with the CEBAF upgrade plan to the beam energy range $1 \div 11$ GeV. Description and status of the Møller polarimeter after the upgrade can be found in [1].

The Hall A Møller polarimeter has two data acquisition and processing systems:

- Old system is based on CAMAC, VME, NIM modules;
- New system is based on VME module flash-ADC F-250 designed in Jefferson Lab.

Both DAQs are used simultaneously to measure the electron beam polarization. The old DAQ, in operation since 1998, is fully functional but may not be repairable in case of malfunction, as the system modules are not in stock and are not manufactured anymore. The new DAQ based on flash-ADC, which is in operation since 2010, is more precise and provides more detailed data analysis. However, it currently requires more careful adjustment and further improvement.

2.1.2 The old DAQ

The old system is fully functional for both ("high magnetic field" and "low magnetic field") polarimeter targets. It is time-tested and well-studied. However, it has a low event recording speed, the system modules occupy several crates, and there is a large number of inter-unit connections and cables which reduces the system reliability. Moreover, some system modules went out of production and are not replaceable in case of malfunction. The old DAQ layout is shown in Fig. 2. The CODA system remotely controls the data acquisition system and data recording from the Møller polarimeter [2].

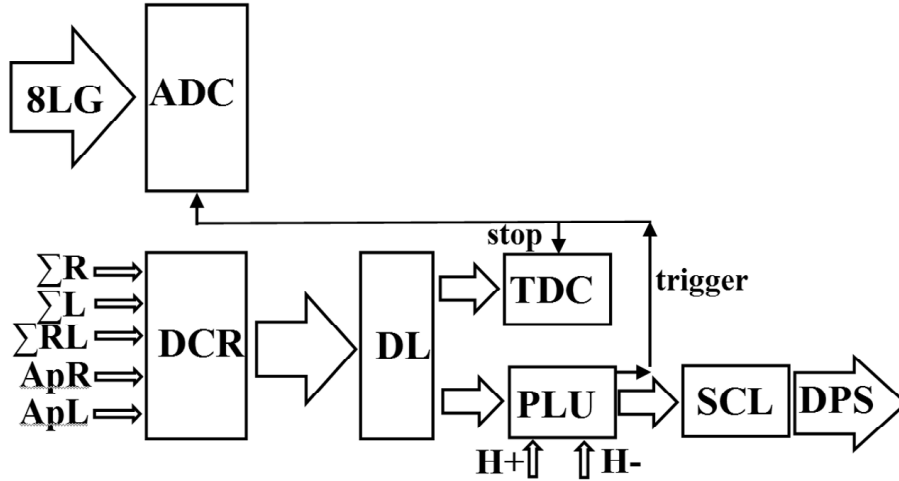


Figure 2: Scheme of the old Møller DAQ. 8LG - signals of 8 blocks (calorimeter), ADC - analog to digital converter, ΣL - sum of 4 left blocks (left calorimeter), ΣR - sum of 4 right blocks, ΣRL - sum of 8 calorimeter blocks, ApL - signal from left aperture counter, ApR - signal from right aperture counter, DCR - discriminator, DL - delay lines, TDC time to digital converter, PLU - programmable logic unit, H+, H- -signals of "+" and "-" helicity, SCL - scalars, DPS - data processing system.

A few electronic modules of the old DAQ were replaced with more modern ones with higher bandwidth. The main goals of the upgrade are:

- To replace programmable logic module (PLM) which is no longer available;
- To increase bandwidth (up to 200 MHz);

- To decrease readout time from ADC and TDC modules;
- To decrease the number of crates required for the DAQ and to eliminate CAMAC as an outdated and slow standard.

The list of replaced modules is:

- To increase bandwidth:
 1. PLM LeCroy-2365 (frequency < 75 MHz, crate CAMAC) was replaced with PLU based on CAEN V1495 (frequency 200 MHz, crate VME) (see Fig.3);
 2. Discriminator Ortec-TD8000 (frequency < 150 MHz, crate CAMAC) was replaced with discriminator P/S 708 (frequency < 300 MHz, crate NIM).
- To reduce readout time:
 1. ADC LeCroy 2249A (12 channels, crate CAMAC) was replaced with ADC CAEN V792 (32 channels, crate VME);
 2. TDC LeCroy 2229 (crate CAMAC) was replaced with TDC CAEN V1190B (64 channels, 0.1 ns, crate VME).

All new modules have been tested, and new software and the analyzer for the upgraded DAQ are under development.

It is planned to use the old DAQ after reconstruction at least until the system based on flash-ADC is fully functional for operation with two targets of the Møller polarimeter. It should be stressed that the new DAQ (based on FADC) was created for operation with the new target ("high magnetic field") and its software is not intended for operation with the old target ("low magnetic field"). As a result, if the Møller polarimeter is operating with the old target, the old DAQ system is mandatory whereas the new one is optional. Moreover, simultaneous use of the two systems allows to study the polarimeter systematic errors.

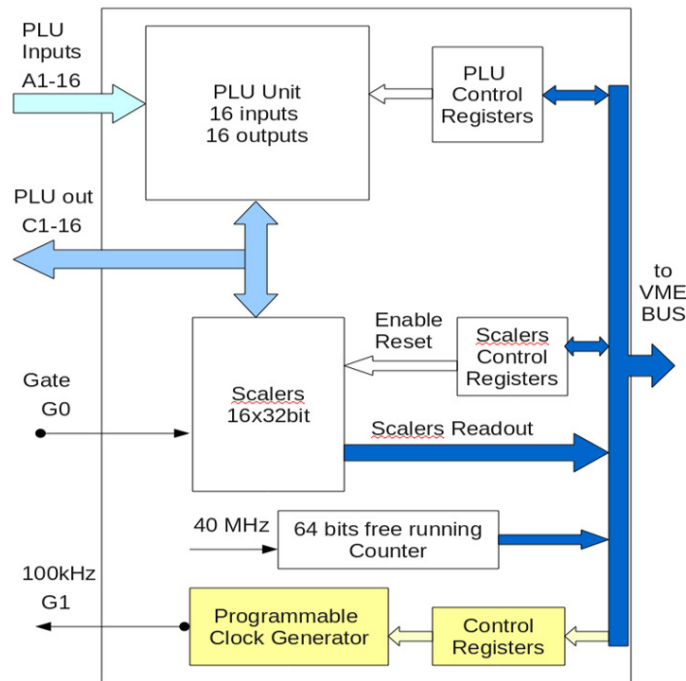


Figure 3: Diagram of programmable logic unit based on module CAEN V1495.

2.1.3 The new DAQ based on FADC

One of the main goals for implementing the new DAQ is to reduce systematic error of the polarization measurement with the Hall A Møller polarimeter. One of the Møller polarimeter systematic error components is a dead time of event record system. One of the ways to reduce the dead time is to increase DAQ event rate registration and record speed. The programmable module flash-ADC F250, designed in Jefferson Lab, with algorithm for processing and recording events from the polarimeter [5] was chosen for the new fast DAQ. A block diagram of the data acquisition system on the basis of flash-ADC is shown in Fig. 4.

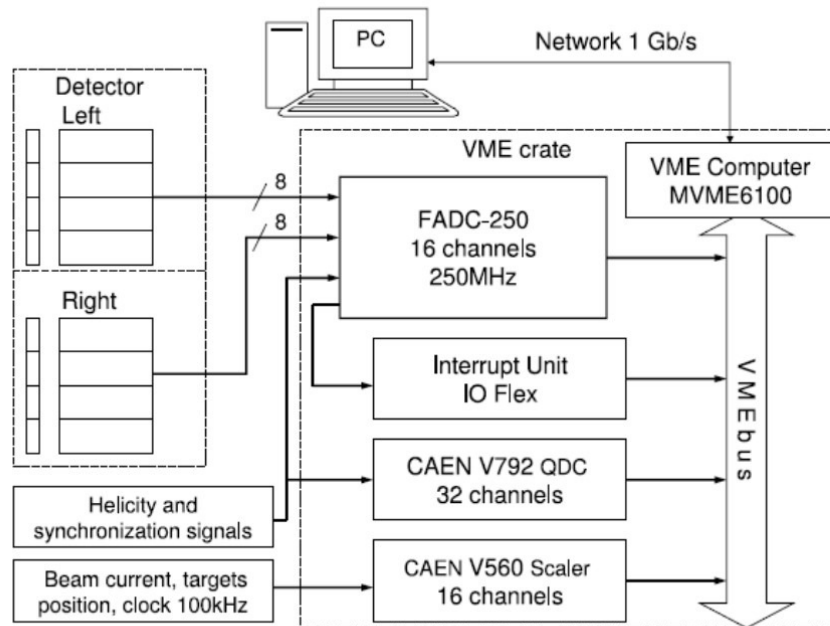


Figure 4: New Møller polarimeter DAQ based on FADC.

The new data acquisition system consists of:

- Flash-ADC F250;
- Interrupt unit IO Flex;
- Additional QDC module CAEN V792;
- Scalers module CAEN V560;
- VME controller MVME6100;
- NIM crate and modules for ECL/NIM levels conversion (not shown in the figure);
- Gigabit Ethernet network;
- Controlling PC.

Electronic modules are mounted in the VME crate located in the Hall A behind a shielding wall. QDC module ADC V792 is used with the flash-ADC for supplementary record of polarization sign signals and synchronization signals. Scalers module V560 is used for recording of the beam current, target position relating to the beam and the signals of the 100 kHz reference generator.

The module flash-ADC is an integration of 16-channel 12-bit ADC of conveyor type with the conversion frequency 250 MHz and the programmable logic array FPGA in one VME unit. Analog signals with amplitude up to +1 Volt and duration $30 \div 35$ ns from the detector PMTs are sent to the module input and are digitized in the ADC. The programmable logic module allows to construct the whole logic circuit for event recording and to process digitized signals from the ADC directly in the module. Functions of the discriminators, delay lines, coincidence circuits, scalers and event recording logic are programmed in the FPGA (see Fig. 5).

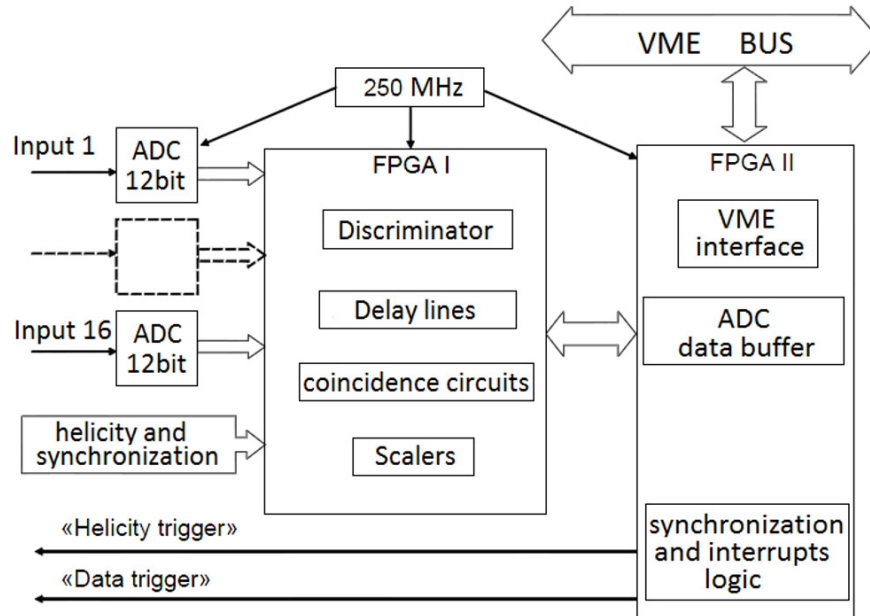


Figure 5: Flash ADC module.

After digitizing in the ADC, signals from the detector are summed for each calorimeter arm. The summed signal is selected in the discriminator. If the level of the summed signal exceeds the preset discriminating threshold, the event (digitized signals of all channels) is recorded to inner data buffer of the module and the logic signals are formed at the inputs of the coincidence circuits. Parameters of ADC operation are programmed and uploaded to the module at the CODA start.

The data acquisition system based on flash-ADC generates 2 types of triggers (events):

- *Helicity trigger* -when values of scalers are read;
- *Data trigger* - when inner buffer is filled with data from the ADC.

Upon interrupt signals, the data of inner scalers and ADC buffer are read into the common data flow of the CODA system and are transmitted via network to the controlling computer. On the PC, the data are written into files for further analysis and processing. This system allows to detect and to record data flow at the speed up to 50 MB/s in the coincidence mode which corresponds to the event rate in the arms ~ 160 kHz.

The software package includes the program for data acquisition and on-line monitoring, and programs for off-line data processing. Monitoring program allows to control the quality of incoming information by displaying current values of coincidence scalers, digitized analog signals from each detector unit and amplitude spectra of signals from the detector. Fig. 6 shows an example of displayed information by the on-line monitoring program. The programs for off-line data processing allows to convert data files from CODA into ROOT [3], to process and analyze data, and to obtain the results of the beam polarization measurement.

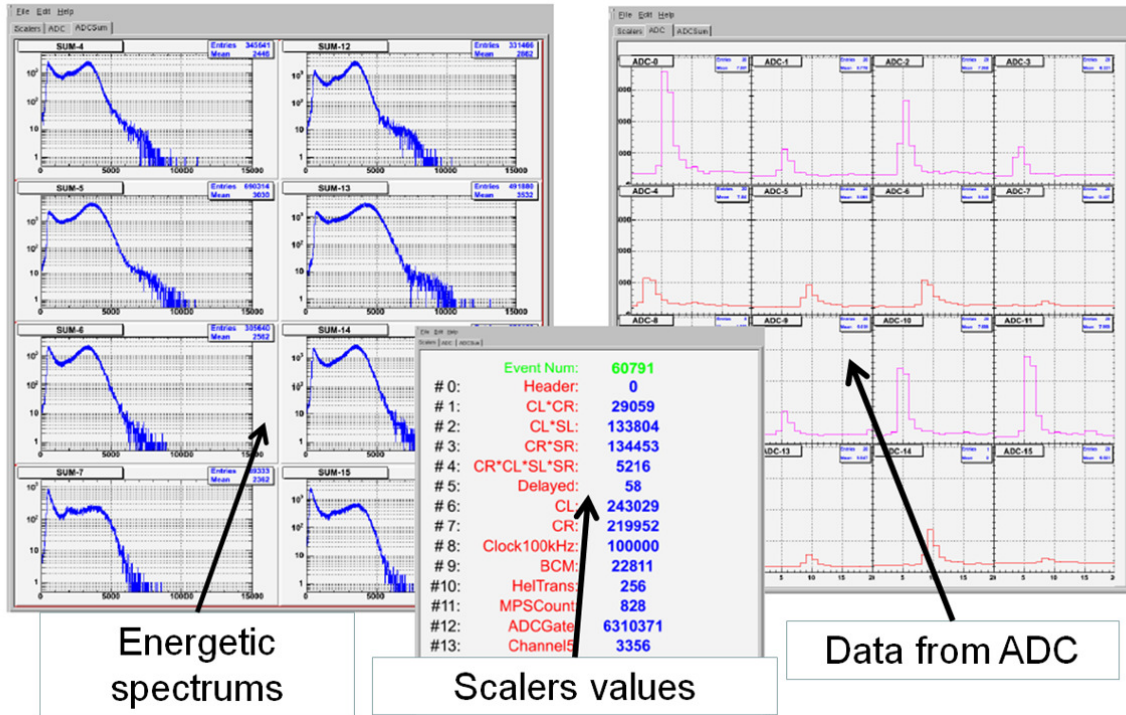


Figure 6: Data from on-line monitoring program.

Ability of the flash ADC to record every single event from the detector (data trigger) allows to study systematic errors. Analysis of this information should help to improve the polarimeter GEANT model, to increase the accuracy of measuring average analyzing power, and to take into account such effects as “pile-up events” (see Fig. 7), Levchuk effect, etc. During operation of the flash-ADC data trigger some problems were found. Due to these problems this new instrument cannot be used in full. The bugs and errors have to be eliminated, and development of the software for the data analysis has to be completed.

2.1.4 Comparison of two DAQs results

Fig. 8 shows the results of comparison of the asymmetry values measured by both data acquisition systems.

Blue dots show the measurement result with the new DAQ system based on flash-ADC, and red dots show the measurement result with using the old DAQ system. The discrepancy between two DAQs results is not beyond the statistical error.

2.1.5 Conclusion

The Hall A Møller polarimeter has two data acquisition and processing systems operating simultaneously. The systems are based on different element bases with different types of triggers (events).

The old DAQ is fully functional. After the upgrade a few modules will be replaced.

The new system based on high-speed multichannel flash-ADC has been developed and tested. This system allows to record events with the rate up to 160 kHz in coincidence mode, and allows data acquisition rate up to 50 MB/s without significant increase of the system dead time. It allows to increase the accuracy of measurement of the electron beam polarization with the Hall A Møller polarimeter [4]. The new system is more accurate but currently requires more accurate adjustment and further improvement.

References

- [1] S. Riordan *et al.* Hall A Annual Report 2012. arXiv:1302.4324 [physics.ins-det] 18 Feb 2013. pp. 14-26.

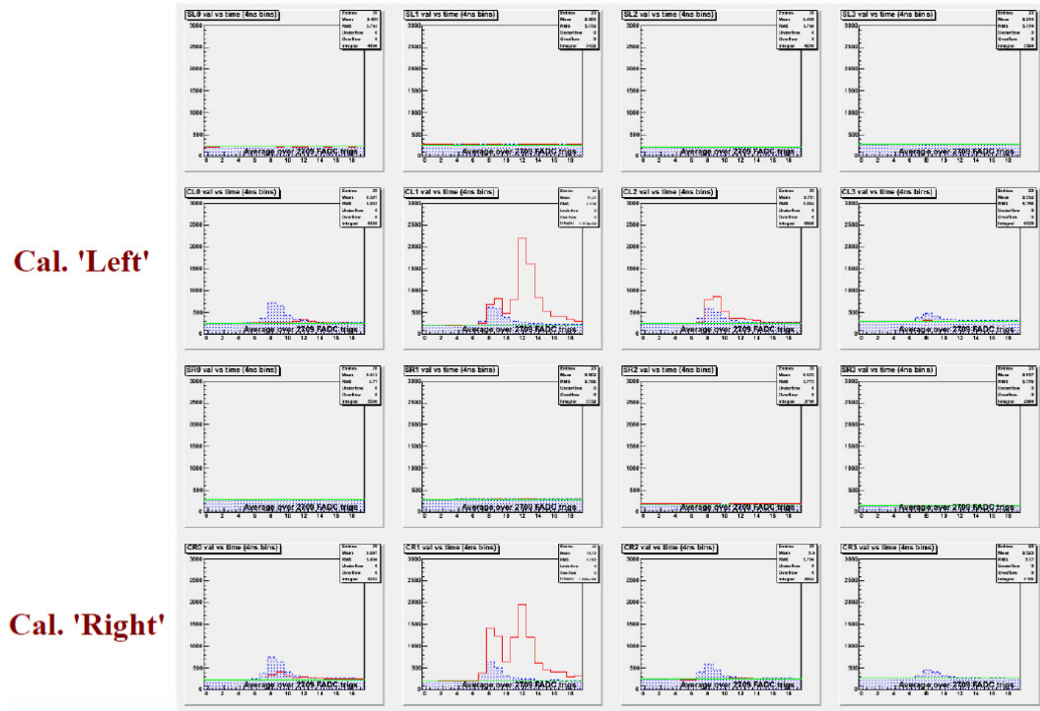


Figure 7: An example of data trigger (pile-up events).

- [2] JLAB CODA Group. Coda. <http://coda.jlab.org>.
- [3] R. Brun, F. Rademakers, P. Canal, *et al.* ROOT An Object-Oriented Data Analysis Framework. Users Guide 4.04. Geneva, 2005, p. 293.
- [4] B. Sawatzky, Z. Ahmed, C-M Jen, E. Chudakov, R. Michaels, D. Abbott, H. Dong, E. Jastrzemski. Møller FADC DAQ Upgrade. Hall A Annual report 2009. pp.25-30.
- [5] B. Sawatzky, Z. Ahmed, C-M Jen, E. Chudakov, R. Michaels, D. Abbott, H. Dong, E. Jastrzemski. Møller FADC DAQ upgrade. Internal Review. Jefferson Lab, December, 2010, p. 7.

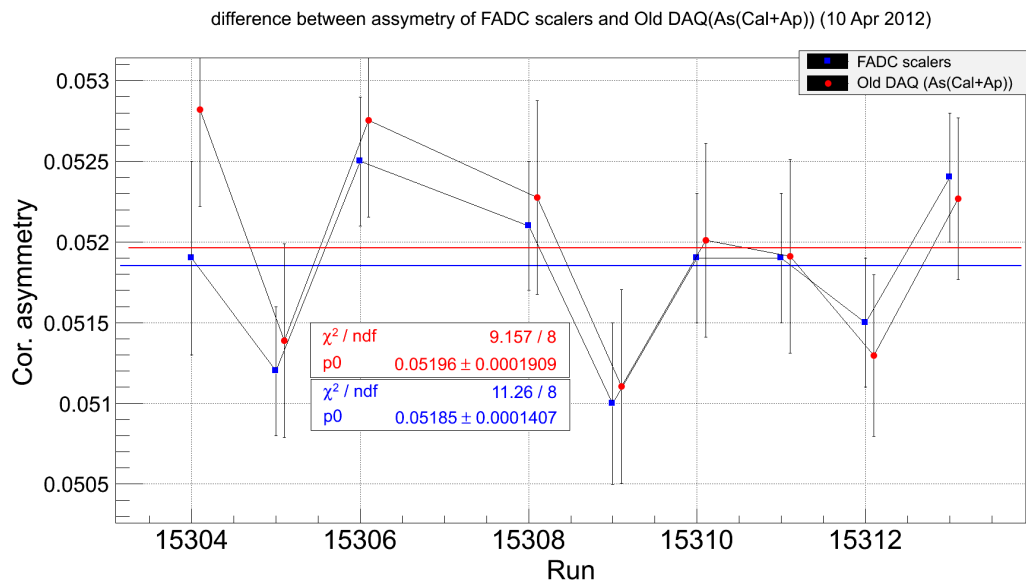


Figure 8: Result of asymmetry measurement with two Møller polarimeter DAQs.

2.2 Compton DAQ

Upgrade of Compton Polarimeter DAQ: Progress and Plans

R. Michaels, A. Camsonne, S. Nanda
contributed by R. Michaels

In this contribution, I describe the progress and plans to upgrade the Compton Polarimeter DAQ. The project can also be viewed as a test for the new pipelining electronics needed for some future projects like SOLID. The Hall A Compton Polarimeter consists of an integrating-mode DAQ and a counting-mode DAQ for the detectors, plus a slow DAQ for auxiliary signals such as laser state and beam current. The two modes have different advantages and different systematics. The integrating mode was developed largely by the Carnegie Mellon group prior to the three parity experiments that ran in 2009-2010, and we don't foresee modifying this for now. The counting-mode DAQ had been developed in 1998 by Saclay, and has served us well, but it needs to be upgraded.

The plan for the upgrade and some details about the progress are kept at this URL:

<http://hallaweb.jlab.org/equipment/daq/compton>

The photon detector will be read out by the the JLab FADC. The electron detector will require a new board, which is being developed by the JLab DAQ Group and the JLab Fast Electronics Group. This new board is called the "VETROC" and it will replace the existing "ETROC". (ETROC means electron trigger readout card, and the new "V" implies VXS-based). The FADC and VETROC are part of a "fast" DAQ which handles triggers, as shown in fig 9. The triggers will be either singles triggers from the two detectors or coincidence triggers. These electronics boards are based on the 12 GeV VME modules being used in hall D, for example.

The two main areas of progress in 2013 were : 1) a test stand was setup to test the FADC and several useful things were learned about the performance, the deadtime correction, and systematic errors in the extraction of asymmetries; and 2) a detailed specification of the VETROC was written and the JLab DAQ Group and JLab Fast Electronics Group have agreed to build a prototype; indeed, the board may have broad application at the lab as a flexible trigger module.

The FADC test stand consists of a set of NIM electronics, a random high-rate pulser, and the VME crate with the FADC and associated DAQ boards to test the ability to measure photon signals at up to 500 kHz with a known and variable helicity-correlated asymmetry of 1 to 10% (note, the Compton asymmetry is 3%), where the helicity is provided by the JLab Helicity Generator Board. The tests up to now can be summarized as follows. The fastest method for event-mode readout is to run the FADC in "pulse-integral" mode, whereby a pulse produces a trigger if it is above a threshold, and the FADC board provides both the time of the trigger and the integrated signal, which is integrated over a time window that extends by a programmable amount before the trigger time to an amount after; a window of about 80 nsec was usually used. The data are readout in a multiblock mode. Since the FADC is pipelined, there is zero deadtime for rates below a critical frequency f_c . The value of f_c depends on the setup parameters – mainly the number of enabled channels and the integration window – and was 300 kHz for our setup. Below f_c the asymmetries extracted from the data agreed with expectation to better than 100 ppm. Above f_c there is a significant deadtime which, so far, we cannot correct; however, we've learned that this deadtime affects the data in contiguous time bins or "chunks" of time; the majority of helicity windows remain deadtime-free if $f \leq 500$ kHz. Above 500 kHz the data become less useful as one approaches 100% deadtime. The "chunks" of data affected by deadtime can be flagged and eliminated, leaving a clean sample of data whose asymmetry agrees with expectation.

The near-term goal is to commission this counting-mode photon DAQ with the beam, and run it in conjunction with the existing integrating-mode DAQ. Meanwhile, the VETROC prototype will be available in about one year and we will test it in the aforementioned DAQ test stand.

Compton DAQ Upgrade Plan

Jan 2014

R. Michaels

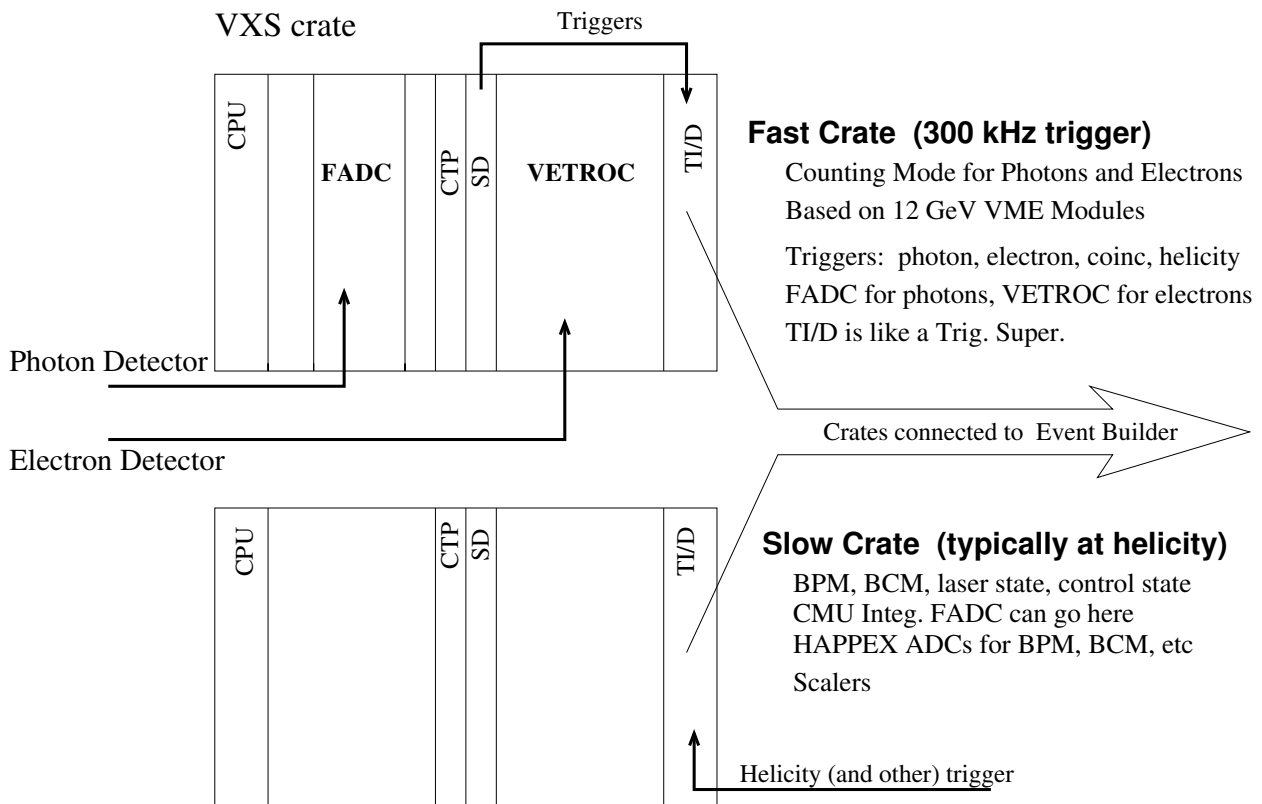


Figure 9: Proposed upgrade of the Compton DAQ

3 Summaries of Experimental Activities

3.1 E01-020: (e, e'p) Studies of the Deuteron at High Q^2

Hari P Khanal and W. Boeglin

Spokespersons: W. Boeglin, E.Voutier, M.Jones, A.Klein, P.E.Ulmar,
The Hall A Collaboration.

3.1.1 Introduction

The deuteron is the simplest nuclear system consisting of a single proton and a single neutron. Exclusive electron scattering from the deuteron is an efficient way of probing the dynamics of two nucleons at very short space-time distance. The simplest model of deuteron electro-disintegration is the Plane Wave Impulse Approximation (PWIA) in which the proton ejected by the virtual photon does not further interact with the recoiling neutron and is described by a plane wave. In this approximation, the missing momentum $\vec{p}_m = \vec{q} - \vec{p}_f$, where \vec{p}_f is the momentum of the outgoing proton and \vec{q} is the 3-momentum transfer, represents the momentum of the recoiling nucleon and is opposite to the initial momentum \vec{p}_i of the struck nucleon $\vec{p}_i = -\vec{p}_m$. However the out-going proton can interact strongly with the recoiling neutron thereby destroying the simple relationship between \vec{p}_m and \vec{p}_i (final state interaction, FSI).

The main focus of the analysis consists of the determination of the $d(e, e'p)n$ cross section as a function of (I) missing momenta for fixed angles between the momentum transfer and the momentum of the recoiling nucleon (θ_{nq}) and (II) as a function of θ_{nq} for fixed values of p_m . State of the art calculations [2, 3, 4, 5, 6, 7, 8, 9, 10, 11, 12, 13] and recent results have indicated that at high energies (≈ 1 GeV) in the final n-p system the strength of FSI depend strongly on the recoiling neutron angle.

The $d(e, e'p)n$ differential cross section in one photon exchange is written in the following way

$$\frac{d^5\sigma}{d\omega d\Omega_e d\Omega_p} = K f \sigma_{Mott} (\nu_L R_L + \nu_T R_T + \nu_{TT} R_{TT} \cos(2\phi) + \nu_{LT} R_{LT} \cos(\phi)). \quad (1)$$

Where R_i and R_{ij} are the nuclear response functions, ν_i and ν_{ij} are the coefficients which depend only on the electron kinematics and σ_{Mott} is the Mott cross section. In PWIA, the differential cross section can be factorized to

$$\frac{d^5\sigma}{d\omega d\Omega_e d\Omega_p} = K \sigma_{ep} \rho(p_m). \quad (2)$$

Where K is a kinematic factor, σ_{ep} is the off-shell electron-proton cross section and $\rho(p_m)$ is the momentum distribution, which describes the probability of finding the nucleon with initial momentum $-\vec{p}_m$ in the ground state of the deuteron.

3.1.2 Experimental Overview

Data have been taken during experiment E01020 in Hall-A at Jefferson Lab at energies of 2.83 , 4.7 and 5.0 GeV for Q^2 values of 0.8, 2.1 and 3.5 (GeV/c)², respectively. The Hall A cryogenic target system provided a 15 cm long liquid deuterium target at beam currents ranging from 1 to 100 μA . The scattered electrons and out-going protons were detected by the two 4 GeV/c High Resolution Spectrometers(HRS). In each HRS, the timing information was provided by two scintillator planes. A pair of Vertical Drift Chambers (VDC) provided the tracking information in each spectrometer and electrons were identified using the gas Cherenkov detector. $d(e, e'p)n$ events have been selected by a time of flight cut between the spectrometers, a cut on missing energy and a cut on the reconstructed vertex location from each spectrometer.

3.1.3 Analysis Status

First results at $Q^2 = 3.5$ (GeV/c)² have already been published in [1] while the analysis of the $Q^2 = 0.8$ and 2.1 (GeV/c)² data is nearing completion. For the lower Q^2 data detector calibrations, beam position determinations, detector efficiency determinations, radiative correction and phase space calculations have been completed. Differential cross sections for the angular distribution and for the momentum distribution at both $Q^2 = 0.8$ and 2.1 (GeV/c)² have been determined. We are currently working on the estimation of the systematics uncertainties and an extraction of A_{LT} .

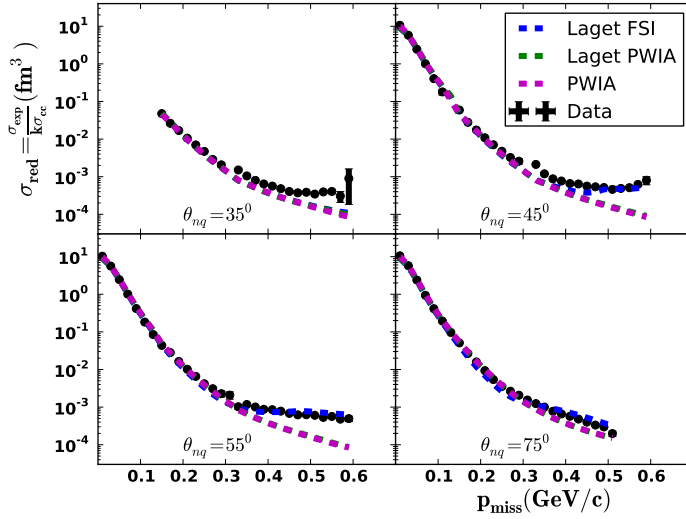


Figure 10: The momentum distribution at low $Q^2 = 0.8 \text{ (GeV/c)}^2$ for different recoil angles θ_{nq}

Momentum Distribution If there were no FSI the momentum distribution could be extracted from the measured cross section by simply dividing them by $K\sigma_{ep}$. In reality FSI are always present to a certain degree and this ratio is referred to as the reduced cross section. Figs. 10 and 11 show the reduced cross section as a function of the missing momentum for a set of four, fixed recoil angles and for $Q^2 = 0.8$ and $Q^2 = 2.1 \text{ (GeV/c)}^2$. The θ_{nq} bin width of each setting of recoil angle is $\pm 5^\circ$ and the missing momentum bin width is $\pm 10 \text{ MeV/c}$. The experimental reduced cross section has been compared to a calculated one with and without FSI. At low Q^2 FSI start to contribute significantly for missing momenta above 0.2 - 0.3 GeV/c for all angles. In contrast at higher Q^2 as shown in Fig. 11, FSI dominates the cross section only around $\theta_{nq} = 75^\circ$. Fig. 12 shows a comparison of the experimental reduced cross sections (momentum distributions) at $Q^2 = 0.8, 2.1$ and 3.5 (GeV/c)^2 . All distributions agree with each other in the low missing momentum region.

Angular Distribution In order to study the angular dependence of FSI contributions we determined the ratio $R = \sigma_{exp}/\sigma_{pwia}$ of the experimental cross section (σ_{exp}) to the PWIA cross section (σ_{pwia}). If there were no FSI and the momentum distribution used correctly described the deuteron structure then $R = 1$ independent of θ_{nq} would be found. The experimental values of R are shown for missing momenta $p_m = 0.2, 0.4$ and 0.5 GeV/c and at $Q^2 = 0.8$ and 2.1 (GeV)^2 in Figs. 13 and 14.

At low Q^2 , the distributions are quite broad with large FSI contributions even at small angles $\theta_{nq} < 40^\circ$ and missing momenta of $p_m = 0.4$ and 0.5 GeV/c . Only small fluctuations around 1 are found for $p_m = 0.2 \text{ GeV/c}$.

In contrast at $Q^2 = 2.1 \text{ (GeV)}^2$ R has a well defined peak at around 75° as shown in Fig. 14. At missing momentum $p_m = 0.2 \text{ GeV/c}$ R is reduced by about 30% at θ_{nq} around 75° . For $p_m = 0.4 \text{ GeV/c}$ and $p_m = 0.5 \text{ GeV/c}$ R increases at around 75° by factor 2.5 and 3.0 respectively. The angular dependence of R clearly indicates that FSI between the two final state nucleons at high missing momenta is highly anisotropic. For both data sets the experimental results have been compared with the results from Monte Carlo simulations using Laget's Model including FSI. The solid lines represent the distributions calculated from the theoretical model. At $Q^2 = 0.8 \text{ (GeV/c)}^2$ the calculated angular distributions agree well with the experimental results for $p_m = 0.2 \text{ GeV/c}$ and $\theta_{nq} < 40^\circ$ only. For all other kinematic settings at this momentum transfer they do not very well reproduce the experimental results for R . At $Q^2 = 2.1 \text{ (GeV/c)}^2$ and at $p_m = 0.2 \text{ GeV/c}$ the experimental results agree quite well with the theoretical calculations while larger discrepancies exist at higher missing momenta.

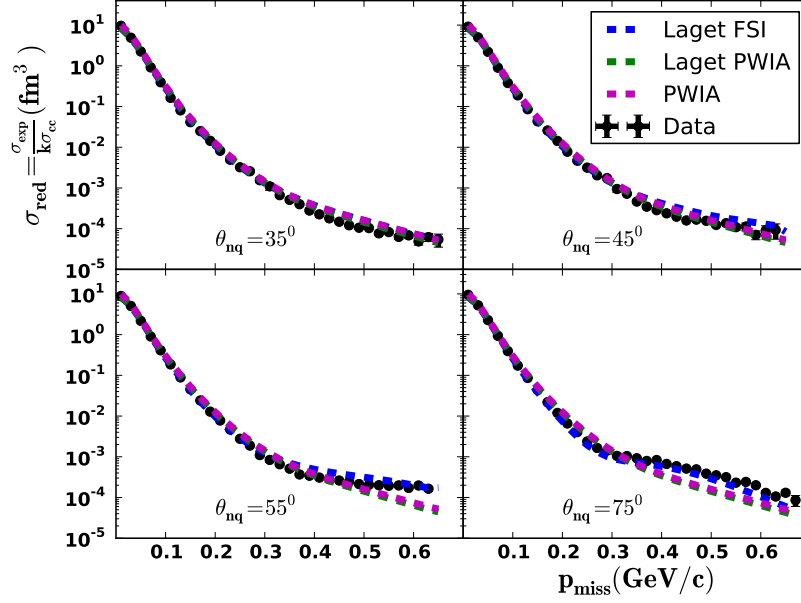


Figure 11: The momentum distribution at high $Q^2 = 2.1 \text{ (GeV/c)}^2$ for different recoil angles θ_{nq}

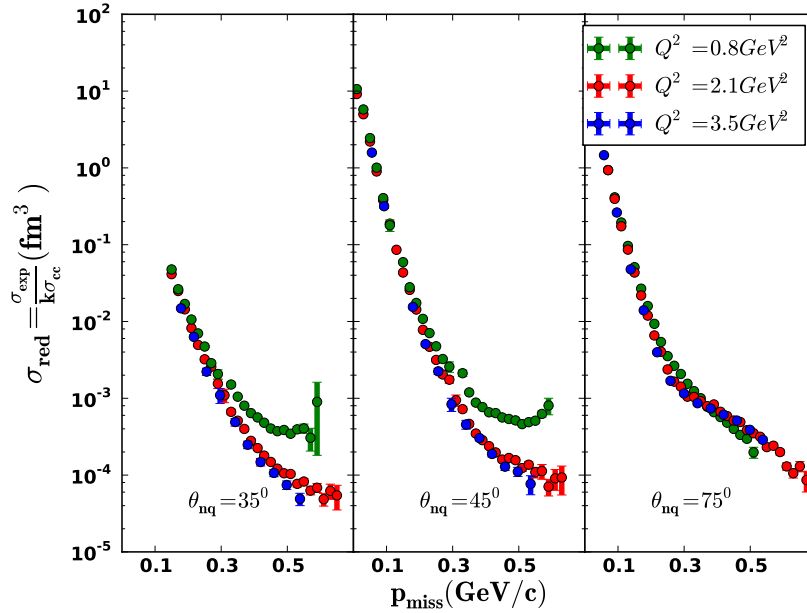


Figure 12: Comparison of the experimental momentum distributions for $Q^2 = 0.8$ (green), 2.1 (red), and 3.5 $(\text{GeV/c})^2$ [1] (blue) for different values of θ_{nq}

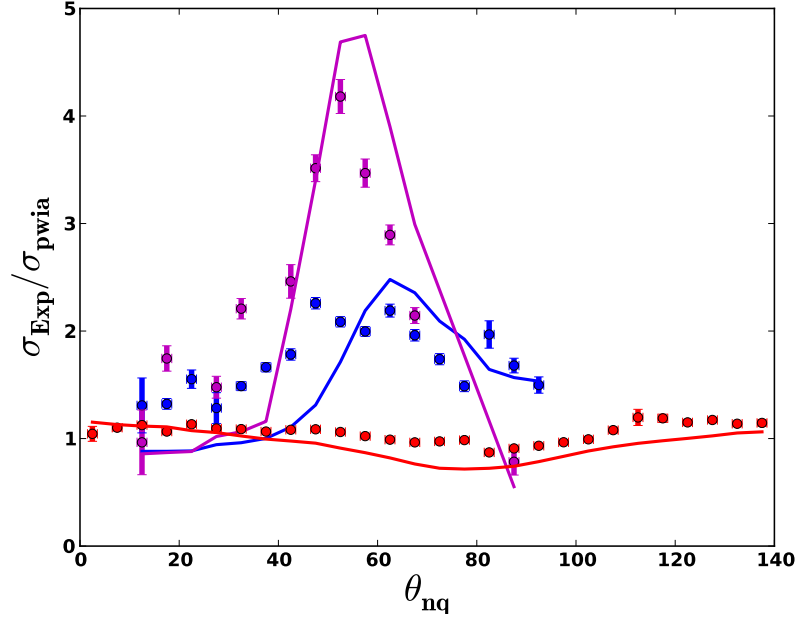


Figure 13: R as a function of θ_{nq} for $Q^2 = 0.8(\text{GeV}/c)^2$. Red: $p_m = 0.2\text{GeV}/c$, blue: $p_m = 0.4 \text{ GeV}/c$ and magenta: $p_m = 0.5\text{GeV}/c$. The corresponding solid lines represent calculations using Laget's model including FSI

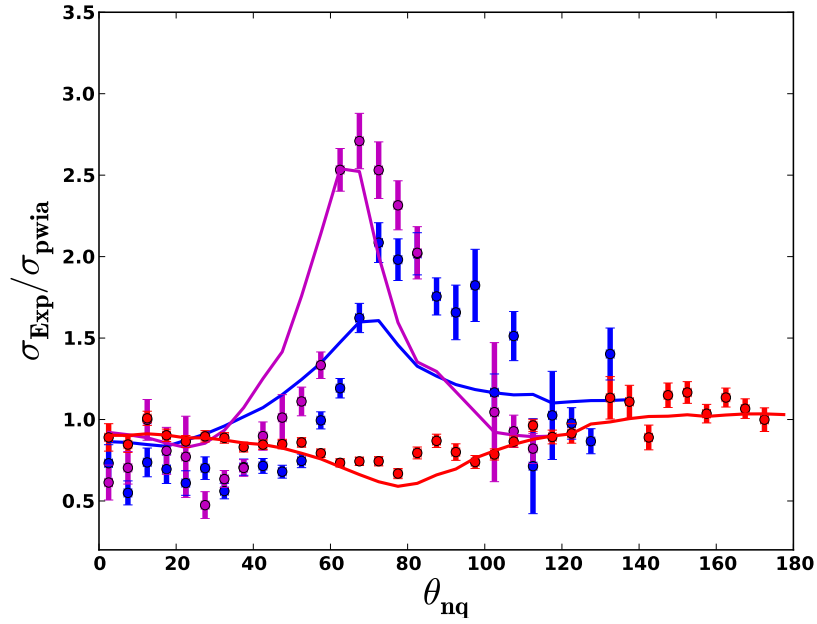


Figure 14: Like Fig. 13 for $Q^2 = 2.1 (\text{GeV}/c)^2$

References

- [1] W. U. Boeglin et al. Probing the high momentum component of the deuteron at high q^2 . *Physics Review Letters*, 107, 2011.
- [2] A. Bianconi, S. Jeschonnek, N. N. Nikolaev, and B. G. Zakharov. *Phys. Lett. B*, 343:13, 1995.
- [3] L.L. Frankfurt, W.G. Greenberg, J.A. Miller, M.M. Sargsian, and M.I. Strikman. *Z. Phys. A*, 352:97, 1995.
- [4] L.L. Frankfurt, M.M. Sargsian, and M.I. Strikman. *Phys. Rev. C*, 56:1124, 1997.
- [5] S. Jeschonnek. *Phys. Rev. C*, 63:034609, 2001.
- [6] C. Ciofi degli Atti and L. P. Kaptari. *Phys. Rev. Lett.*, 100:122301, 2008.
- [7] M. M. Sargsian. *Int. J. Mod. Phys. E*, 10:405, 2001.
- [8] S. Jeschonnek and J. W. Van Orden. *Phys. Rev. C*, 78:014007, 2008.
- [9] S. Jeschonnek and J. W. Van Orden. *Phys. Rev. C*, 80:054001, 2009.
- [10] C. Ciofi degli Atti and L. P. Kaptari. *Phys. Rev. C*, 71:024005, 2005.
- [11] J.M. Laget. *Phys. Lett. B*, 609:49, 2005.
- [12] S. Jeschonnek and J. W. Van Orden. *Phys. Rev. C*, 81:014008, 2010.
- [13] M. M. Sargsian. *Phys. Rev. C*, 82:014612, 2010.

3.2 E04-007: Precision Measurements of Electroproduction of π^0 near Threshold

contributed by Richard Lindgren and Cole Smith
for

J.R.M. Annand, D.W. Higinbotham, R. Lindgren, B. Moffit, B. Norum, V. Nelyubin, spokespersons,
M. Shabestari and K. Chirapatimol, students

and

The Hall-A Collaboration

3.2.1 Introduction

The experiment is designed to measure the electroproduction reaction $p(e, e'p)\pi^0$ of neutral pions off the proton at the lowest possible invariant mass W . Results from previous electroproduction measurements at Mainz with four-momentum transfers of $Q^2 = 0.10 \text{ GeV}/c^2$ [1] and $Q^2 = 0.05 \text{ GeV}/c^2$ [2] were in disagreement with the Q^2 dependence predicted by Heavy Baryon Chiral perturbation theory (HBChPT) and also inconsistent with the predictions of the MAID model [3]. If the Mainz discrepancies remain unresolved, they will constitute a serious threat to the viability of Chiral Dynamics as a useful theory of low energy pion production. Our experiment has measured absolute cross sections as precisely as possible from threshold to $\Delta W = 30 \text{ MeV}$ above threshold at four-momentum transfers in the range from $Q^2 = 0.050 \text{ GeV}/c^2$ to $Q^2 = 0.150 \text{ GeV}/c^2$ in small steps of $\Delta Q^2 = 0.01 \text{ GeV}/c^2$. This will cover and extend the Mainz kinematic range allowing a more sensitive test of chiral corrections to Low Energy Theorems for the S and P wave pion multipoles. In addition, the beam asymmetry was measured, which can be used to test predictions for the imaginary components of the of S wave E_{0+} and L_{0+} pion multipoles, which are sensitive to unitary corrections above the $n\pi^+$ threshold. Mainz recently repeated the electroproduction measurements and now report [4] that the new results are more consistent with HBChPT predictions, but are in disagreement with their own previous measurements [2]. In view of the importance of knowing whether or not HBChPT is valid in this domain, it is imperative that an independent set of measurements be reported.

3.2.2 Analysis Status

The default LHRS optics data base used in our analysis up to now requires higher order polynomials to eliminate kinematic distortions near the edges of the acceptance. Our attempt to reduce these distortions by fitting an LH2 sieve run introduced some unphysical oscillations in the dependence on $L.tgph$. To eliminate this unphysical behavior the LHRS optics has been further refined by eliminating some of the higher order terms which was causing the over-fitting of the matrix coefficients. Although now the fits overall are more reasonable without the fine oscillations, the refit has introduced a small shift in the LHRS horizontal angle. We find also that the hydrogen elastic and carbon elastic cross sections are uniformly lower by 5% and 10%, respectively, from expected according to previous measurements. Although the discrepancy in the elastic yields could derive from this angle shift, it is also possible we are underestimating other corrections. We have also studied single track efficiency corrections, which are fairly large for the high rate LH2 data and less so for the C runs. We discovered and corrected some previous errors in our application of the Mo-Tsai radiative and straggling correction. Also to improve our understanding of the LHRS acceptance and to study the effect of multiple scattering on vertex reconstruction in the LH2 target we added the J.J. LeRose forward transport functions to our GEANT simulation of the LH2 target, target chamber exit window, LHRS entrance window and BigBite. (LHRS was not otherwise simulated except through r.m.s. smearing of the e- momentum vector according to results of previous empirical studies.) This simulation is now under study and hopefully we will reduce the hydrogen and carbon elastic yield discrepancy closer to the 5% level. Our main effort is to reduce the systematic error on the π^0 production cross section, W and Q^2 . Further checks are also in progress on the BigBite optics to reduce remaining reconstruction errors and improve missing mass systematics. To help speed up systematic studies a reduced data set saving only essential variables needed for the remaining analysis has been created and stored on the Galileo computer farm at UVA.

References

- [1] M.O. Distler et al., Phys. Rev. Lett. **80**, 2294 (1988).
- [2] H. Merkel et al., Phys. Rev. Lett. **88**, 12301 (2002).
- [3] D. Drechsel, S.S. Kamalov and L. Tiator, Eur. Phys. J. **A34**, 69 (2007).
- [4] H. Merkel et al., "Proceedings of the 6th International Workshop on Chiral Dynamics July 6-10 2009, Bern, Switzerland". **C44**, 1096 (1991).

3.3 E05-102: Measurement of A'_x and A'_z asymmetries in the quasi-elastic ${}^3\text{He}(\vec{e}, e'd)$ reaction

S. Gilad, D. W. Higinbotham, W. Korsch, S. Širca, B. E. Norum (spokespersons)
and

the Hall A Collaboration.

Contributed by M. Mihovilović and S. Širca

The E05-102 experiment [1] is devoted to a detailed study of the

$${}^3\text{He}(\vec{e}, e'd), \quad {}^3\text{He}(\vec{e}, e'p)d, \quad {}^3\text{He}(\vec{e}, e'p)pn$$

processes at low Q^2 . Its main purpose is to approach the ground-state structure of the ${}^3\text{He}$ nucleus by studying the missing-momentum (p_{miss}) dependence of the double-polarization (beam-target) transverse and longitudinal asymmetries. The experiment has been performed in Summer 2009. The data analysis of the ${}^3\text{He}(\vec{e}, e'd)$ channel is now complete. We have insufficient resolution to distinguish the two- and three-body channels in the proton knockout processes, but the analysis of the proton channel as a sum of these contributions is also complete.

Since the large-acceptance spectrometer BigBite [2] was used in the experiment, the most problematic part of the data analysis has been the averaging of the theoretical asymmetries over the experimental acceptance. Here we focus on the averaging procedure for the deuteron channel. We have received the calculated asymmetries in ${}^3\text{He}(\vec{e}, e'd)$ from three theory groups: the Bochum/Krakow, the Hannover/Lisbon and, most recently, the Pisa group. Since the calculations are numerically intensive, they have provided us only with calculations on a discrete grid of 35 kinematic points distributed over the acceptance of the electron arm (HRS spectrometer). Each kinematic point represents one combination of (E', θ_e) . For each such pair the asymmetries are calculated as functions of p_{miss} and ϕ_{dq} .

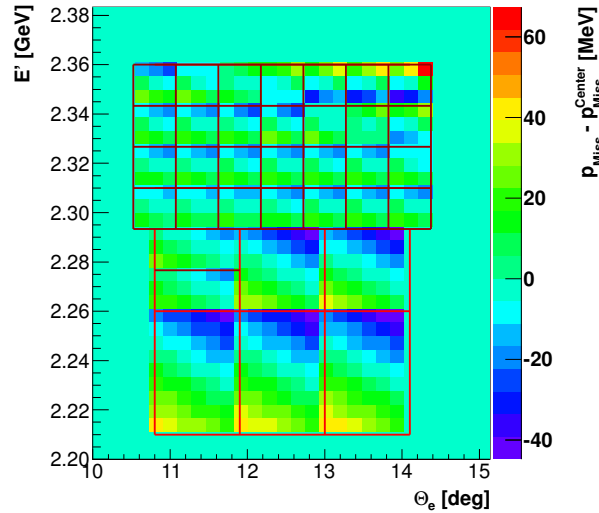


Figure 15: Deviations of p_{miss} from the values at the bin centers (where the theoretical calculations are available) in the (E', θ_e) region used for averaging of the theories over the experimental acceptance.

In this report we describe an important alteration of the previous averaging procedure. Initially, the following method was used. From the measured data we determined all relevant kinematic variables E' , θ_e , p_{miss} , and ϕ_{dq} for each event. We then checked whether the theoretical asymmetry is actually available for the event under consideration: if the event was within the corresponding rectangular area in the 35-point (E', θ_e) mesh, the theoretical asymmetry *at the center* of that rectangle was assigned to the event. Subsequently, we had to check whether the calculation exists for the given p_{miss} of the actual event since not all values of p_{miss} are available at all kinematic points. If the calculation existed, the event was accepted and the theoretical asymmetry for the given set of kinematic variables was computed. The final theoretical

asymmetry as a function of p_{miss} was obtained by averaging the asymmetries over all events in each p_{miss} bin.

The advantage of this method was that the measured data and the computed asymmetries were compared on an equal footing, since the experimental asymmetry was determined by using only the data for which theoretical calculations exist. But this procedure had many handicaps. By selecting only events that can be furnished with the corresponding theoretical asymmetry we have lost a huge fraction of the events. In addition, when calculating the theoretical asymmetry, we have always considered the event as coming from the bin center. This induces certain problems because our kinematic bins are quite large. For example, in each bin the minimal reachable p_{miss} can be up to 40 MeV/ c lower than the minimal p_{miss} available at the bin center, as shown in Fig. 15. This is problematic at low p_{miss} , because it forces us to throw away statistics. Neglecting low- p_{miss} data in some bins can also lead to variations in the final average values of the asymmetries.

Furthermore, if an event comes from near the edge of the selected bin, the theories from the neighboring bins are almost equally valid as the one belonging to the chosen bin: the closer one approaches the edge of a bin, the more important the neighboring bins become. Hence, we need to correctly decide which theory we are going to consider and how.

All these questions and problems have led us to develop a new method for comparing the data to the simulation. The main goal of this new approach is to keep as much as possible of the measured data by avoiding unnecessary cuts. We do not want to make the data conform to the theory but vice-versa. This means that one needs to extend the p_{miss} range of the calculations in order to match the larger range spanned by the measured data. This has been achieved by extrapolating the calculations to smaller values of p_{miss} , which is not trivial as the p_{miss} -dependence of the asymmetries is far from linear. However, since typical extrapolations of not more than approximately 20 MeV/ c are needed, the procedure is not expected to introduce large systematic errors.

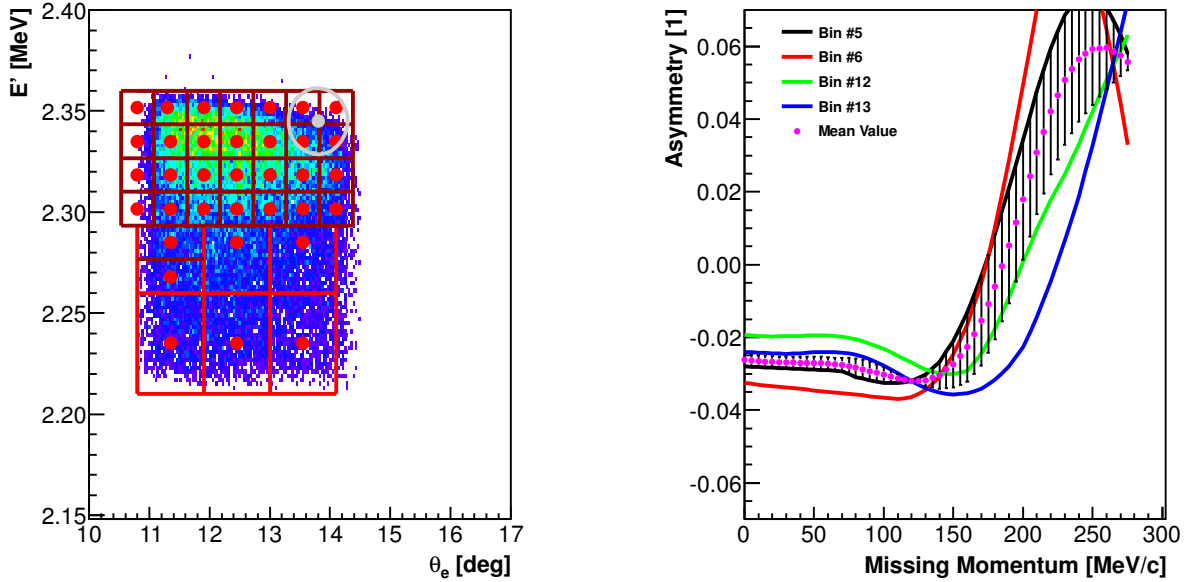


Figure 16: Averaging of the theoretical asymmetries for the ${}^3\text{He}(\vec{e}, e'd)$ channel. Left: selection of neighboring bins for a chosen event (gray point at the intersection of four regions) and its neighborhood (gray circle) used to weigh the corresponding theoretical predictions in the adjacent four bins. Right: weighted predicted asymmetries from all four bins encompassed by the gray circle. The resulting averaged interpolated asymmetry (magenta points with uncertainties corresponding to the averaging procedure) now extends to $p_{\text{miss}} = 0$.

To obtain the best possible estimate for the asymmetries in the low- p_{miss} region we defined the negative p_{miss} axis by exploiting the fact that $A(-p_{\text{miss}}, \phi_{\text{dq}}) = A(p_{\text{miss}}, 180^\circ + \phi_{\text{dq}})$. By such mirroring of the asymmetries to the negative p_{miss} -axis the extrapolation of the asymmetries to zero turns into a more

reliable interpolation that connects the two branches of the asymmetries at positive and negative p_{miss} across the $p_{\text{miss}} = 0$ axis. We have assumed that the asymmetries have a modest dependence on p_{miss} in the interpolation region, a view supported by theoretical calculations for the bins where the asymmetries at very low p_{miss} are available a priori.

Once the (interpolated) calculated asymmetries have been made available for all required p_{miss} , we use each measured event in the following procedure. First, we take into account not only the theoretical value at the center of the event's bin, but also the values from the neighboring regions in the (E', θ_e) plane. We select a neighborhood around each event (see e.g. the gray circle surrounding an event at the intersection of four kinematic regions in Fig. 16 (left)). The size of the circle is chosen such that for each event the closest theoretical predictions are selected, i.e. the radius of the circle is approximately the same as the linear size of the region. Then we check which theories are available in the selected zone; in the example shown, the algorithm picks the theories from all four neighboring bins. The distance of the event to each of the considered bin centers is calculated, and these distances are then used as weights in the calculation of the average of all theories available inside the selected zone defined by the event, i.e. larger distances imply smaller contributions of a particular kinematic point to the average asymmetry. We also calculate the difference from the average asymmetry to the nearest predicted asymmetry, and take this as a measure for the systematic uncertainty introduced by our approach. This uncertainty is in no way related to the quality of the theoretical calculations themselves; it is solely a consequence of our averaging procedure and the fact that the theory is available only at discrete points. The final result for the p_{miss} -dependence of the asymmetry is shown in Fig. 16 (right) for the 5, 6, 12, 13 bin quartet. The whole algorithm is repeated for each event. Finally, the asymmetries are accumulated and averaged in each p_{miss} bin.

References

- [1] S. Širca, S. Gilad, D. W. Higinbotham, W. Korsch, B. E. Norum (spokespersons), *Measurement of A'_x and A'_z asymmetries in the quasi-elastic ${}^3\vec{\text{He}}(\vec{e}, e'd)$* , TJNAF Experiment E05-102.
- [2] M. Mihovilović et al. (Hall A Collaboration), *Methods for optical calibration of the BigBite hadron spectrometer*, Nucl. Instr. Meth. A **686** (2012) 20.

3.4 E06-010: Measurement of Single Target-Spin Asymmetry in Semi-Inclusive Pion Electroproduction on a Transversely Polarized ^3He Target

J.-P. Chen, E. Cisbani, H. Gao, X. Jiang, J.-C. Peng co-spokespersons,
and
the Hall A Collaboration.

contributed by K. Allada, X. Yan, and Y.X. Zhao

3.4.1 Introduction

Experiment E06010 (Transversity) [1] was conducted in Hall A from Oct. 2008 to Feb. 2009 using a longitudinally polarized beam and transversely polarized ^3He target. The beam energy was 5.9 GeV. The primary goal of the experiment was to extract Collins and Sivers moments in the semi-inclusive deep inelastic (SIDIS) reaction, $^3\text{He}^\uparrow(e, e'\pi^\pm)X$. The beam helicity was flipped at 30 Hz and the target spin direction was flipped every 20 minutes. One can either perform target single spin asymmetry (TSSA) study by summing the two beam helicity states to achieve unpolarized beam, or do beam-target double spin asymmetry (DSA) study. The BigBite spectrometer was set at 30° on beam-right to detect scattered electron with momenta from 0.6-2.5 GeV. The left HRS [2] was set at 16° on beam-left to detect the produced hadrons (π^\pm , K^\pm and proton) with a fixed momentum of 2.35 GeV.

There were four types of physics triggers (see Table 1). The coincidence trigger (T5) was used for the primary analysis, which included SSA and DSA analysis to obtain the Collins/Sivers moments [3] and A_{LT} moments [4] for charged pions, respectively. These two results were published in [3, 4]. The following are some of the recent progresses in E06-010 physics analysis:

- The results of SSA in the inclusive hadron production reaction, $e + ^3\text{He}^\uparrow \rightarrow hX$ ($h = \pi^\pm, K^\pm, p$), have been submitted for a publication [7]. This analysis was performed by Kalyan Allada (MIT) and independently checked by Yuxiang Zhao (USTC, China).
- The final analysis of pretzelosity asymmetry for charged pions, extracted from the TSSA data in the SIDIS reaction $^3\text{He}^\uparrow(e, e'\pi^\pm)X$, is finished. The results were submitted for a publication. This analysis was performed by Yi Zhang (Lanzhou University, China)
- Results of Collins and Sivers moments for charged Kaons in SIDIS reaction $^3\text{He}^\uparrow(e, e'K^\pm)X$ are final, and a draft for publication is being prepared. This analysis was performed by Youcai Wang (UIUC) and independently checked by Yuxiang Zhao (USTC, China).
- The preliminary results of DSA in inclusive hadrons production reaction, $e + ^3\text{He}^\uparrow \rightarrow hX$, ($h = \pi^\pm, K^\pm, p$) from HRS data were obtained. The analysis is currently focused on producing final results for this channel. This analysis is being performed by Yuxiang Zhao (USTC, China).
- Analysis of unpolarized SIDIS cross-section to access the Boer-Mulders function and to study the $x - z$ factorization. This work is being performed by Xuefei Yan (Duke University).

In this report we will discuss some of the on-going analysis from the list above.

Trigger type	Description
1	Low threshold on BigBite lead-glass
3	Left HRS singles (S1 .and. S2)
5	Coincidence between BigBite and Left HRS (T1 .and. T3)
6	High threshold on BigBite lead-glass

Table 1: Summary of physics triggers in E06010

3.4.2 SSA in Inclusive Hadron Production

Our primary results were focused on the SIDIS reaction to study transverse momentum dependent parton distribution functions (TMDs). In addition to SIDIS reaction one can study inclusive hadron production reaction where the scattered electron remains undetected. We obtained the SSA from $e + {}^3\text{He}^\uparrow \rightarrow hX$ reaction using the HRS data for π^\pm , K^\pm and protons.

The target SSA is defined as,

$$A_{UT}(x_F, p_T) = \frac{1}{P} \frac{d\sigma^\uparrow - d\sigma^\downarrow}{d\sigma^\uparrow + d\sigma^\downarrow} \sin\phi_S = A_N \sin\phi_S, \quad (3)$$

where $d\sigma^{\uparrow(\downarrow)}$ is the differential cross-section in the target “up” (“down”) state, P is the target polarization, and ϕ_S is the angle between the scattering plane and the nucleon spin vector.

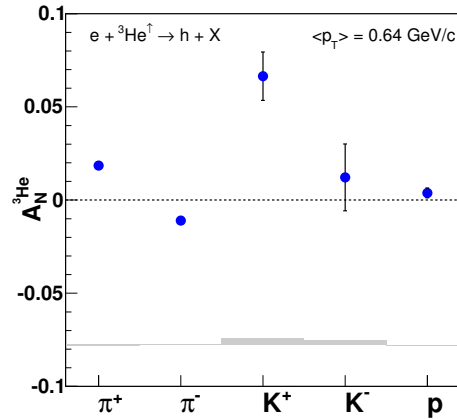


Figure 17: Inclusive SSA results on a ${}^3\text{He}$ target for π^\pm , K^\pm and protons in the vertical target spin configuration ($\phi_S = \pm 90^\circ$). The error bars on the points represents the statistical uncertainty. The grey band shows the magnitude of the overall systematic uncertainty for each hadron channel.

The final ${}^3\text{He}$ asymmetry results are shown for different hadron species in Fig. 17. The center-of-mass energy was $\sqrt{s}=3.45$ GeV, and the average p_T for this data was 0.64 GeV/c. For the high statistics pion sample the SSA was divided into five bins in p_T . The SSAs for charged pions as a function of p_T for a ${}^3\text{He}$ target are shown in Fig. 18 (left). A first attempt to extract the neutron SSA from the ${}^3\text{He}$ was done using effective polarization approach. The final results for A_N^n for charged pions on an effective neutron target are shown in Fig. 18 (right) [7].

3.4.3 Pretzelosity Asymmetry

There are three leading-twist terms that appear in the SIDIS cross-section (σ_{UT}) obtained from an unpolarized beam and a transversely polarized target. The first two are Collins and Sivers terms which were studied in our earlier analysis [3, 4]. The third term is known as pretzelosity (h_{1T}^\perp), one of the least known TMDs. In a class of relativistic quark models [8, 9], pretzelosity can be expressed as the difference between the helicity and the transversity, and can be intuitively related to orbital angular momentum of quarks.

The SSA data from SIDIS reaction ${}^3\text{He}^\uparrow(e, e'\pi^\pm)X$ was binned in ϕ_S and ϕ_h , the spin and hadron angle, respectively. The pretzelosity asymmetry was obtained by performing a 2D fitting in the ϕ_S and ϕ_h using three terms (Collins, Sivers and Pretzelosity) in the fitting function. The extracted pretzelosity asymmetries on ${}^3\text{He}$ target for charged pions are shown in Fig. 19. To extract the pretzelosity asymmetry on the neutron, the effective polarization method was used. The results of the extracted pretzelosity moment on the neutron are shown in the bottom two panels of Fig. 19 and are compared with various models.

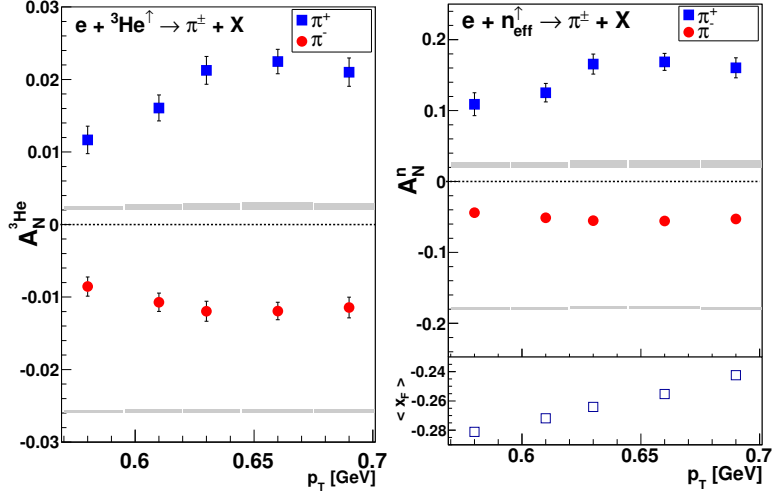


Figure 18: Left: A_N results on a ${}^3\text{He}$ target for the π^\pm channel as a function of p_T . Right: A_N results on a neutron target extracted from the measured ${}^3\text{He}$ asymmetries. The solid band on the bottom of each panel shows the magnitude of the systematic uncertainty for each momentum bin. The lower plot shows the x_F and p_T correlation in this measurement.

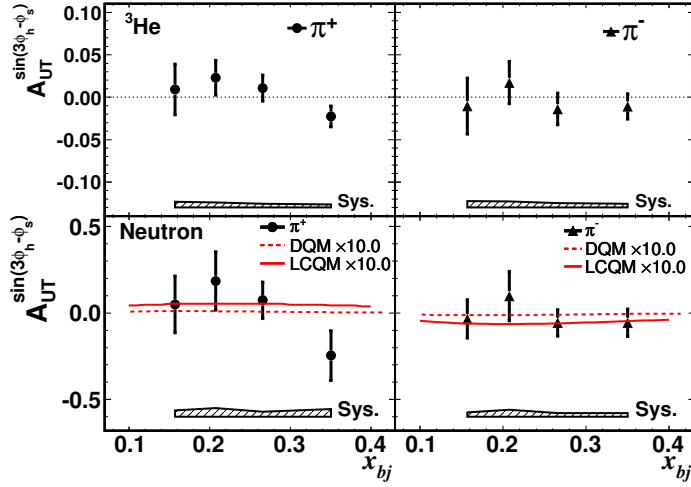


Figure 19: The extracted pretzelosity asymmetries on ${}^3\text{He}$ nuclei (top panels) and on the neutron (bottom panels) are shown together with uncertainty bands for both π^+ and π^- electroproduction.

3.4.4 SSA of Kaon in SIDIS

The HERMES experiment [11] observed that the Collins effect for K^+ is larger than that for π^+ on proton target, whereas for K^- it is small and consistent with zero. The Siverts effect reported by the HERMES experiment shows that the K^+ asymmetry is larger than K^- asymmetry on proton target. It is also important to note that the K^\pm Collins and Siverts moments from the COMPASS experiment on deuteron target are consistent with zero, suggesting large cancellations between contributions from proton and neutron. Our results from polarized ${}^3\text{He}$ data will provide crucial independent information on Kaon Collins and Siverts moments.

In this section, we report the preliminary results of single-spin asymmetries of charged kaons produced

in semi-inclusive deep inelastic scattering of electrons from a transversely polarized ${}^3\text{He}$ target. Both the Collins and the Sivers moments for K^+ and K^- are extracted over the kinematic range of $0.05 < x < 0.5$.

The electron identification was achieved by using cuts on the BigBite pre-shower energy E_{ps} and the ratio E/p of the total pre-shower and shower energy to the reconstructed momentum. After all the cuts, π^- contamination was controlled to be less than 1%. Left HRS was configured for hadron detection. In addition to three Cherenkov detectors (CO_2 gas Cherenkov detector, Aerogel detector (A1) and RICH), coincidence time of flight (CTOF) between HRS and BigBite was also used to perform the hadron PID. During E06010, RICH performance was not optimal, its efficiency was very low and kaon yield itself is relatively small, so kaon identification was relied on CTOF, and RICH was used as a cross-check. Figure 20 shows the CTOF spectrum with a veto on A1 to suppress the pion background. After combining all the HRS cuts and CTOF cut, $\pi^+(\pi^-)$ contamination in $K^+(K^-)$ sample was controlled to be less than 2%(5%). Random contamination in $K^+(k^-)$ sample is less than 4%(1%). Total number of $K^+(K^-)$ after PID cuts are 9481(1797).

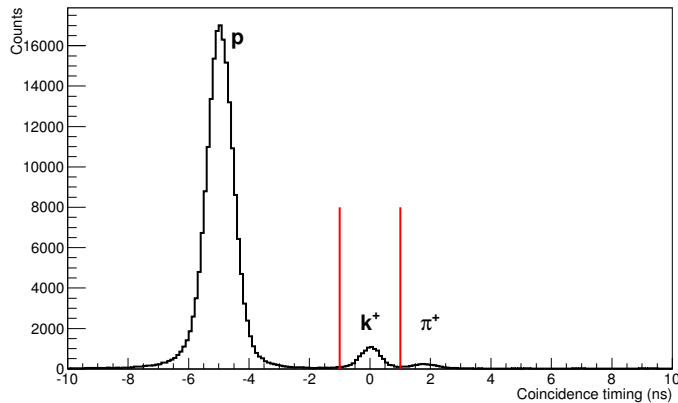


Figure 20: Coincidence ToF spectrum between BigBite and HRS with a veto cut on A1 detector to suppress the pion background. The red lines shows the Kaon selection cuts.

Preliminary Results Due to the low statistics for kaons, the data was averaged over full range of x_{bj} . The Collins and Sivers moments were extracted simultaneously by using Maximum Likelihood Estimation (MLE) [10], the preliminary results are shown in figure 21. K^+ Collins and Sivers asymmetries are consistent with zero within error bar, while k^- Collins and Sivers asymmetries favor negative sign.

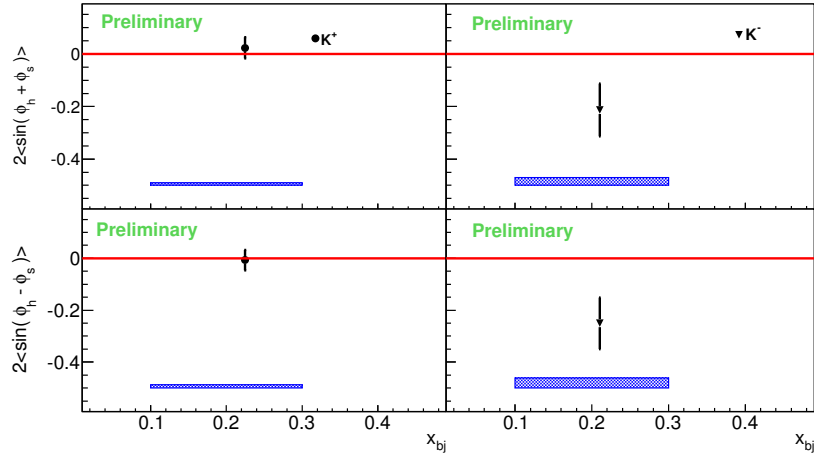


Figure 21: Preliminary results of Collins and Sivers moments on ${}^3\text{He}$ for kaon electro-production.

3.4.5 Unpolarized SIDIS Cross-Section

Most of the data analysis effort for experiment E06010 so far has been focused on single-spin asymmetry and double-spin asymmetry to extract information on various TMDs such as Collins, Sivers, Pretzelosity and Transversal Helicity (g_{1T}^q) [3, 4, 5]. Recently we started a new analysis on unpolarized differential cross-section from E06010 in order to access the Boer-Mulders function, which describes the distribution of transversely polarized quarks in an unpolarized nucleon. Moreover, we plan to study the $x - z$ factorization in SIDIS using unpolarized cross-section.

Unpolarized differential cross-section obtained from an unpolarized beam and an unpolarized target, is equivalent to a proper combination of differential cross-sections with different beam and target polarizations extracted from experiment E06010. An extraction of differential cross-section from experiment E06010 requires further study of the BigBite acceptance model in the existing SIMC-Transversity simulation. The BigBite acceptance is being studied by comparing the elastic H_2 calibration runs at 1.23 and 2.4 GeV, with the SIMC-Transversity simulation combined with a well-developed elastic electron-proton-scattering event generator with radiative effects included.

After the acceptance thoroughly studied and SIMC-Transversity simulation updated, the unpolarized differential cross-section of SIDIS will be extracted, from which the Boer-Mulders function can be obtained.

References

- [1] J.P. Chen, E. Cisbani, H. Gao, X. Jiang, and J.-C. Peng. http://www.jlab.org/exp_prog/CEBAF_EXP/E06010.html
- [2] J. Alcorn et al. Nucl. Instr. and Meth. A522, 294 2004
- [3] X. Qian et al. Phys. Rev. Lett., 107:072003 2011
- [4] J. Huang et al. Phys, Rev. Lett., 108:052001 2012
- [5] Y. Zhang et al. (submitted for publication).
- [6] J. Katich, X. Qian, Y.X. Zhao et al. arXiv:1211.0197 2013
- [7] K. Allada, Y.X. Zhao et al. arXiv:1311:1866 2013
- [8] H. Avakian, A. V. Efremov, P. Schweitzer, and F. Yuan Phys. Rev. D81 074035 2010

- [9] C. Lorce and B. Pasquini Phys. Lett. B710 486
- [10] J. Huang, Y. Qiang Note:Maximum Likelihood Estimation of Asymmetry and Angular Modulation for Transversity 2010
- [11] A. Airapetian et al. Phys. Lett. B693, 11 2010

3.5 E06-014: A Precision Measurement of d_2^n : Probing the Lorentz Color Force

S. Choi, X. Jiang, Z.-E. Meziani, B. Sawatzky, spokespersons,
and
the d_2^n and Hall A Collaborations.
Contributed by D. Flay.

3.5.1 Physics Motivation

3.5.1.1 d_2^n : Quark-Gluon Correlations in the Nucleon To date, extensive work has been done investigating the spin structure function g_1 within the context of the Feynman parton model and pQCD. However, far less is known about the g_2 structure function. It is known to contain quark-gluon correlations. It follows from a spin-flip Compton amplitude and may be written as:

$$g_2(x, Q^2) = g_2^{WW}(x, Q^2) + \bar{g}_2(x, Q^2), \quad (4)$$

where g_2^{WW} is the Wandzura-Wilczek term, which may be expressed entirely in terms of g_1 [1]:

$$g_2^{WW}(x, Q^2) = -g_1(x, Q^2) + \int_x^1 \frac{g_1(y, Q^2)}{y} dy. \quad (5)$$

The second term is given as:

$$\bar{g}_2(x, Q^2) = - \int_x^1 \frac{1}{y} \frac{\partial}{\partial y} \left[\frac{m_q}{M} h_T(y, Q^2) + \xi(y, Q^2) \right] dy, \quad (6)$$

where h_T is the transverse polarization density, and ξ is a term arising from quark-gluon correlations. Here, h_T is suppressed by the ratio of the quark mass m_q to the target mass M . Therefore, a measurement of \bar{g}_2 provides access to quark-gluon interactions inside the nucleon [2].

Additionally, a measurement of both g_1 and g_2 allows for the determination of the quantity d_2^n , which is formed as the second moment of a linear combination of g_1 and g_2 :

$$d_2^n(Q^2) = \int_0^1 x^2 [2g_1^n(x, Q^2) + 3g_2^n(x, Q^2)] dx = 3 \int_0^1 x^2 \bar{g}_2^n(x, Q^2) dx. \quad (7)$$

d_2^n also appears as a matrix element of a twist-3 operator in the operator product expansion [3]:

$$\langle P, S | \bar{\psi}_q(0) g G^{+y}(0) \gamma^+ \psi_q(0) | P, S \rangle = 2MP^+ P^+ S^x d_2^n, \quad (8)$$

where $G^{+y} = \frac{1}{\sqrt{2}}(B^x - E^y)$. We see from Equations 6–8 that d_2^n is a twist-3 matrix element that measures quark-gluon interactions.

Recent work has shown [4, 5] that at high Q^2 , d_2^n is seen as a color Lorentz force averaged over the volume of the nucleon. This is given by the expression for the transverse (color) force on the active quark immediately following its interaction with a virtual photon:

$$F^y(0) \equiv -\frac{\sqrt{2}}{2P^+} \langle P, S | \bar{\psi}_q(0) g G^{+y}(0) \gamma^+ \psi_q(0) | P, S \rangle = -\frac{1}{2} M^2 d_2^n. \quad (9)$$

This theoretical interpretation reveals how g_2 and subsequently d_2^n will allow us to examine the color interactions of the constituents inside the nucleon.

While bag and soliton model calculations of d_2 for the neutron yield numerical values consistent with those of lattice QCD, current experimental data differ by roughly two standard deviations (see the highest Q^2 data in Figure 22). One of the goals of our experiment is to improve the experimental error on the value of d_2^n by a factor of four. It subsequently provides a benchmark test of lattice QCD calculations, shown in Figure 22.

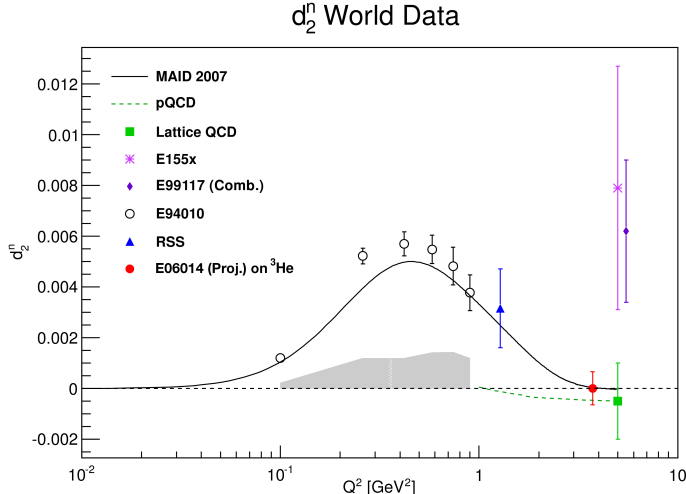


Figure 22: d_2^n as a function of Q^2 . All the data shown with the exception of the SLAC E155x data are dominated by resonance contributions. E06-014 data will be dominated by the deep inelastic scattering (DIS) contribution. The projected error from E06-014 [6] is shown, along with the lattice QCD result [7]. The dashed green curve shows the pQCD evolution from the lattice point [8] based on the calculations of [9, 10]. Data from JLab experiments E94-010 [11, 12] and RSS [13] are included in the plot. For comparison to the resonance contribution, a MAID model [14] is plotted. Also plotted is the total d_2 from SLAC experiment E155x [15], which consists of DIS data distributed over a large range in Q^2 .

3.5.1.2 A_1 : The Virtual Photon-Nucleon Asymmetry Another quantity of interest is the virtual photon-nucleon longitudinal spin asymmetry A_1 . It provides insight into the quark structure of the nucleon and can be defined as:

$$A_1(x, Q^2) \equiv \frac{\sigma_{1/2} - \sigma_{3/2}}{\sigma_{1/2} + \sigma_{3/2}}, \quad (10)$$

where the subscript 1/2 (3/2) gives the projection of the total spin of the virtual photon-nucleon system along the virtual photon direction corresponding to the nucleon's spin anti-parallel (parallel) to the virtual photon. Constituent quark models (CQM) and pQCD models predict A_1 to be large and positive at large x . Figure 23(a) shows the current world data compared to these models. It is seen that the CQM (yellow band [16]) describes the trend of the data reasonably well. The pQCD parameterization with hadron helicity conservation (dark blue curve [22])—assuming quark orbital angular momentum to be zero—does not describe the data adequately. However, the pQCD model allowing for quark orbital angular momentum to be non-zero (green curve [24]) describes the data well, pointing perhaps to the importance of quark orbital angular momentum in the spin structure of the nucleon.

Combining A_1^n data measured on a polarized effective neutron target with A_1^p data measured on a polarized proton target allows access to $\Delta u/u$ and $\Delta d/d$. Recent results from Hall A [20] and from CLAS [25] showed a significant deviation of $\Delta d/d$ from the pQCD predictions, which have that ratio approaching 1 in the limit of $x \rightarrow 1$ (Fig. 23(b)). As part of the 12 GeV program, two approved experiments (one in Hall A [26] and one in Hall C [27]) will extend the accuracy and x range of this measurement, but a measurement of A_1^n at the kinematics of this experiment (E06-014) will provide valuable support (or refutation) of prior JLab results, while producing additional input for theoretical models in advance of the coming experiments at 12 GeV.

3.5.2 The Experiment

The experiment ran in Hall A of Jefferson Lab from February to March of 2009, with two beam energies of $E = 4.74$ and 5.89 GeV, covering the resonance and deep inelastic valence quark regions, characterized by

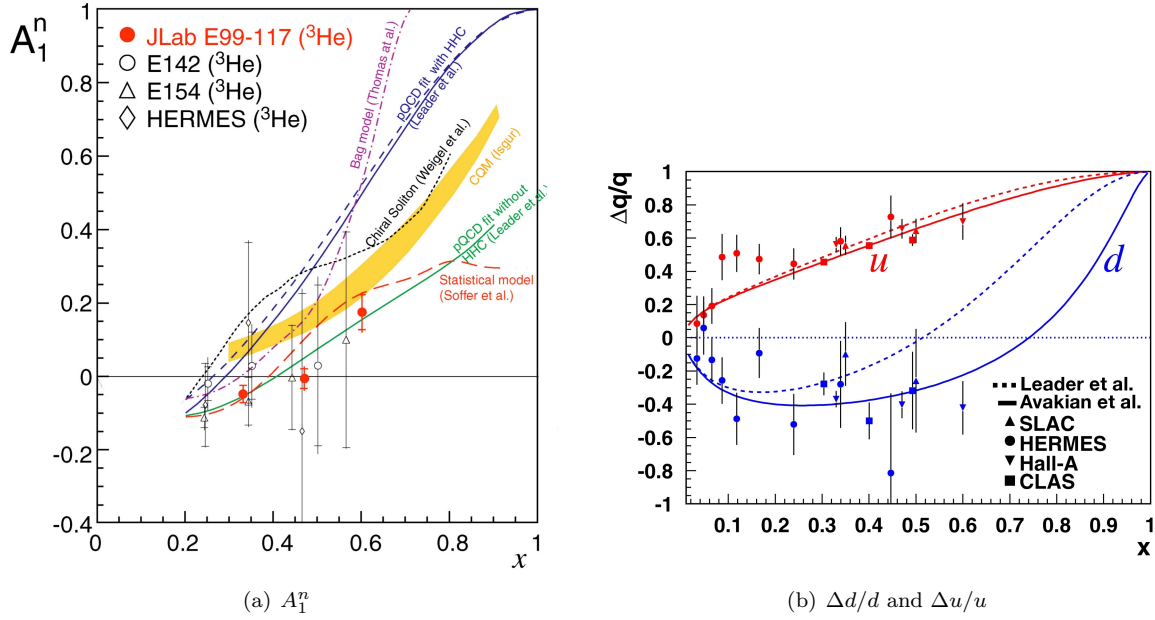


Figure 23: Current data for A_1^n , $\Delta d/d$ and $\Delta u/u$. (a): The current world data for the neutron A_1 from SLAC E143 [17] and E154 [18] and HERMES [19], along with JLab E99-117 [20]. Also shown are CQM models and various pQCD models. Figure adapted from [21]. (b): $\Delta q/q$ for the up (u) and down (d) quarks. The dashed curves represent a prediction from Leader *et al.* [22], while the solid curves show calculations by Avakian *et al.* [23]. The data shown are from HERMES, SLAC and JLab. Figure adapted from [23].

$0.2 \leq x \leq 0.7$ and $2 \text{ GeV}^2 \leq Q^2 \leq 6 \text{ GeV}^2$. The coverage in the x and Q^2 plane is shown in Figure 24.

In order to measure d_2^n , we scattered a longitudinally polarized electron beam off of a ^3He target in two polarization configurations – longitudinal and transverse. ^3He serves as an effective polarized neutron target since roughly 86% of the polarization is carried by the neutron. This is due to the two protons in the nucleus being primarily bound in a spin singlet state [28, 29].

We measured the unpolarized cross section σ_0 and the double-spin asymmetries A_{\parallel} and A_{\perp} . The cross section was measured by the Left High-Resolution Spectrometer (LHRS), while the asymmetries were measured by the BigBite Spectrometer. The LHRS and BigBite were oriented at scattering angles of $\theta = 45^\circ$ to the left and right of the beamline, respectively.

Expressing the structure functions entirely in terms of these experimental quantities, we have the expression for d_2 :

$$d_2 = \int_0^1 \frac{MQ^2}{4\alpha^2} \frac{x^2 y^2}{(1-y)(2-y)} \sigma_0 \left[\left(3 \frac{1+(1-y)\cos\theta}{(1-y)\sin\theta} + \frac{4}{y} \tan(\theta/2) \right) A_{\perp} + \left(\frac{4}{y} - 3 \right) A_{\parallel} \right] dx, \quad (11)$$

where $x = Q^2/2M\nu$, $\nu = E - E'$ is the energy transferred to the target, E' is the scattered electron energy, and $y = \nu/E$ is the fractional energy transferred to the target. The asymmetries are given by:

$$A_{\parallel} = \frac{N^{\downarrow\uparrow} - N^{\uparrow\uparrow}}{N^{\downarrow\uparrow} + N^{\uparrow\uparrow}} \quad \text{and} \quad A_{\perp} = \frac{N^{\downarrow\Rightarrow} - N^{\uparrow\Rightarrow}}{N^{\downarrow\Rightarrow} + N^{\uparrow\Rightarrow}},$$

where N is the number of electron counts measured for a given configuration of beam helicity (single arrows) and target spin direction (double arrows).

While d_2 was the main focus of the experiment, the measurement of the asymmetries allowed for the extraction of A_1 :

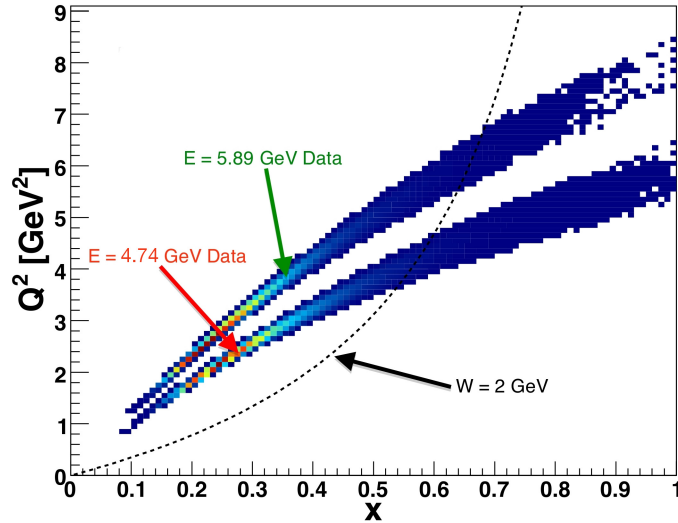


Figure 24: The E06-014 kinematic coverage in Q^2 and x . The lower band is the 4.74 GeV data set and the upper band is the 5.89 GeV data set. The black dashed line shows $W = 2$ GeV. The regions to the left and right of this line correspond to DIS and resonance kinematics, respectively.

$$A_1 = \frac{1}{D(1 + \eta\xi)} A_{\parallel} - \frac{\eta}{d(1 + \eta\xi)} A_{\perp}, \quad (12)$$

where D , η , ξ and d are kinematic factors [30].

3.5.3 Data Analysis Progress

3.5.3.1 Summary of Completed Work Nearly all of the analyses for E06-014 have been completed, including detector calibrations for both the LHRS and the BigBite spectrometer [34] and various background studies for the spectrometers relating to nitrogen dilution in the target and pair-produced electrons [35, 36].

The experiment used a polarized electron beam at energies of 4.74 and 5.89 GeV. The polarization of the electron beam was measured independently through Compton and Møller scattering, and the analysis of these measurements revealed a beam polarization of $\sim 72\%$ [36].

Knowledge of the target polarization is crucial when performing a double-spin asymmetry experiment. E06-014 used the standard Hall A polarized ^3He target with two holding field directions: longitudinal and transverse in plane, with respect to the electron beam direction. The target polarization was extracted through electron paramagnetic resonance (EPR). The longitudinal polarization was cross checked using nuclear magnetic resonance (NMR) measurements. During the running of the experiment, the polarization of the target was $\sim 50\%$ [36].

3.5.3.2 Unpolarized Cross Sections The LHRS was used to measure the unpolarized cross section. The analysis for the extraction of the experimental cross section, σ_{rad} , for the $E = 4.74$ GeV and 5.89 GeV data sets is shown in [35].

3.5.3.3 Unpolarized Cross Section Radiative Corrections Electrons lose energy due to interactions with material. This includes the material before and after the target, and the target material itself. These interactions will alter the electron's *true* incident energy and also its *true* scattered energy. This ultimately results in a different cross section than the true value. These effects are characterized by ionization (or Landau straggling) and bremsstrahlung. There are also higher-order processes at the interaction vertex that must also be considered. Collectively, the removal of these effects is called *radiative corrections*.

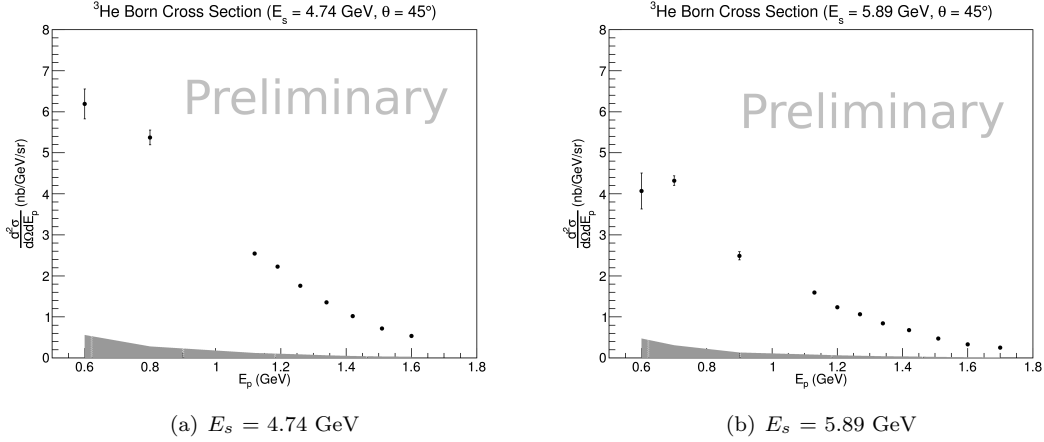


Figure 25: The ^3He Born cross sections. The error bars indicate the statistical error, while the band indicates the systematic error. (a): $E_s = 4.74$ GeV data; (b): $E_s = 5.89$ GeV data.

A first correction that must be done *before* carrying out the radiative corrections is to subtract the elastic radiative tail, since it is long and affects all states of higher invariant mass W [37]. For these kinematics, the elastic tail is small and affects the lowest bins in scattered electron energy E_p at the $\lesssim 1\%$ level. The elastic tail was computed using the ROSETAIL code [38]. The model used for the elastic ^3He form factors was from Amroun [39].

The ^3He quasi-elastic tail, however, is much larger. The quasi-elastic radiative tail was computed by utilizing an appropriate model of the ^3He quasi-elastic cross section [40] and applying radiative effects [41]. The tail was then subtracted from the data. The model was checked against existing quasi-elastic ^3He data covering a broad range of kinematics.

In considering the effects mentioned above, the *measured* cross section is realized in terms of a triple integral:

$$\sigma_{\text{rad}}(E_s, E_p) = \int_0^T \frac{dt}{T} \int_{E_s^{\text{min}}}^{E_s} dE'_s \int_{E_p}^{E_p^{\text{max}}} dE'_p I(E_s, E'_s, t) \sigma_r(E'_s, E'_p) I(E_p, E'_p, T-t), \quad (13)$$

where σ_{rad} is the measured (radiated) cross section, σ_r is the *internally*-radiated cross section. E_s is the incident electron energy, E_p is the scattered electron energy. $I(E_0, E, t)$ is the probability of finding an electron with incident energy E_0 that has undergone bremsstrahlung with energy E at a depth t inside a material [37, 41].

In order to *unfold* the Born cross section, an iterative procedure is carried out in RADCOR [42]. It amounts to calculating:

$$\sigma_b^i = \frac{1}{C} \left[\sigma_{\text{rad}} - \int (\dots) dE'_s - \int (\dots) dE'_p \right], \quad (14)$$

where C and the two integrals are defined in Equation IV.2 in [37]. σ_b^i is the Born cross section obtained for the i^{th} iteration of the code, σ_{rad} is the radiated cross section to be corrected. σ_b^i is then re-inserted into equation for the next iteration. It was found that the calculation converges within the first 3–4 iterations. Figure 25 shows the resulting Born cross sections.

In E06-014, we took data for only two E_s values of 4.74 GeV and 5.89 GeV. However, we need enough data to properly calculate the integrals above. Therefore, we used a suitable cross section model [43] to fill in the rest of the phase space for each data set.

3.5.3.4 Unpolarized Cross Section Systematic Errors There are a number of contributions to the systematic errors on the cross section calculation [36]. We will focus our discussion on the radiative corrections.

The systematic errors corresponding to the radiative corrections include the elastic and quasi-elastic tail subtraction, material thicknesses in the electron’s path, and dependence on the input model used for the radiative correction calculations.

The systematic error of subtracting the elastic tail from the data is $\ll 1\%$, determined by considering different models for the elastic ${}^3\text{He}$ form factors.

In a similar fashion as the elastic tail, the systematic effect of the subtraction of the quasi-elastic tail was determined by considering different quasi-elastic cross section models to compute the tail. We found that the error is $\approx 5\text{--}6\%$ for the lowest bin in E_p , and falls to $\approx 1\%$ for all other bins for which we have data.

To determine the error related to the material thicknesses in the electron’s path, we varied the thicknesses in our calculations by up to 10%, and saw a change in our resulting Born cross section of $\lesssim 1.5\%$.

The error corresponding to the input model used in the radiative correction procedure was determined by using different models. The resulting Born cross section changed by at most $\approx 5\%$ for the lowest bin in E_p and dropped to $\lesssim 1\%$ for all other bins.

3.5.3.5 The Double-Spin Asymmetries The BigBite spectrometer was used to measure the parallel and perpendicular double-spin asymmetries between longitudinally polarized electrons and a longitudinally or transversely polarized ${}^3\text{He}$ target. These asymmetries were then corrected for imperfect beam and target polarizations. Corrections were also made for dilution effects due to the presence of N_2 in the target [32], and contamination due to pions and pair-produced electrons. The full details of these analyses may be found in [35, 36].

3.5.3.6 Asymmetry Radiative Corrections To compute the radiative corrections for asymmetries, we utilized the radiative correction code RADCOR mentioned in 3.5.3.3. To do this, we carried out the corrections on polarized cross section differences, $\Delta\sigma$, related to asymmetries by:

$$\Delta\sigma_{\parallel,\perp}^r = 2\sigma_0^r A_{\parallel,\perp}^r, \quad (15)$$

where $A_{\parallel,\perp}$ indicates a radiated asymmetry where the target is polarized either parallel (\parallel) or perpendicular (\perp) with respect to the incident electron beam momentum. The unpolarized cross section is σ_0^r , where the r indicates that radiative effects have been applied. We used the F1F209 [43] model for the unpolarized cross section. After the data have been converted to polarized cross section differences, they are imported into the RADCOR code in a similar fashion as was done for the unpolarized cross sections. The difference here, however, is that a model for the polarized cross section differences is needed to complete the integrals mentioned in Equation 14. This model consists of three components describing different kinematic regions: DIS, the quasi-elastic region, and the resonance region. The model used for the DIS region was the DSSV global analysis parton distribution function (PDF) model [44], which describes world data quite well in our kinematic region of interest. For the quasi-elastic region, we utilized P. Bosted’s nucleon form factors [45], smeared by a quasi-elastic scaling function [46] to simulate the nuclear effects of ${}^3\text{He}$. Putting together the nucleon form factors and the smearing function yields a quasi-elastic $\Delta\sigma$ which fits world data well. For the resonance region, we used the MAID model [14], which adequately describes world data. Putting the DIS, quasi-elastic and resonance contributions together, we built up an appropriate $\Delta\sigma$ that describes the physics to a reasonable level, an example of which is shown in Figure 26 where we compare our model to JLab E94-010 data [11, 12]. In the radiative correction procedure, the quasi-elastic tail was not subtracted first, but rather included in the integration. The elastic tail was found to be very small and was not subtracted.

To minimize statistical fluctuations in the radiative corrections, the corrections were done to a model of our data set. After obtaining the Born $\Delta\sigma$ from RADCOR, the corresponding asymmetry was obtained by inverting Equation 15 (but using the *Born* σ_0) to find A . Then, the size of the radiative correction at the asymmetry level was determined as:

$$\Delta A = A_b - A_r, \quad (16)$$

where A_b is the Born asymmetry and A_r is the radiated asymmetry. This ΔA was applied to our data for both the parallel and perpendicular cases as an additive correction. The size of the radiative correction as a function of x is shown in Figure 27. The red band indicates the systematic error, which is discussed in Section 3.5.3.7.

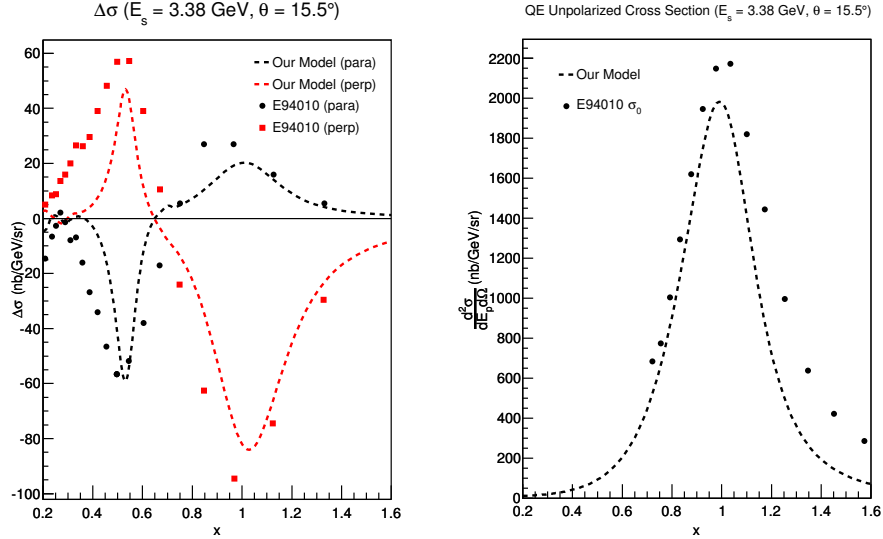


Figure 26: Our model of $\Delta\sigma_{\parallel,\perp}$ as compared to JLab E94-010 data. Our model consists of combining a smeared version of P. Bosted’s nucleon form factors to describe the quasi-elastic region and the MAID model for the resonance region. The DIS region is modeled using the DSSV PDFs.

The Born asymmetries for our data and their systematic errors are shown in Figure 28. The error bars indicate the statistical errors, while the colored bands indicate the systematic errors, which were obtained by varying all of the inputs needed¹ to extract the asymmetries within reasonable limits and observing the change in the asymmetry.

3.5.3.7 Asymmetry Radiative Correction Systematic Errors To investigate the systematic errors for the radiative corrections, there are two main contributions to consider: material thicknesses and model dependence.

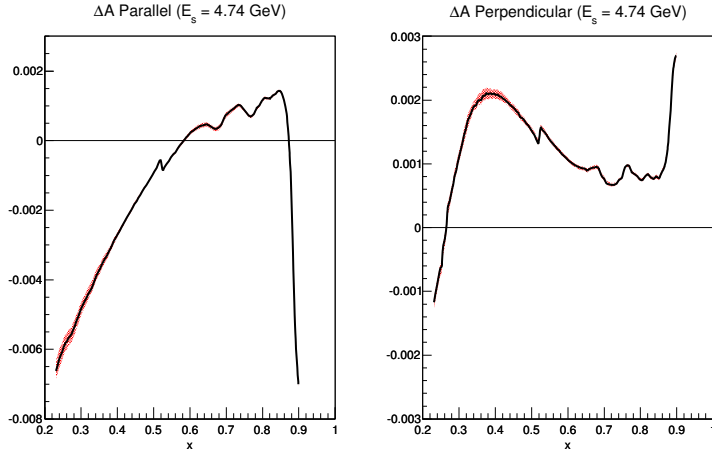
To address the first consideration, the thicknesses, they were changed by $\pm 10\%$ and the result was compared to the unmodified result. The change was found to be $\lesssim 1.5\%$, similar to what was seen for the unpolarized cross sections.

The model dependence of the radiative corrections was determined as follows: the input spectra to the integrals were varied *at random* by $\pm 10\%$ for 30 trials, and the size of the correction changed by $\lesssim 5\%$.

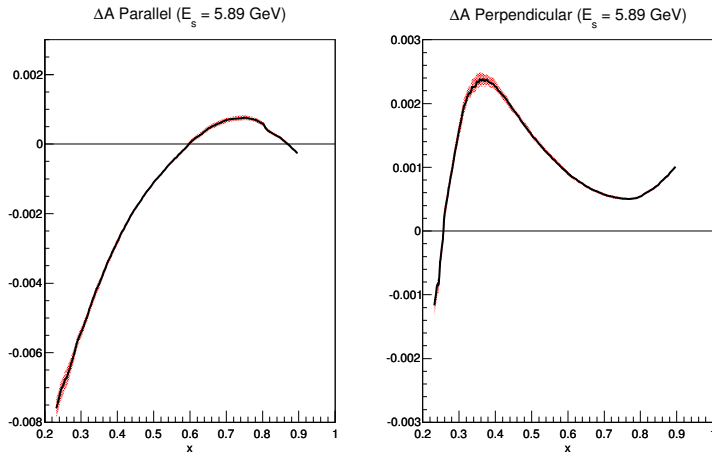
3.5.4 Preliminary Physics Results

3.5.4.1 The Virtual Photon-Nucleon Asymmetry Figure 29 shows the preliminary results for $A_1^3\text{He}$ at $E = 4.74$ and 5.89 GeV, respectively. Also shown are world data from SLAC E142 [47] and JLab E01-012 [48] and E99-117 [20]. The red (blue) data points indicate our $E = 4.74$ GeV ($E = 5.89$ GeV) data. The error bars on the world data are the in-quadrature sum of the statistical and systematic errors, while the error bars on our data are statistical only. The colored bands at the bottom of the plot indicate the systematic errors. The systematic errors were determined by varying all of the inputs to the computation of $A_1^3\text{He}$ to reasonable levels and observing the change in the asymmetry. The gray band represents various global analyses [22, 44, 51, 52, 53, 54, 55]. The data from this experiment are consistent with the world data across a wide range in x , despite the larger error bars in the resonance region, which corresponds to $x > 0.519$ (0.623) for $E = 4.74$ GeV (5.89 GeV).

¹Such quantities include the electron cuts, the nitrogen dilution factor, beam and target polarizations, and pion and pair production contamination factors.



(a) $E = 4.74$ GeV



(b) $E = 5.89$ GeV

Figure 27: The size of the radiative correction on the asymmetries, defined as $\Delta A = A_b - A_r$. The red band indicates the systematic error associated with the correction, see Section 3.5.3.7. The ΔA shown in these plots are applied to the data as an additive correction to obtain the Born asymmetry. (a): $E = 4.74$ GeV data; (b): $E = 5.89$ GeV data.

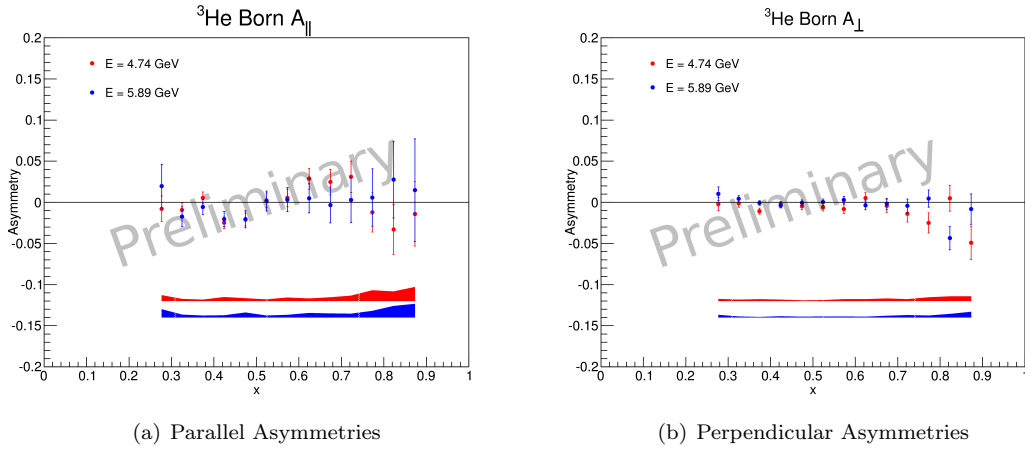


Figure 28: The Born asymmetries for $E = 4.74$ GeV (red) and $E = 5.89$ GeV (blue). The error bars indicate the statistical errors, while the colored bands show the systematic errors. (a): parallel asymmetries; (b): perpendicular asymmetries.

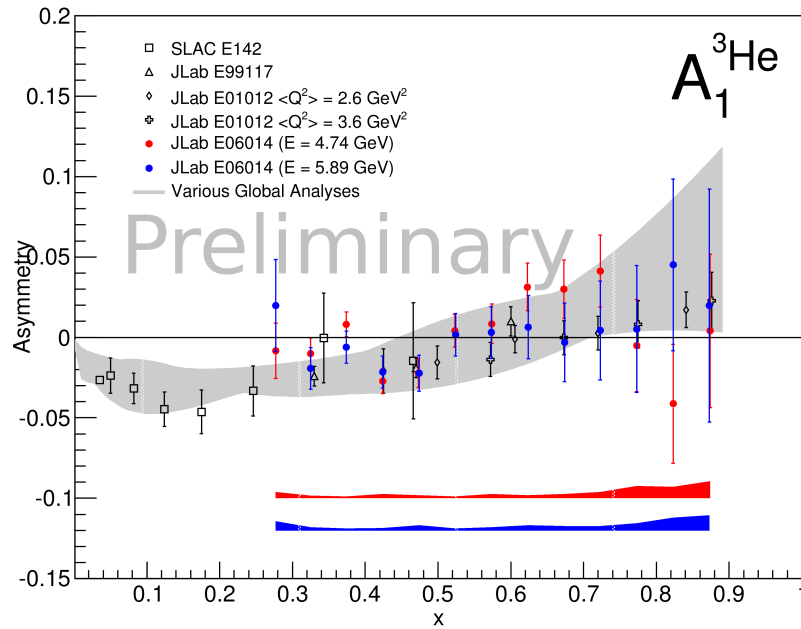


Figure 29: $A_1^{{}^3\text{He}}$ compared to the world data from SLAC E142 [47] and JLab E01-012 [48] and E99-117 [20]. The error bars on the world data indicate the in-quadrature sum of statistical and systematic errors, while the error bars on our data are statistical only. The colored bands at the bottom of the plot show the systematic errors. The gray band shows an envelope of various global analyses [22, 44, 51, 52, 53, 54, 55].

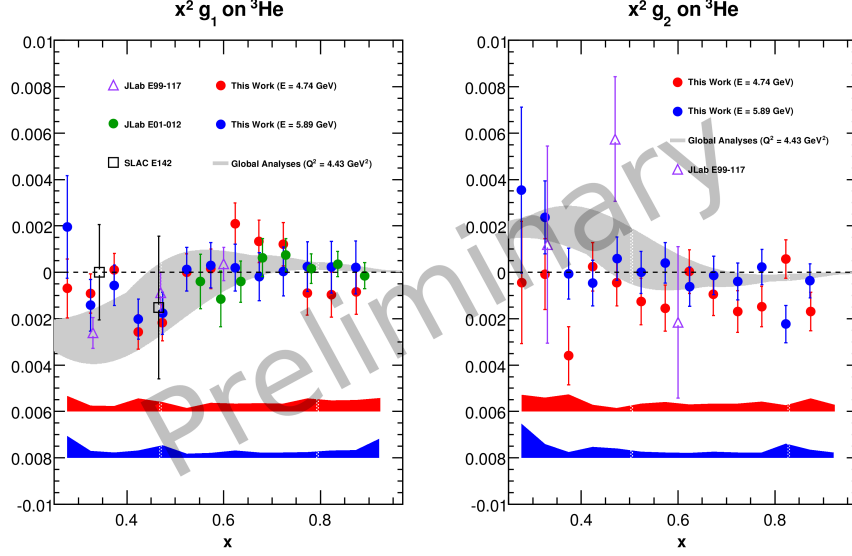


Figure 30: Preliminary results for the spin structure functions g_1 and g_2 on a ^3He target for $E = 4.74$ GeV (red) and 5.89 GeV (blue) compared to the world data [47, 48, 20] and various global analyses [22, 44, 51, 52, 53] represented by the gray band. The error bars on our data are statistical only; the colored bands at the bottom of the plot indicate the systematic errors.

3.5.4.2 The Spin Structure Functions En route to extracting d_2^n , the spin structure functions g_1 and g_2 can be obtained according to:

$$g_1 = \frac{MQ^2}{4\alpha^2} \frac{2y}{(1-y)(2-y)} \sigma_0 [A_{\parallel} + \tan(\theta/2) A_{\perp}] \quad (17)$$

$$g_2 = \frac{MQ^2}{4\alpha^2} \frac{y^2}{(1-y)(2-y)} \sigma_0 \left[-A_{\parallel} + \frac{1 + (1-y) \cos \theta}{(1-y) \sin \theta} A_{\perp} \right], \quad (18)$$

The preliminary results for g_1 on ^3He and g_2 on ^3He are shown in Figure 30, which compares the data to various models represented by the gray band [22, 44, 51, 52, 53] and the world data. The systematic errors on our data were obtained by varying all of the inputs needed to compute g_1 and g_2 to reasonable levels and observing the change in the result.

3.5.5 Current and Future Work

At present, we are working on finalizing our analysis to evaluate d_2^n and A_1^n . Additionally, from d_2^n we can extract the color electric and magnetic forces [3, 4, 5]. From our A_1^n data, we can also perform a flavor decomposition to obtain the quantities $\Delta u/u$ and $\Delta d/d$.

References

- [1] S. Wandzura and F. Wilczek, Phys. Lett. B **72**, 2 (1977).
- [2] R.L. Jaffe, Comm. Nucl. Part. Phys. **19**, 239 (1990).
- [3] B.W. Filippone and Xiandong Ji, Adv. Nucl. Phys. **26**, 1 (2001). arXiv:0101224v1 [hep-ph].
- [4] M. Burkardt, *The g_2 Spin Structure Function* (2009), arXiv:0905.4079v1 [hep-ph].

- [5] M. Burkardt, *Parton Distributions in the Impact Parameter Space* (2008), arXiv:0902.0163v1 [hep-ph].
- [6] S. Choi, X. Jiang, Z.-E. Meziani, B. Sawatzky *et al.*, Jefferson Lab PAC E06-014 (2005).
- [7] M. Gockeler *et al.*, Phys. Rev. D **72**, 054507 (2005).
- [8] P. Solvignon, private communication.
- [9] E. V. Shuryak and A.I. Vainshtein, Nucl. Phys. B **201**, 141 (1982).
- [10] Ji and Chou, Phys. Rev. D **42**, 3637 (1990).
- [11] M. Amerian *et al.*, Phys. Rev. Lett. **89**, 242301 (2002).
- [12] K. Slifer *et al.*, Phys. Rev. Lett. **101**, 022303 (2008)
- [13] K. Slifer *et al.*, *Resonance Spin Structure*, 2008. arXiv:0812.0031.
- [14] D. Drechel, S.S. Kamolov and L. Tatar, Eur. Phys. J. **A34**, 69 (2007).
- [15] P.L. Anthony *et al.*, Phys. Lett. B **553**, 18 (2003).
- [16] N. Isgur, Phys. Rev. D **59**, 0340123 (1999).
- [17] K. Abe *et al.*, SLAC-PUB-7753 (Feb. 1998).
- [18] K. Abe *et al.*, Phys. Rev. Lett. **79**, 26 (1997); Phys. Lett. B **405**, 180 (1997).
- [19] K. Ackerstaff *et al.*, Phys. Lett. B **404**, 383 (1997).
- [20] X. Zheng *et al.*, Phys. Rev. C **70**, 065207 (2004).
- [21] X. Zheng *et al.*, Phys. Rev. Lett **92**, 012004 (2004).
- [22] E. Leader, A.V. Siderov, D.B. Stamenov, Int. J. Mod. Phys **A13**, 5573 (1998).
- [23] H. Avakian, S. Brodsky and A. Deur *et al.*, Phys. Rev. Lett. **99**, 082001 (2007).
- [24] J.P. Ralson, P. Jain, R.V. Buniy, AIP Conf. Proc. **549**, 302 (2000).
- [25] K.V. Dharmawardane *et al.*, Phys. Lett. B **641**, 11 (2006).
- [26] G. Cates, N. Liyanage, Z.-E. Meziani, G. Rosner, B. Wojtsekhowski, X. Zheng *et al.*, Jefferson Lab PAC E1206122 (2006).
- [27] G. Cates, J.P. Chen, Z.-E. Meziani, X. Zheng *et al.*, Jefferson Lab PAC E1210101 (2010).
- [28] J.L. Friar *et al.*, Phys. Rev. C **42**, 6 (1990).
- [29] F. Bissey, A.W. Thomas and I.R. Afnan, Phys. Rev. C **64**, 024004 (2001).
- [30] M. Anselmino *et al.*, Phys. Rep. **261**, 1–124 (1995).
- [31] D. Parno, Ph.D. Thesis, Carnegie Mellon University (2011).
- [32] I. Kominis, Ph.D. Thesis, Princeton University (2001).
- [33] J. Singh, *A Note About Beam Depolarization*, Univeristy of Virginia (2008).
- [34] D. Parno *et al.*, E06-014 Analysis Status Report 2010, https://hallaweb.jlab.org/wiki/images/b/b3/D2n_Annual_Report_2010.pdf
- [35] M. Posik *et al.*, E06-014 Analysis Status Report 2011, https://hallaweb.jlab.org/wiki/images/8/8c/D2n_HallAReport_2011.v5.pdf

- [36] D. Flay *et al.*, E06-014 Analysis Status Report 2012, <https://hallaweb.jlab.org/wiki/images/7/7a/E06014-2012.pdf>
- [37] L.W. Mo and Y.S. Tsai, *Rev. Mod. Phys.* **40**, 205 (1969).
- [38] R. Altulmus and J. Wise, *rosetail.f*, fortran analysis code.
- [39] Amroun *et al.*, *Nucl. Phys. A* **579**, 596 (1994).
- [40] J. W. Lightbody and J. S. O'Connell, *Comp. in Phys.*, 57 (1988).
- [41] S. Stein *et al.*, *Phys. Rev. D* **12**, 1884 (1975).
- [42] Roy Whitney, *radcor.f*, fortran analysis code.
- [43] P.E. Bosted and V. Mamyan, *Empirical Fit to electron-nucleus scattering* (2012), arXiv:1203.2262v2 [nucl-th].
- [44] D. de Florian, R. Sassot, M. Stratmann and W. Vogelsang, *Phys. Rev. Lett.* **101**, 072001 (2008).
- [45] P.E. Bosted, *Phys. Rev. C* **51**, 409 (1995).
- [46] J. E. Amaro, M. B. Barbaro, J. A. Caballero, T. W. Donnelly, A. Molinari and I. Sick, *Phys. Rev. C* **71**, 015501 (2005).
- [47] P.L. Anthony *et al.*, *Phys. Rev. D* **54**, 6620 (1996).
- [48] P. Solvignon *et al.*, *Phys. Rev. Lett.* **101**, 182502 (2008).
- [49] F. Bissey *et al.*, *Phys. Rev. C* **65**, 064317 (2002).
- [50] S.A. Kulagin and W. Melnitchouk, *Phys. Rev. C* **78**, 065203 (2008).
- [51] H. Weigel, L. Gamberg and H. Reinhart, *Phys. Rev. D* **55**, 6910 (1997).
- [52] C.R.V. Bourely, J. Soffer and F. Buccella, *Eur. Phys. J. C* **41**, 327 (2005) [arXiv:hep-ph/0502180].
- [53] M. Stratmann, *Z. Phys. C* **60**, 763 (1993).
- [54] J. F. Owens, A. Accardi and W. Melnitchouk, *Phys. Rev. D* **87**, 094012 (2013).
- [55] J. Pumplin, D. R. Stump and J. Huston *et al.*, *J. High Energy Phys.* **7**, 012 (2002).

3.6 E07-007 and E08-025: Deeply Virtual Compton Scattering

P. Bertin, A. Camsonne, C. Hyde, M. Mazouz, C. Muñoz Camacho and J. Roche, spokespersons,
and
the Hall A Collaboration.
contributed by C. Muñoz Camacho.

3.6.1 Introduction

Deeply Virtual Compton Scattering (DVCS) refers to the electroproduction of photons in the Deep Inelastic Scattering (DIS) kinematics: $ep \rightarrow ep\gamma$. In the Bjorken regime, this reaction is sensitive to the Generalized Parton Distributions (GPDs) of the nucleon. In the photon electroproduction, the DVCS amplitude interferes with the so-called Bethe-Heitler (BH) process, where the photon is radiated by the electron, instead of the proton. Previous measurements of DVCS cross sections, both on the proton [1] and the deuteron [2], showed a significant contribution of the pure DVCS² term, comparable to the BH-DVCS interference.

The goal of DVCS experiments E07-007 and E08-025 is to perform a Rosenbluth-like separation of the pure DVCS² and the BH-DVCS interference terms from the photon electroproduction cross section. The cross section was measured at 3 different values of Q^2 with an LH2 target (E07-007) and at one Q^2 with an LD2 target (E08-025), all at constant $x_B = 0.36$. Each measurement was performed at two different incident beam energies E_b .

A secondary goal of the experiments is to perform an L/T separation of the π^0 electroproduction cross section, from both a proton and deuteron target. The only measurements of π^0 electroproduction cross sections in Jefferson Lab kinematics are still unseparated [3, 4]. For the proton target, σ_L and σ_T will be measured as a function of Q^2 within a limited range: 1.5 to 2.0 GeV².

3.6.2 Status of the analysis

Calibrations of all subsystems are completed and final physics analysis has started for all different channels and kinematic settings.

Stability of the data and global normalization has been checked by computing the DIS cross section in a run-by-run basis. Figure 31 shows, for one of the kinematic settings ($Q^2 = 1.5$ GeV² and $E_b = 3.356$ GeV), the DIS cross section measured as a function of the run number. The stability of the results is below 2%, once a few runs with identified problems are removed.

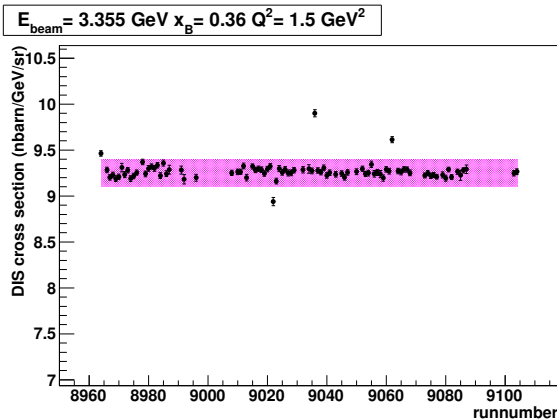


Figure 31: DIS cross section as a function of the run number for the kinematic setting with $Q^2 = 1.5$ GeV² and $E_b = 3.356$ GeV. The magenta band shows the stability of the results to 1.6% once 4 particular runs with identified problems are removed from the analysis.

Table 2 shows a summary of the DIS results for all our kinematics. Results are compared to the ones obtained using the parametrization of the structure functions [5]. Also, the stability of our results is presented in the last column.

Table 2: DIS cross section measured for each kinematic setting. The second column shows the result using the parametrization of the structure functions [5] and the third column shows our measurement. The relative difference between these two values is also presented. Finally, the last column represents the stability of our results as a function of time (run number).

Kinematic setting	$\frac{d\sigma^{TMC}}{d\Omega dE}$ (nb/GeV/sr)	$\frac{d\sigma_{exp}^{TMC}}{d\Omega dE}$ (nb/GeV/sr)	Relative difference (%)	Stability (%)
$Q^2 = 1.50 \text{ GeV}^2, E_b = 3.356 \text{ GeV}$	9	9.26	+2.8	1.6
$Q^2 = 1.50 \text{ GeV}^2, E_b = 5.552 \text{ GeV}$	55.2	53.3	-3.4	1.3
$Q^2 = 1.75 \text{ GeV}^2, E_b = 4.454 \text{ GeV}$	13.14	13.14	0	2
$Q^2 = 1.75 \text{ GeV}^2, E_b = 5.552 \text{ GeV}$	28.93	27.9	-3.4	1.3
$Q^2 = 2.00 \text{ GeV}^2, E_b = 4.454 \text{ GeV}$	6.6	6.9	+4.5	4
$Q^2 = 2.00 \text{ GeV}^2, E_b = 5.552 \text{ GeV}$	15.93	15.26	-4	2.2

All photon data have been processed and number of counts for DVCS off the proton and the deuteron are available for all of the kinematic settings. Figure 32 shows the $ep \rightarrow e\gamma X$ missing mass squared M_X^2 off the proton for the kinematic setting $Q^2 = 1.5 \text{ GeV}^2$ and $E_b = 3.356 \text{ GeV}$. Neutral pion decays that yield only one photon in the DVCS calorimeter are subtracted from the raw data using the sample of events where the 2 photons of the decay are detected. This contribution is shown in blue in Figure 32.

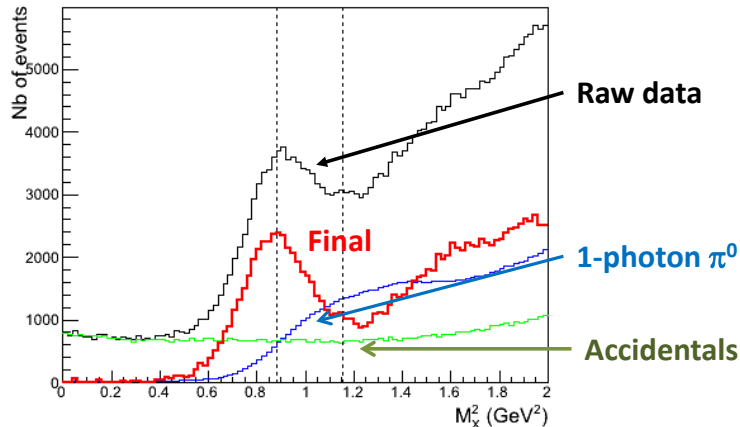


Figure 32: DVCS $ep \rightarrow e\gamma X$ missing mass squared M_X^2 off the proton, $Q^2 = 1.5 \text{ GeV}^2$ and $E_b = 3.356 \text{ GeV}$. The black histogram shows the raw data and the red is the final sample, once accidentals (green) and the contamination from 1-photon π^0 s (blue) are subtracted.

The DVCS cross section is extracted using a Monte Carlo simulation of the experimental setup and integrating the known kinematic factors of the different cross-section terms over each experimental bin. Thus, the average value of the Compton Form Factors (GPD integrals) are accurately computed in each bin, regardless of the rapid variation of the cross section within the bins. Figure 33 shows, for one particular bin in the momentum transfer t of the kinematic setting $Q^2 = 2.0 \text{ GeV}^2$ and $E_b = 5.552 \text{ GeV}$, the experimental number of counts as a function of the angle φ_γ between the leptonic and hadronic planes, together with the estimate obtained from the Monte Carlo simulation.

DVCS events from the LD2 target are also in advanced stage of analysis. Measurements of DVCS off the neutron relies on the measurements with an LD2 and the subtraction of the proton contribution obtained using an LH2 target. Figure 34 shows the $ep \rightarrow e\gamma X$ missing mass squared for the same kinematics with both an LH2 (left) and LD2 (right) target. Accidental and π^0 contamination are subtracted from the raw data (black) in order to obtain the final DVCS sample (red). The vertical line at $M_X^2 = (M_n + m_\pi)^2 = 1.15 \text{ GeV}^2$

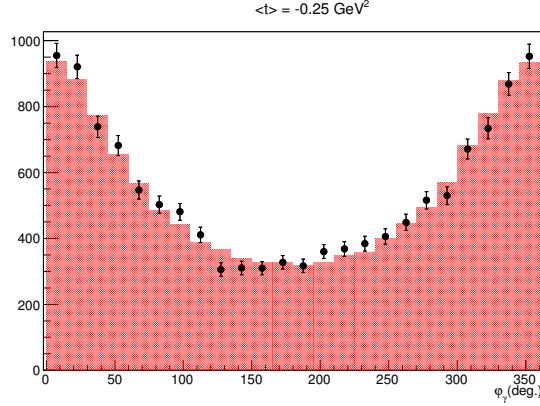


Figure 33: Final number of DVCS counts for $Q^2 = 2.0 \text{ GeV}^2$, $E_b = 5.552 \text{ GeV}$ and $t = -0.25 \text{ GeV}^2$ (black points) as a function of the angle φ_γ between the leptonic and hadronic planes. The red histogram shows the estimate obtained from a Monte Carlo simulation of the experimental setup.

shows the cut applied to ensure exclusivity.

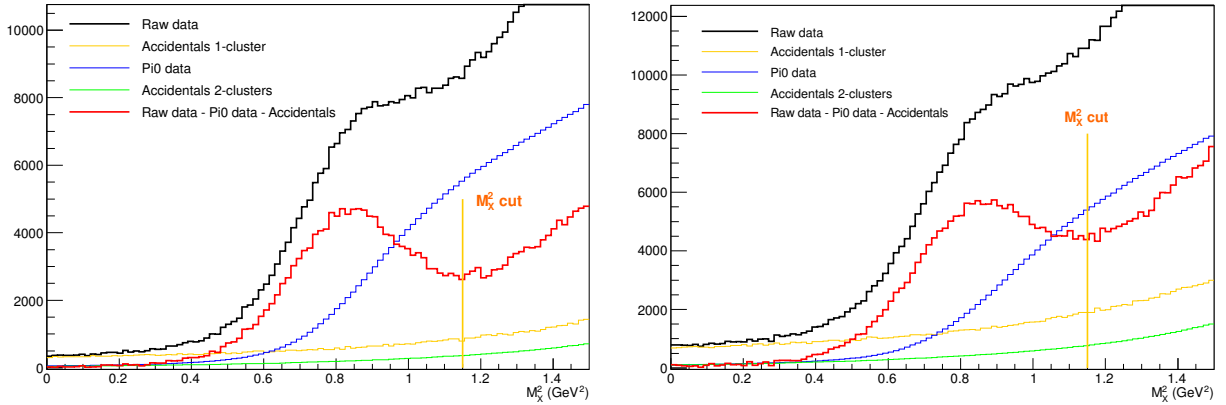


Figure 34: DVCS $ep \rightarrow e\gamma X$ missing mass squared M_X^2 , $Q^2 = 1.75 \text{ GeV}^2$ and $E_b = 5.552 \text{ GeV}$. The black histogram shows the raw data and the red is the final sample, once accidentals (green and yellow) and the contamination from 1-photon π^0 s (blue) are subtracted. The left plot shows data off a LH2 target and the right plot corresponds to an LD2 target.

References

- [1] C. Muñoz Camacho *et al.*, Phys. Rev. Lett. **97**, 262002 (2006).
- [2] M. Mazouz *et al.*, Phys. Rev. Lett. **99**, 242501 (2007).
- [3] E. Fuchey *et al.*, Phys. Rev. **C83**, 025201 (2011).
- [4] I. Bedlinskiy *et al.*, Phys. Rev. Lett. **109**, 112001 (2012).
- [5] I. Schienbein *et al.*, J. Phys. **G35**, 053101 (2008).

3.7 E08-005: Target Single-Spin Asymmetry A_y^0 in the Quasi-Elastic ${}^3\text{He}^\uparrow(e, e'n)$ Reaction

T. Averett, D. Higinbotham, V. Sulkosky, (Spokespersons)
and
the Hall A Collaboration.
contributed by E. Long (University of New Hampshire).

3.7.1 Progress of ${}^3\text{He}(e, e'n)$ A_y^0

Progress has been made on the ${}^3\text{He}^\uparrow(\vec{e}, e'n)$ target single-spin asymmetry, A_y^0 , for experiment E08-005, where the target was polarized in the vertical direction, transverse to the beam. In plane wave impulse approximation (PWIA), this asymmetry is exactly zero. Any non-zero measurement indicates higher-order effects, such as final state interactions (FSI) and meson exchange currents (MEC).

Data from the RHRS were used to isolate the quasi-elastically scattered electrons using standard kinematic cuts. Neutrons were identified using the Hall A Neutron Detector. New analysis was conducted this past year to examine run-by-run fluctuations of A_y^0 , as illustrated in Fig. 35 for $Q^2 = 0.46$ (GeV/c)².

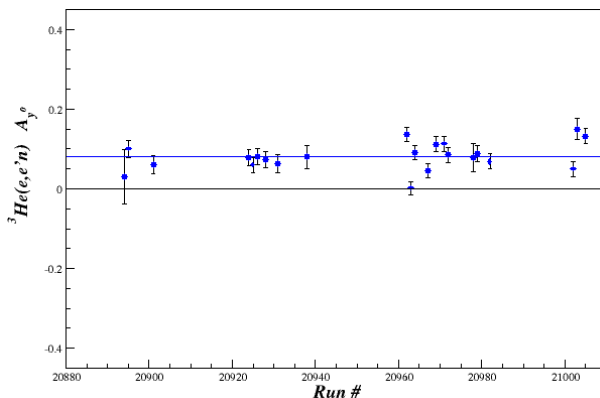


Figure 35: A_y^0 calculated on a run-by-run basis at $Q^2 = 0.46$ (GeV/c)².

The analysis was compared directly to Y. Zhang's ${}^3\text{He}^\uparrow(e, e')$ target single-spin asymmetry by removing the neutron cuts. Through this comparison, it was found that there were minor corrections to the calculation of the charge and the live-time that were included into the A_y^0 analysis. This discrepancy, and fix, are shown in Fig. 36 for $Q^2 = 0.46$ (GeV/c)².

However, these corrections did not account for the fluctuations seen when the neutron cuts were applied, shown in Fig. 37. The fluctuations were included as a systematic uncertainty of the neutron cuts using the χ^2 scaling method described in the Review of Particle Physics. In this method, a scaling factor S is defined by

$$S = [\chi^2/dof]^{1/2}. \quad (19)$$

This factor is then applied to the total uncertainty. The contribution due to only these fluctuations is then separated into a systematic contribution and included in the total uncertainty analysis.

A paper summarizing the final results has been prepared and is circulating the collaboration for comments. We expect to submit the final results to Physics Review Letters in early 2014.

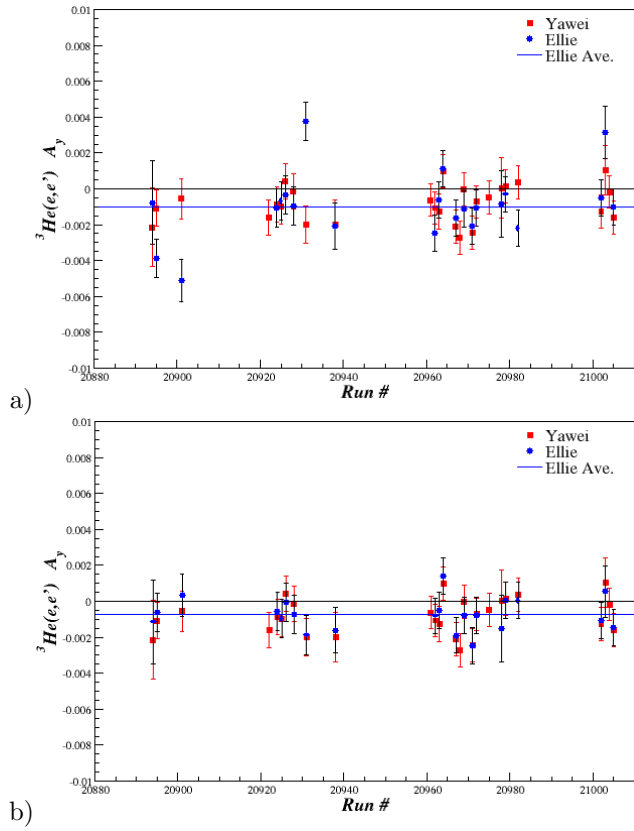


Figure 36: The ${}^3\text{He}^\uparrow(e, e')$ target single-spin asymmetry was compared to Y. Zhang’s analysis of the same dataset. Calculations were done using a) the original analysis script and b) the corrected analysis script, which accounted for minor corrections to the charge and live-time calculations.

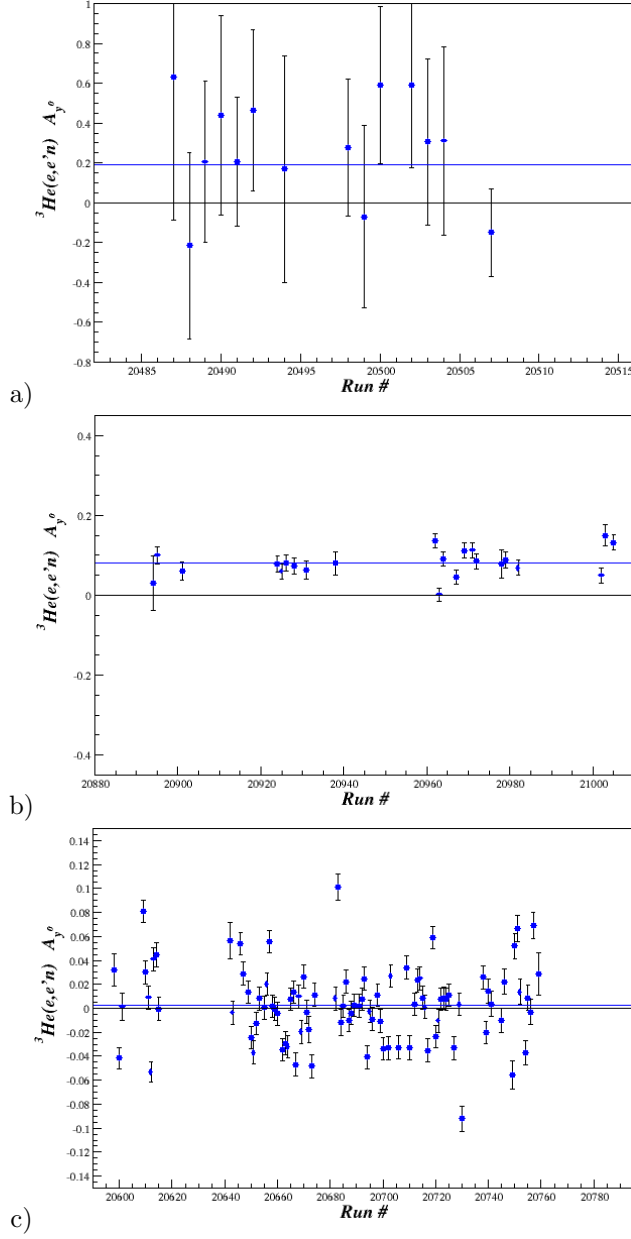


Figure 37: Run-by-run analysis of A_y^0 for Q^2 of a) $0.13 \text{ (GeV}/c)^2$, b) $0.46 \text{ (GeV}/c)^2$, and c) $0.95 \text{ (GeV}/c)^2$

3.8 E08-007-II: G_E^p at Low Q^2

M. Friedman, for the E08-007 collaboration

3.8.1 Motivation

The measurement of the proton form factor ratio at low Q^2 is important for several reasons. First, the form factors are fundamental properties of the nucleon that should be measured well to test our understanding of the nucleon. Second, although theory generally indicates that the form factors vary smoothly with Q^2 , there are an unsatisfyingly large number of theoretical calculations, fits, and data points that suggests this might not be the case, and that there might be narrow structures in the form factors. Experiment E08-007-II is good enough to either confirm or refute existing suggestions of few percent structures in the form factors, or in the form factor ratio. Third, it has become apparent that the existing uncertainties in the form factors are among the leading contributions to uncertainties in determining other physics quantities, such as the nucleon Zemach radius, the strange form factors determined in parity violation, and the generalized parton distributions determined in deeply virtual Compton scattering. The improvement possible with this measurements is substantial. The proton electric and magnetic "radii" are also directly related to the form factor slope at $Q^2 = 0$:

$$\langle r_{E/M}^2 \rangle = -\frac{6}{G_{E/M}(0)} \left(\frac{dG_{E/M}(Q^2)}{dQ^2} \right)_{Q^2=0}. \quad (20)$$

Recent results from muonic-hydrogen lamb shift measurements [1] suggest a significantly smaller charge radius for the proton than the established values, and precise measurement of the form factors at very low Q^2 may help to resolve this discrepancy.

3.8.2 The Experiment

E08-007-II was run in parallel with E08-027. Details about the experiment can be found in the experiment section of E08-027. All E08-007-II runs were taken with a magnetic field of 5T. The kinematics are listed in Table 3.

3.8.3 Experimental Progress

Details about optics, helicity and other calibrations are listed in the experimental progress section of E08-027. The target polarization analysis is completed, with relative uncertainties of $\sim 2\%$ - 3% . These uncertainties are still under investigation.

A preliminary extraction of the raw data has been completed, with the available calibrations, for the entire data set. Analysis of the data with the available optics is complete, and the physical asymmetries are listed in Table 3.

The proton data in this experiment is diluted by elastic and quasi-elastic scattering off nitrogen (in the ammonia) and helium (cooling liquid). While elastic cross section data for ^4He is available, we have only a single experiment for ^{14}N elastic cross section in the relevant Q^2 range. Neither ^4He nor ^{14}N has experimental quasi-elastic cross section data. In order to estimate our dilution we are working in parallel on three techniques: A. Using ^{12}C dilution runs and scaling the magnitude by the elastic peaks. B. Writing MC simulations, based on phenomenological cross section models, and comparing to experimental data. C. Analyzing unpublished ^{14}N quasi-elastic cross section data.

At present, the dilution analysis is based on carbon data with results shown in Table 3. An example extraction is shown in Fig. 38. MC simulations are not yet sufficiently good for extracting experimental data. (See Fig. 39 for example). When optics calibrations are done, we will be able to improve the transport calculations from the target to the focal plane and hopefully improve our results.

After background analysis is done, we are able to extract physical asymmetries for each kinematic setup and binning. Asymmetries are calculated for each run separately, and the mean value and its uncertainty are extracted by fitting to a constant number. Fig. 40 shows an example of such extraction. Table 3 summarizes our preliminary results. These should be taken with caution, since calibrations and dilution analysis are not yet final.

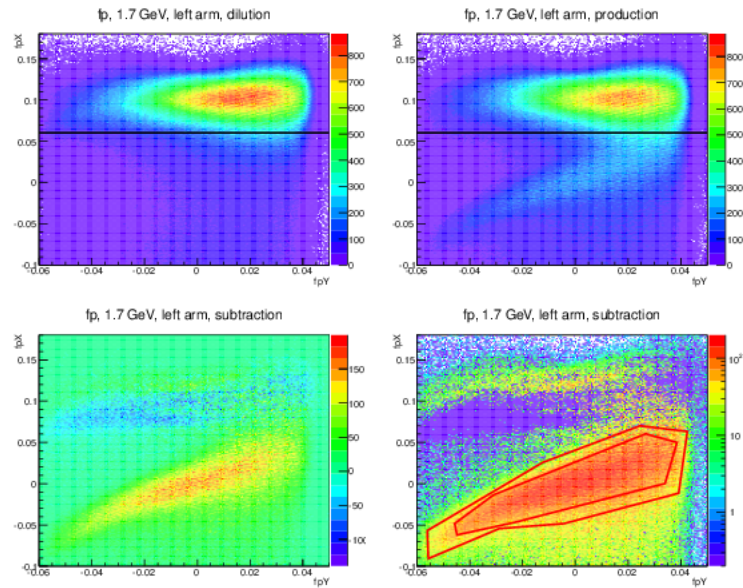


Figure 38: Background subtraction procedure, 1.7 GeV left arm data. Top-left is the dilution run, and top-right is the production run. The black line represents the fpX limit used for normalization. The separation between hydrogen elastic peak and other events is not clear enough. The bottom-left is the subtraction after normalizing, and the bottom-right is the same in log scale. Two different cuts are show, and used for consistency purposes

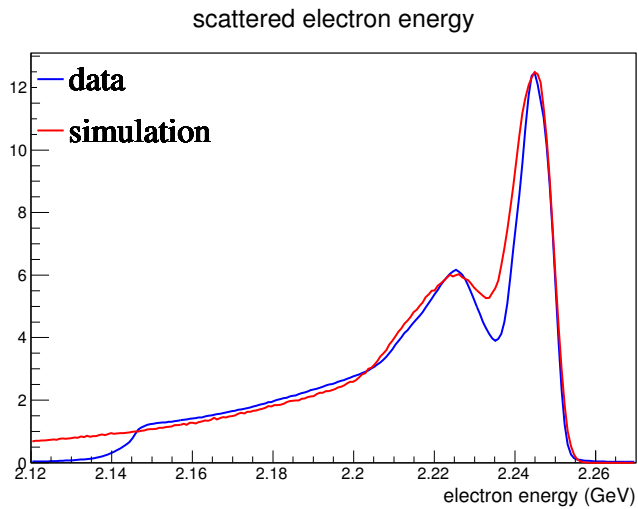


Figure 39: Monte-Carlo simulation of production data at 2.2 GeV (left arm), compared to experimental data. Agreement is not yet good enough for dilution analysis.

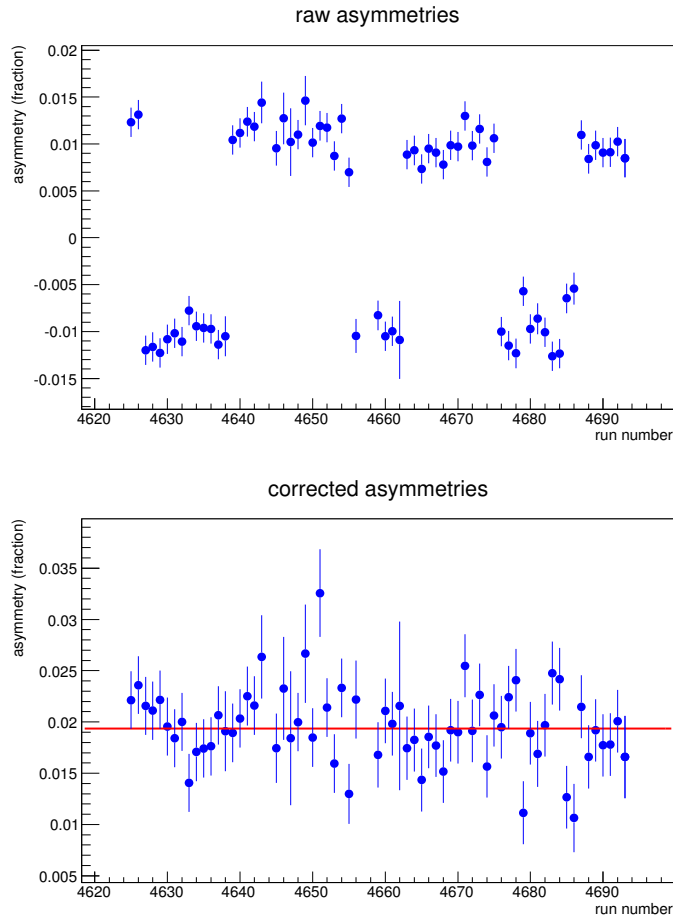


Figure 40: An example for physical asymmetry extraction. This data is for the left arm, 1.7 GeV runs. The uncertainty is extracted by the fit, and the χ^2 values are listed in Table 3.

arm	bin		cut 1			cut 2					
	E_e (GeV)	Q^2 range (GeV ²)	Q^2 value (GeV ²)	dilution	A (%)	$\Delta A/A$ (%)	χ^2/ndf	dilution	A (%)	$\Delta A/A$ (%)	χ^2/ndf
left	2.2	0.045-0.080	0.057±0.008	0.74	3.03±0.046	1.52	1.57	0.68	2.96±0.042	1.42	1.53
right	2.2	0.056-0.082	0.065±0.005	0.67	3.39±0.059	1.74	0.85	0.59	3.41±0.058	1.70	1.21
left	2.2	0.028-0.050	0.037±0.006	0.75	1.56±0.021	1.35	1.20	0.70	1.48±0.021	1.42	1.34
right	2.2	0.038-0.064	0.047±0.006	0.71	1.93±0.029	1.50	1.60	0.66	1.74±0.029	1.67	1.39
left	1.7	0.020-0.045	0.028±0.006	0.71	1.93±0.038	1.97	1.25	0.66	1.95±0.035	1.79	0.96
right	1.7	0.031-0.050	0.037±0.004	0.78	2.17±0.071	3.27	0.79	0.73	2.20±0.055	2.50	0.87
left	1.7	0.017-0.027	0.020±0.003	0.54	1.24±0.071	5.87	0.90	0.48	1.18±0.066	5.59	0.82
right	1.7	0.023-0.033	0.027±0.003	0.67	1.68±0.056	3.33	1.23	0.64	1.53±0.047	3.07	1.38
left	1.1	0.009-0.020	0.012±0.0027	0.26	1.78±0.060	3.37	0.79	0.23	1.72±0.052	3.02	0.80
right	1.1	0.010-0.022	0.014±0.0026	0.18	2.33±0.120	5.15	0.74	0.15	2.78±0.097	3.49	0.70

Table 3: Preliminary asymmetries for the GEp experiment. All numbers should be taken with caution. See text for details.

References

- [1] R. Pohl *et al.*, Nature 466, 213 (2010).

3.9 E08-009: ${}^4\text{He}(e, e'p){}^3\text{H}$ at $x_b = 1.24$

A. Saha, D. Higinbotham, F. Benmokhtar, S. Gilad, and K. Aniol, spokespersons
and
Students: S. Iqbal(CSULA) and N. See(CSULA)
and
the Hall A Collaboration.
contributed by K. Aniol.

3.9.1 Experimental Conditions

The data were taken in collaboration with the SRC(E07-006) measurement during April 13 and April 14, 2011 for 16 hours of running. Our measurements provide the low missing momenta data taken at the 0.153 GeV/c and 0.353 GeV/c kinematic settings, which complement the high missing momenta data of the SRC experiment. A 20 cm long cryogenic ${}^4\text{He}$ target at 20K and 10 atmosphere provided a thickness of about $8 \times 10^{22}/\text{cm}^2$. The electron beam energy was 4.454 GeV. This is the first measurement of ${}^4\text{He}(e, e'p)X$ at this value of $x_b = 1.24$. The M.S. thesis by Sophia Iqbal [1] gives greater detail on the data's analysis.

3.9.2 Motivation

A theoretical description of ${}^4\text{He}(e, e'p)X$ is critical for understanding nuclear structure. In particular, one must be able to include many body forces in the theory. The reaction we measured actually includes multiple exit channels, that is, $X = {}^3\text{H}, n + {}^2\text{H}$ and $n+n+p$ nuclear and nucleonic channels. At the beam energy used here meson production also contributes to X . Our first goal is to compare the data for ${}^4\text{He}(e, e'p){}^3\text{H}$ to theoretical calculations provided by the Madrid group [2]. The missing energy spectra also reveal a broad peak attributed [3] to the absorption of the virtual photon on a pair of nucleons.

3.9.3 E_{miss} Spectra

The E_{miss} spectrum calculated from the Hall A analyzer variable SKxceb.emiss shows a strong dependence on the ReactPt_L.y value as seen in figure 41. We made a linear fit in the root analysis script correcting for the slope using:

```
TString ec_emiss("SKxceb.emiss - 1.7255*(ReactPt_L.y - 0.0006)");
```

The two dimensional plot after applying this correction is shown in figure 42.

The E_{miss} spectra with the y_{tgt} corrections applied are shown in figures 43, 44, 45.

3.9.4 Simulations

During the root replay of the GEANT simulations the electron momenta and proton momenta were subjected to Gaussian broadening to match the FWHM of the strong triton peak seen in the $0.153\text{GeV}/c$ data.

```
eexs = eexs*gRandom.Gaus(mean,sig1);  
eeys=eeys*gRandom.Gaus(mean,sig1);  
eezs=eezs*gRandom.Gaus(mean,sig1);  
  
ppxs=ppxs*gRandom.Gaus(mean,sig1);  
ppys=ppys*gRandom.Gaus(mean,sig1);  
ppzs=ppzs*gRandom.Gaus(mean,sig1);
```

A comparison between the simulated E_{miss} triton spectrum using $\text{sig1} = 1. \times 10^{-4}$ and $\text{sig1} = 6.53 \times 10^{-4}$ is shown in figure 46. The data and the simulated triton peaks are shown in figures 47, 48.

The wide momentum acceptances of the HRSs' allows for a broad missing momentum acceptance. In the simulation each point within the spectrometers' apertures has an equal probability of being a target for a vertex electron or proton. The 3 body kinematical and geometrical limitations are correctly determined by

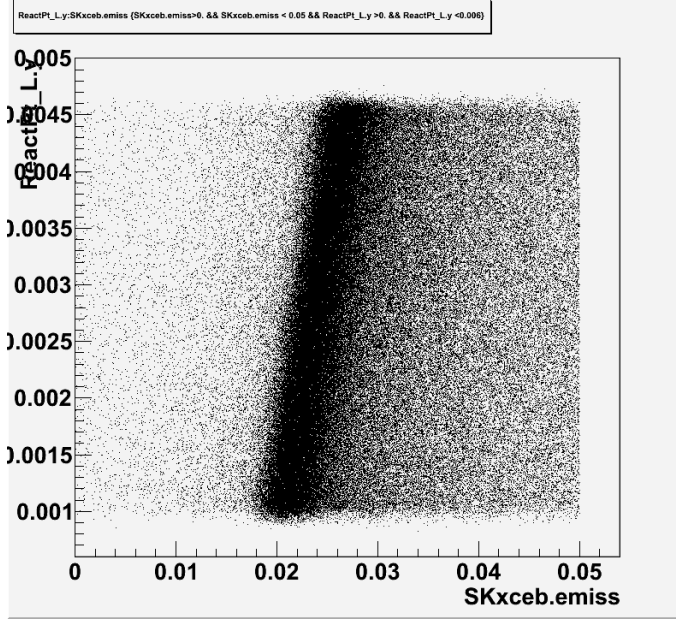


Figure 41: E_{miss} defined by SKxceb.emiss vs y_{tgt} for the $0.153\text{GeV}/c$ kinematic setting.

GEANT. We thus define the missing momentum acceptance factor, $f(p_m)$, for a bin of missing momentum centered around p_m as

$$f(p_m) = \frac{n(p_m)}{\sum n(p_m)}. \quad (21)$$

Where $n(p_m)$ is the number of triton events in the missing momentum bin centered on p_m and $\sum n(p_m)$ is the total number of triton events over all missing momenta for the particular kinematic setting. This factor, $f(p_m)$ is used in the cross section determinations for each missing momentum bin. An example of the simulation prediction for the missing momenta spectra is shown in figure 49.

The simulation also allows us to determine the fraction of triton events which fall outside of the window we place around the triton peak in the data. This loss of tritons is due to radiative processes and multiple scattering. A more extended discussion of the simulation is in reference [4].

3.9.5 SRC target behavior

The SRC target presented challenges for cross section measurements. We are grateful to Patricia Solvignon and Zhihong Ye for sharing their results about their `ztgt` analysis of this target and especially to Silviu Covrig for providing CFD calculations [6].

The SRC target container is an aluminum can of length 20cm. Cryogenic ${}^4\text{He}$ enters and exits at the upstream end of the target. There is no outlet for the fluid at the downstream end of the can. A diagram of the target from a CFD calculation for a $95\mu\text{A}$ electron beam is shown in figure 50.

The issue with the SRC target, which inspired extensive study, was the non monotonic decrease in event rate as a function of distance between the beam in and beam out points along the z axis seen in figure 51. The first concern was that the beam was hitting some structures besides the ${}^4\text{He}$ target. However, there were no other indications of a misdirected beam or beam halo hitting anything but the cryogenic target. The shape of the `ztgtL` distribution was very stable. The beam currents used for the short runs of E08009, $60\mu\text{A}$, $47\mu\text{A}$, and the long SRC runs at $4\mu\text{A}$ show no significant difference in `ztgtL` shape except for the decrease in count rate.

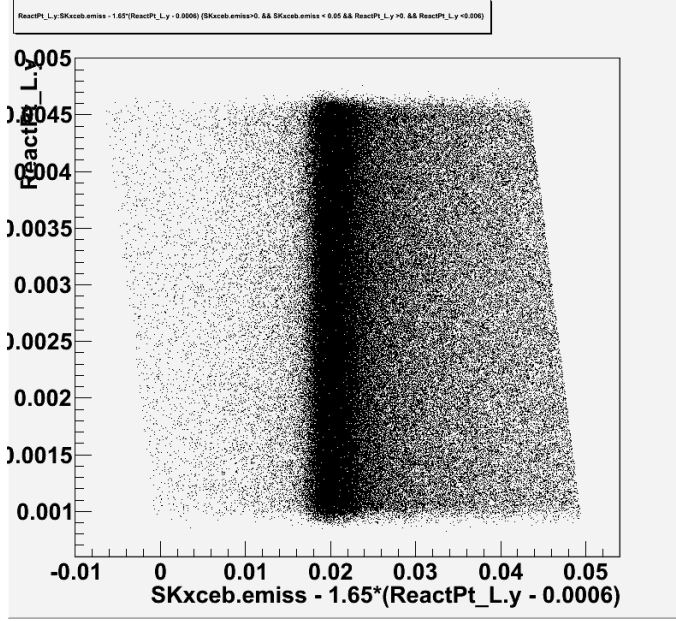


Figure 42: E_{miss} corrected for the y_{tgt} slope for the $0.153\text{GeV}/c$ kinematic setting.

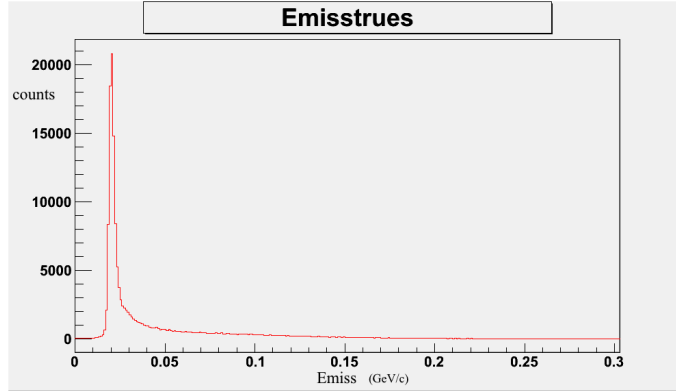


Figure 43: E_{miss} for the $0.153\text{GeV}/c$ kinematic setting.

Although the CFD calculations do not match exactly with the ztgtL distributions seen in the experiment, they do show that the ztgtL distribution will not be a smooth function along the beam axis. Perhaps with sufficient tuning of the parameters or models used in the CFD calculations a match can be made with experiment. The SRC target is a challenge computationally. We were able to extract the target density, $\rho(z, I)$ from a combination of the measure ztgtL distributions and the $4\mu A$ predictions from CFD. More details of the SRC target analysis are found in references [1] and [5].

3.9.6 Cross Section Results and Theory

Our data and theory for the cross section for ${}^4\text{He}(e, e'p){}^3\text{H}$, $\frac{d\sigma}{dE d\Omega_e d\Omega_p}$, is shown in figure 52. A comparison between theory and data for proton angles between 35 degrees and 47 degrees yields

$$\frac{\Sigma\sigma_{data}(\theta_p)\sin(\theta_p)d\theta_p}{\Sigma\sigma_{theory}(\theta_p)\sin(\theta_p)d\theta_p} \leq 0.68. \quad (22)$$

Tables containing the cross sections for data and theory are found in the thesis [1].

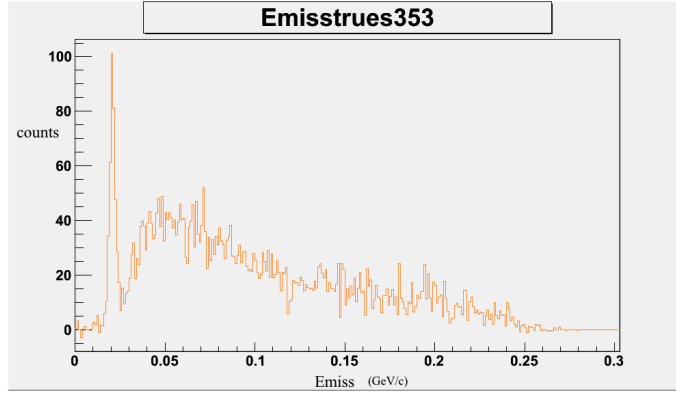


Figure 44: E_{miss} for the $0.353\text{GeV}/c$ kinematic setting.

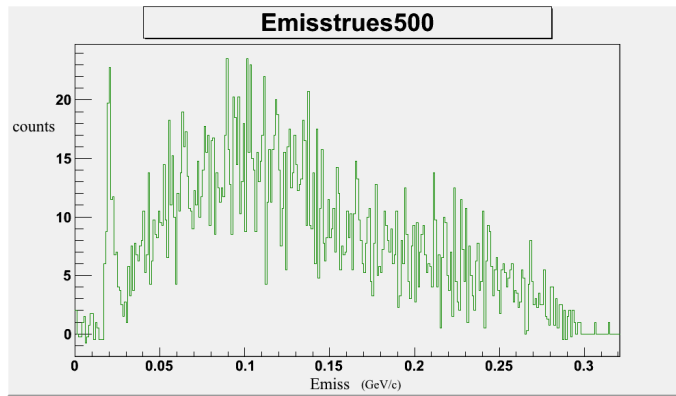


Figure 45: E_{miss} for the $0.500\text{GeV}/c$ kinematic setting.

References

- [1] <https://userweb.jlab.org/~aniol/e08009/sana-thesis-dec20-2013.pdf>
- [2] J.R. Vignote, private communication
- [3] F. Benmokhtar *et al.* Phys. Rev. Lett. **94** 082305
- [4] <https://userweb.jlab.org/~aniol/e08009/simulations.pdf>
- [5] https://userweb.jlab.org/~aniol/e08009/iscan_corrections/SRCtgt.pdf
- [6] Computational Fluid Dynamics calculations, private communication, Silviu Covrig

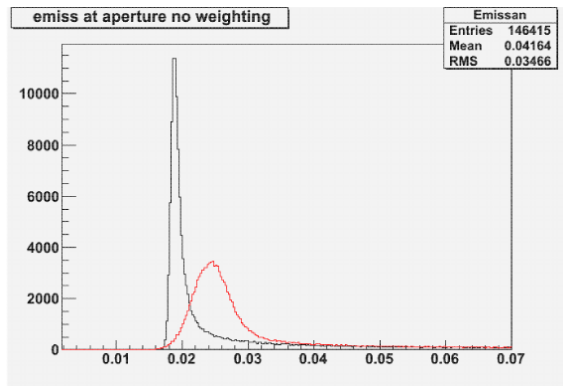


Figure 46: GEANT simulations, Gaussian broadened, of the triton missing energy spectrum. The black curve is for $\sigma = 1. \times 10^{-4}$ and the red curve is offset to match the data with $\sigma = 6.53 \times 10^{-4}$.

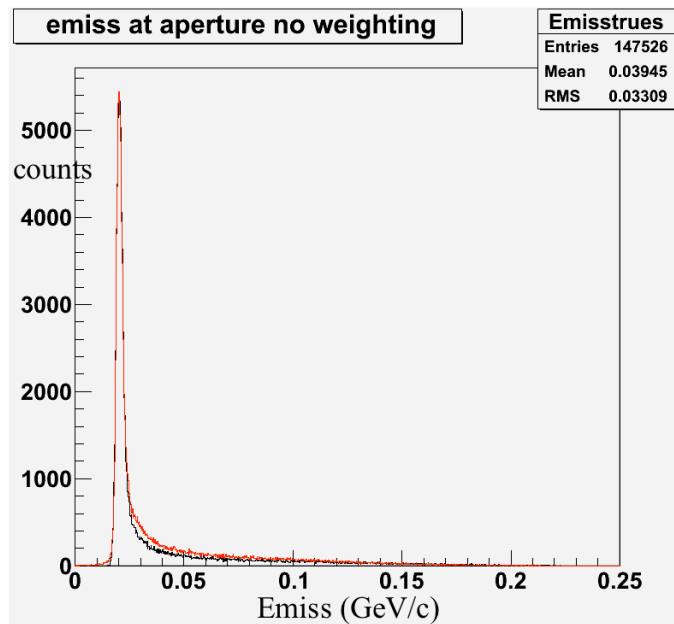


Figure 47: GEANT simulation(black curve) and data(red curve) for the $0.153\text{GeV}/c$ kinematic setting.

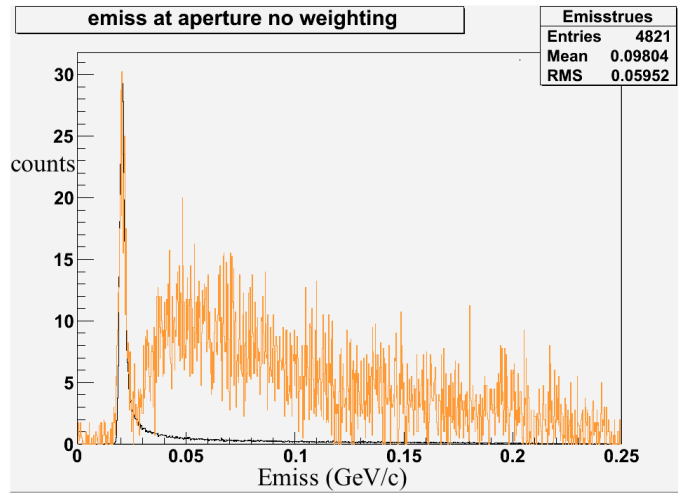


Figure 48: GEANT simulation(black curve) and data(orange curve) for the $0.353\text{GeV}/c$ kinematic setting.

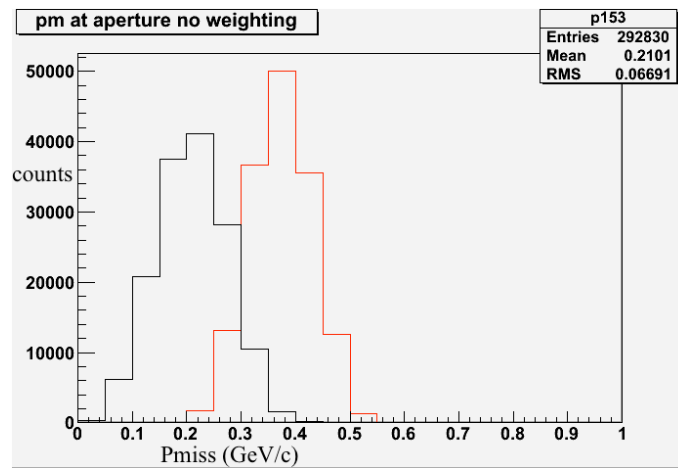


Figure 49: GEANT missing momentum spectra for $0.153\text{GeV}/c$ (black) and $0.353\text{GeV}/c$ (red) as determined at the spectrometer apertures.

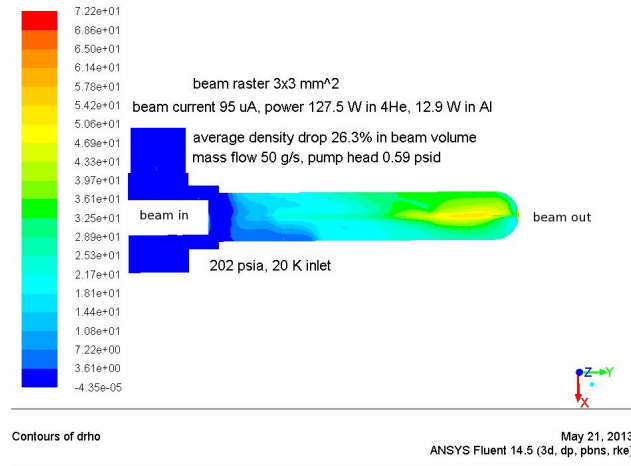


Figure 50: Computational Fluid Dynamic calculation [6] for the SRC target. $drho$ is the loss in percent of density from the input fluid.

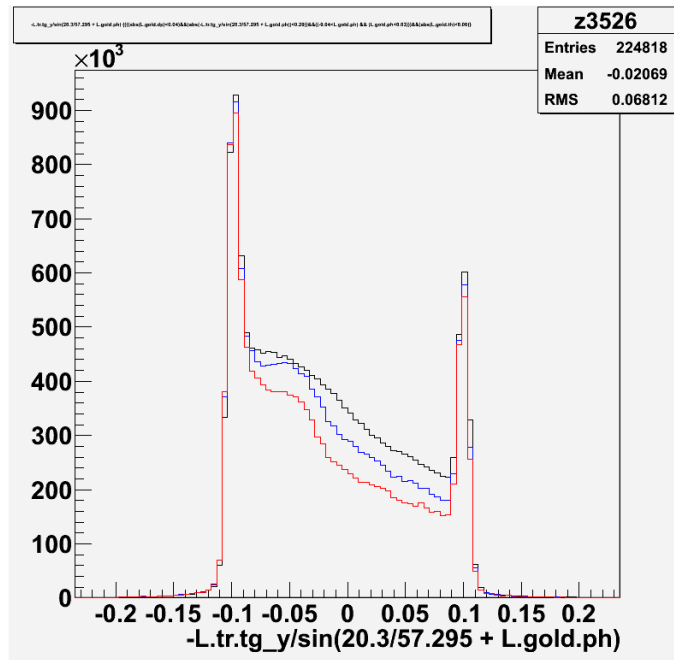


Figure 51: Normalized counts per Coulomb (vertical axis) along the beam's path for 4 different beam currents. $4\mu A$ (black), $47\mu A$ (blue), $60\mu A$ (red). The horizontal axis is along z in meters. The aluminum end caps are seen as sharp spikes at $\pm 0.1m$.

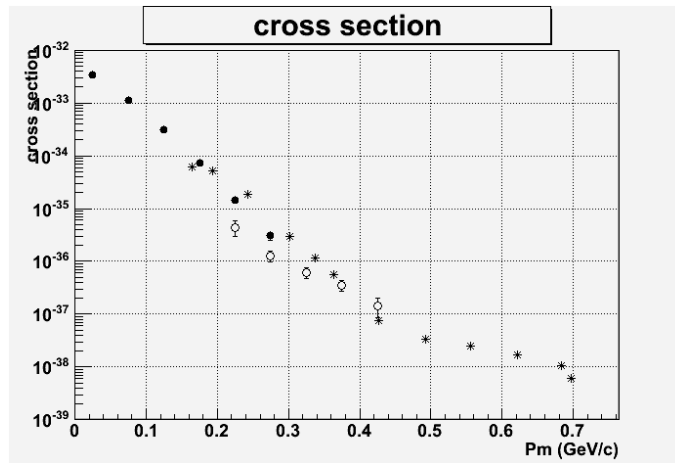


Figure 52: Cross sections for $0.153\text{GeV}/c$ (closed dots), $0.353\text{GeV}/c$ (open dots) and Madrid Theory(asterisks) [2]. The units are $\frac{\text{cm}^2}{\text{MeV} * s R^2}$. The first two theory values are underestimates because the theory values we have are only valid above $0.150\text{GeV}/c$, but the simulations and data continue below $0.150\text{GeV}/c$.

3.10 E08-010: Measurement of the Coulomb quadrupole amplitude at the $\gamma^*p \rightarrow \Delta(1232)$ in the low momentum transfer region

S. Gilad, D. W. Higinbotham, A. Sarty and N. F. Sparveris, spokespersons,

Graduate students: D. Anez (St. Mary's), A. Blomberg (Temple)

and the Hall A Collaboration.

contributed by N.F. Sparveris

3.10.1 Introduction

Hadrons are composite systems with complex quark-gluon and meson cloud dynamics that give rise to non-spherical components in their wave-function which in a classical limit and at large wavelengths will correspond to a "deformation". In recent years an extensive experimental and theoretical effort has been focused on identifying and understanding the origin of possible non-spherical amplitudes in the nucleon wave-function [1, 2, 3, 4, 5, 6, 7, 8, 9, 10, 11, 12, 13, 14, 15, 16, 17, 18, 19, 20, 21, 22, 23, 24, 25, 26, 27, 28, 29]. The spectroscopic quadrupole moment provides the most reliable and interpretable measurement of these components; for the proton, the only stable hadron, it vanishes identically because of its spin 1/2 nature. As a result, the presence of resonant quadrupole amplitudes in the $N \rightarrow \Delta$ transition has emerged as the definitive experimental signature of non spherical amplitudes. Spin-parity selection rules in the $\gamma^*N \rightarrow \Delta$ transition allow only magnetic dipole (M1) and electric quadrupole (E2) or Coulomb quadrupole (C2) photon absorption multipoles (or the corresponding pion production multipoles $M_{1+}^{3/2}, E_{1+}^{3/2}$ and $S_{1+}^{3/2} (L_{1+}^{3/2})$ respectively) to contribute. The ratios $\text{CMR} = \text{Re}(S_{1+}^{3/2}/M_{1+}^{3/2})$ and $\text{EMR} = \text{Re}(E_{1+}^{3/2}/M_{1+}^{3/2})$ are routinely used to present the relative magnitude of the amplitudes of interest. Non-vanishing resonant quadrupole amplitudes will signify the presence of non-spherical components in either the proton or in the $\Delta^+(1232)$, or more likely at both; moreover, their Q^2 evolution is expected to provide insight into the mechanism that generate them.

In the constituent-quark picture of hadrons, the non-spherical amplitudes are a consequence of the non-central, color-hyperfine interaction among quarks [30]. However, it has been shown that this mechanism only provides a small fraction of the observed quadrupole signal at low momentum transfers, with the magnitudes of this effect for the predicted E2 and C2 amplitudes [2] being at least an order of magnitude too small to explain the experimental results and with the dominant M1 matrix element being $\simeq 30\%$ low [2]. A likely cause of these dynamical shortcomings is that the quark model does not respect chiral symmetry, whose spontaneous breaking leads to strong emission of virtual pions (Nambu-Goldstone bosons) [29]. These couple to nucleons as $\vec{\sigma} \cdot \vec{p}$, where $\vec{\sigma}$ is the nucleon spin, and \vec{p} is the pion momentum. The coupling is strong in the p-wave and mixes in nonzero angular-momentum components. Based on this, it is physically reasonable to expect that the pionic contributions increase the M1 and dominate the E2 and C2 transition matrix elements in the low- Q^2 (large distance) domain. This was first indicated by adding pionic effects to quark models [31], subsequently shown in pion cloud model calculations [22, 24], and recently demonstrated in chiral effective field theory calculations [28, 32]. Our current understanding of the nucleon suggests that at low- Q^2 (large distance) the pionic cloud effect dominates while at high- Q^2 (short distance) intra-quark forces dominate.

Recent high precision experimental results [3, 4, 5, 6, 7, 8, 9, 10, 11, 12, 13, 15, 16, 17, 18, 19, 20] are in reasonable agreement with predictions of models suggesting the presence of non-spherical amplitudes and in strong disagreement with all nucleon models that assume sphericity for the proton and the Δ . With the existence of these components well established, recent investigations have focused on understanding the various mechanisms that could generate them. Dynamical reaction models with pion cloud effects [22], [23] bridge the constituent quark models gap and are in qualitative agreement with the Q^2 evolution of the experimental data. These models calculate the resonant channels from dynamical equations; they account for the virtual pion cloud contribution dynamically but have an empirical parametrization of the inner (quark) core contribution which gives them some flexibility in the observables. They find that a large fraction of the quadrupole multipole strength arises due to the pionic cloud with the effect reaching a maximum value in the region $Q^2 = 0.10 (GeV/c)^2$ (see Fig. 53). Results from effective field theoretical (chiral) calculations [28, 32], solidly based on QCD, can also successfully account for the magnitude of the effects giving further

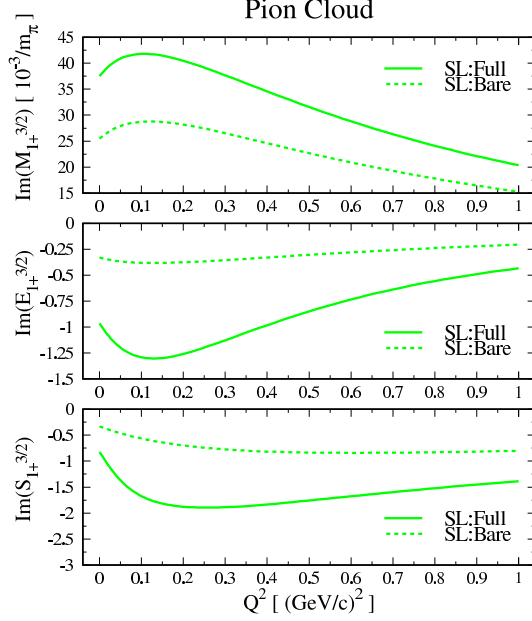


Figure 53: The effect of the pionic cloud to the resonant amplitudes as predicted by the Sato-Lee calculation [22]. Solid line includes the pion cloud contribution while the dashed line neglects the pion cloud effect.

credence to the dominance of the meson cloud effect in the low Q^2 region. Recent results from lattice QCD [21] are also of special interest since they are for the first time accurate enough to allow a comparison to experiment. The chirally extrapolated [28] values of CMR and EMR are found to be nonzero and negative in the low Q^2 region, in qualitative agreement with the experimental results, thus linking the experimental evidence for the non-spherical amplitudes directly to QCD while highlighting the importance of future lattice calculations using lighter quark masses and further refining the chiral extrapolation procedure.

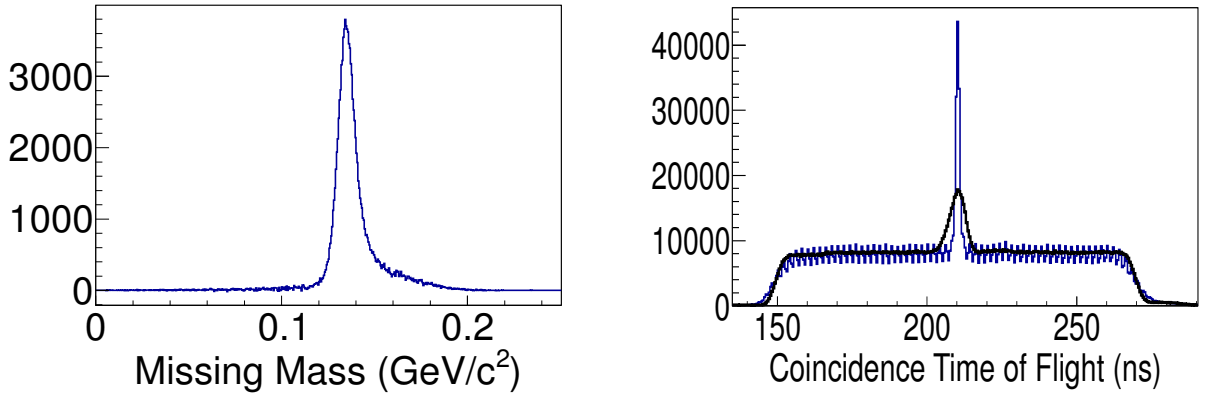


Figure 54: Left panel: The missing mass spectrum for the reconstructed (undetected) pion after the subtraction of accidentals. Right panel: Raw and corrected coincidence Time of Flight spectrum; an excellent timing resolution of 1.6 ns has been achieved after the ToF corrections.

3.10.2 The Experiment

The E08-010 experiment aim to explore the low momentum transfer region at the nucleon - $\Delta(1232)$ transition, where the pionic cloud effects are expected to dominate. The experiment ran in February and March of

2011 and achieved all the quantitative and qualitative goals of the experiment proposal. High precision measurements of the $p(e, e'p)\pi^0$ excitation channel were provided. The two High Resolution Spectrometers were utilized to detect in coincidence electrons and protons respectively while the 6 cm and 15 cm liquid hydrogen targets and an electron beam of $E_o = 1.15 \text{ GeV}$ at $75 \mu\text{A}$ were used throughout the experiment. High precision measurements were conducted in the $Q^2 = 0.04 \text{ (GeV/c)}^2$ to 0.13 (GeV/c)^2 range. The experiment will offer results of unprecedented precision in the low momentum transfer region and will extend the knowledge of the Coulomb quadrupole amplitude lower in momentum transfer. Furthermore these measurements will resolve observed discrepancies between measurements of other labs. Two parallel analysis efforts are currently in progress, by Temple University and St. Mary's University, in order to provide important cross checks throughout all the steps of the analysis. The analysis stage involving calibrations has been completed. In Fig. 54 the Missing Mass spectrum (after background subtraction), corresponding to the undetected pion, as well as the corrected time of flight spectrum are presented. An excellent timing resolution of 1.6 ns has been achieved. Currently the effort has moved on to the kinematical phase space analysis, the extraction of the spectrometer cross sections and the extraction of the resonant amplitudes. In Fig. 55 the measured cross section is presented for the parallel cross section measurement at the highest momentum transfer kinematics of this experiment. The cross section measurements will allow for the extraction of CMR with unprecedented precision at the low momentum transfer region. The projected uncertainties for the CMR are presented in Fig. 56. The new results will allow an in depth exploration of the nucleon dynamics, offering a very precise signature of the pion cloud, and will provide strong constraints to modern theoretical calculations that will in turn allow for a more complete understanding of the nucleon structure.

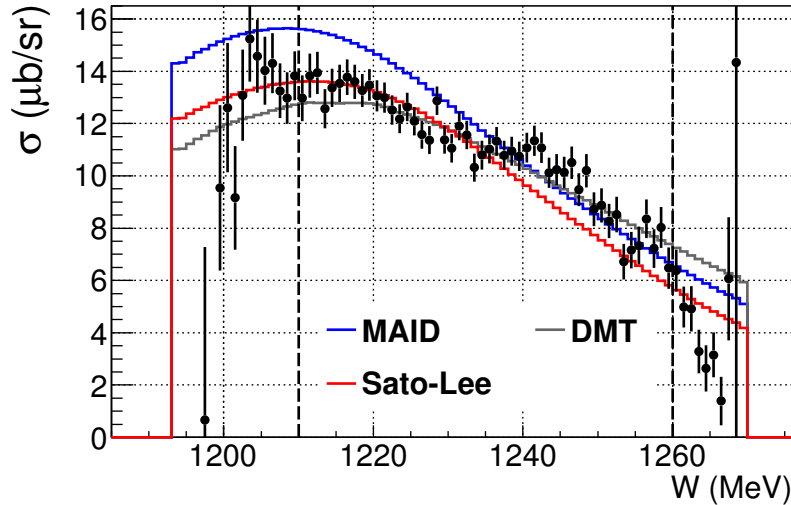


Figure 55: The measured cross section is presented for the parallel cross section measurement at $Q^2 = 0.125 \text{ (GeV/c)}^2$.

References

- [1] A. de Rujula, H. Georgi and S.L. Glashow *et al.*, *Phys. Rev* **D12**, 147 (1975).
- [2] N. Isgur, G. Karl and R. Koniuk, *Phys. Rev.* **D25**, 2394 (1982); S. Capstick and G. Karl, *Phys. Rev.* **D41**, 2767 (1990).
- [3] G. Blanpied *et al.*, *Phys. Rev. Lett.* **79**, 4337 (1997).

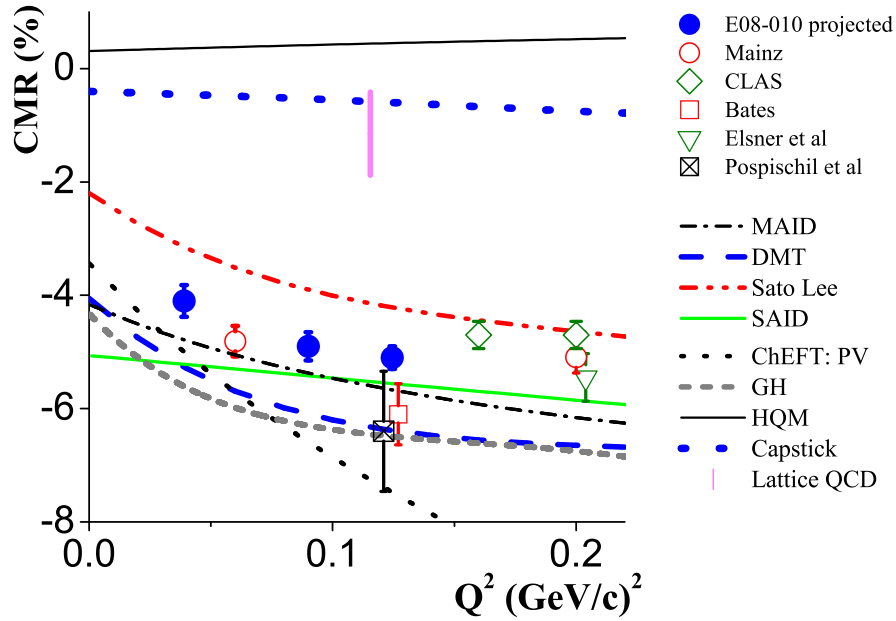


Figure 56: The CMR at the low momentum transfer region. The projected E08-010 uncertainties are presented along with the world data and the theoretical model predictions

- [4] R. Beck *et al.*, Phys. Rev. Lett. **78**, 606 (1997);
 ibid. 79, 4515 (1997) (Erratum).
 R. Beck *et al.*, Phys. Rev. **C61**, 35204 (2000).
- [5] V.V. Frolov *et al.*, Phys. Rev. Lett. **82**, 45 (1999).
- [6] T. Pospischil *et al.*, Phys. Rev. Lett. **86**, 2959 (2001).
- [7] C. Mertz *et al.*, Phys. Rev. Lett. **86**, 2963 (2001).
- [8] P. Bartsch *et al.*, Phys. Rev. Lett. **88**, 142001 (2002).
- [9] L.D. van Buuren *et al.*, Phys. Rev. Lett. **89**, 12001 (2002).
- [10] N.F. Sparveris *et al.*, Phys. Rev. Lett. **94**, 022003 (2005).
- [11] J.J. Kelly *et al.*, Phys. Rev. Lett. **95**, 102001 (2005).
- [12] N.F. Sparveris *et al.*, Phys. Lett. **B 651**, 102 (2007).
- [13] S. Stave *et al.*, Eur. Phys. J. **A 30**, 471 (2006).
- [14] D. Elsner *et al.*, Eur. Phys. J. **A 27** 91-97 (2006).
- [15] K. Joo *et al.*, Phys. Rev. **C68**, 032201 (2003); K. Joo *et al.*, Phys. Rev. **C70**, 042201 (2004)
- [16] S. Stave, N. Sparveris *et al.*, Physical Review **C78**, 025209 (2008)
- [17] M. Ungaro *et al.*, Phys. Rev. Lett. **97**, 112003 (2006).
- [18] A. N. Villano *et al.*, Phys. Rev. C **80**, 035203 (2009)
- [19] I.G. Aznauryan *et al.* Phys. Rev. C **80**, 055203 (2009)

- [20] N. Sparveris *et al.*, Eur. Phys. J. **A 49**, 136 (2013).
- [21] C. Alexandrou *et al.*, Phys. Rev **D83** 014501 (2011); Phys. Rev. Lett. **94**, 021601 (2005).
- [22] T. Sato and T.-S.H. Lee, Phys. Rev. **C63**, 055201 (2001).
- [23] S.S. Kamalov and S. Yang, Phys. Rev. Lett. **83**, 4494 (1999)
- [24] S.S. Kamalov *et al.*, Phys. Lett. **B 522**, 27 (2001).
- [25] D. Drechsel *et al.*, Nucl. Phys. **A 645**, 145 (1999).
- [26] D. Drechsel and L. Tiator, J. Phys. **G18**, 449 (1992)
- [27] R.A. Arndt, *et al.* Phys. Rev. **C66**, 055213 (2002); nucl-th/0301068 and <http://gwdac.phys.gwu.edu>
- [28] V. Pascalutsa and M. Vanderhaegen *et al.*, Phys. Rev. Lett. **95**, 232001 (2005) and V. Pascalutsa and M. Vanderhaegen *et al.*, Phys. Rev. **D73**, 034003 (2006).
- [29] A.M. Bernstein, Eur. Phys. J. **A 17**, 349 (2003).
- [30] S.L. Glashow, Physica A **96**, 27 (1979)
- [31] D.H. Lu, A.W. Thomas, A.G. Williams, Phys. Rev. **C55**, 3108 (1997); U. Meyer, E. Hernandez, A.J. Buchmann, Phys. Rev. **C64**, 035203 (2001); M. Fiolhais, B. Golli, S. Sirca, Phys. Lett. **B 373**, 229 (1996)
- [32] T. A. Gail and T. R. Hemmert, Eur. Phys. J. **A 28** (1), 91-105 (2006)

3.11 E08-011: \vec{e}^- - ^2H Parity Violating Deep Inelastic Scattering (PVDIS) at CEBAF 6 GeV

R. Michaels, P.E. Reimer, X. Zheng, spokespersons,
K. Pan, D. Wang, graduate students,
and
the Hall A Collaboration.
contributed by R. Michaels

In the past year, our collaboration has published three journal articles to document the results of our 2009 run [1, 2, 3]. The DAQ, trigger, detectors, PID, and deadtime corrections were documented in detail in ref [1]. The measurements in the resonance region were published in [2] and compared to models; this was the first parity-violating data covering the full resonance region, and the result showed that quark-hadron duality holds true, at the several percent level, for the electroweak structure functions. Recently, a paper on the main DIS results was accepted by Nature [3]. A fourth and probably final archival paper with many other details is expected to be finished in 2014.

As a reminder, the experiment measured the parity violating asymmetry of \vec{e}^- - ^2H deep inelastic scattering (PVDIS). A simple formula which neglects sea quarks and radiative corrections is

$$A_{PV}^{DIS} \approx \frac{3G_F Q^2}{10\sqrt{2}\pi\alpha} [(2C_{1u} - C_{1d}) + Y_3(2C_{2u} - C_{2d})] \quad (23)$$

where G_F is the Fermi constant, α is the fine structure constant, Q^2 is the square of the four-momentum transfer (we ran at $Q^2 = 1.1$ and 1.9 $(\text{GeV}/c)^2$), and Y_3 is a kinematic function. The constants “ $C_{(1u),(1d),(2u),(2d)}$ ” are products of the fundamental electroweak coupling constants for up (u) and down (d) quarks; in the Standard model they can be written as simple functions of the Weinberg angle. Consider the first-order Feynmann diagram for the process. The parity violation arises either from axial coupling at the electron vertex (the C_1 terms) or at the quark vertex (the C_2 terms). For details, see ref [3]. While Qweak [4] and other experiments provide precise constraints on the C_1 terms, the unique contribution of the e08011 measurement is an extraction of the C_2 terms. We have improved the precision of the vector-electron axial-vector-quark (VA) interaction term combination $2C_{2u} - C_{2d}$ over the world value [5, 6] by a factor of five.

The main experimental challenges were the high event rate (600 kHz), the pion contamination (controlled at the $< 4 \times 10^{-4}$ level), the deadtime uncertainty ($< 0.4\%$), and the beam polarimetry [$dP/P = (1.2-1.8)\%$] [1, 2, 3]. The success of the experiment bodes well for the 12 GeV DIS parity program, which has similar, though significantly more challenging, experimental issues and goals.

References

- [1] R. Subedi, *et al.*, NIM-A **724**, 90 (2013).
- [2] D. Wang *et al.*, Phys. Rev. Lett **111**, 082501 (2013).
- [3] X. Zhang *et al.*, Nature, in press.
- [4] D. Androic, *et al.*, Phys. Rev. Lett. **111**, 141803 (2013).
- [5] C.Y. Prescott *et al.*, Phys. Lett. **B77**, 347 (1978).
- [6] C.Y. Prescott *et al.*, Phys. Lett. **B84**, 524 (1979).

3.12 E08-014: The $x > 2$ experiment

J. Arrington, D. Day, D. Higinbotham and P. Solvignon, spokespersons,
and
the Hall A Collaboration.
contributed by P. Solvignon and Zhihong Ye.

3.12.1 Motivations

The shell model has been partially successful in describing many features of nuclei such as the structure and energies of the nuclear excited states. However, about 30-40% of the nucleonic strength predicted by the shell model to be in shells below the Fermi level is not seen in the experimental data [1]. This missing strength is thought to be due to the nucleon-nucleon (NN) interaction at short distances and the fact that the close packing of nucleons in nuclei results in a significant probability of overlapping nucleon wavefunctions. These overlapping nucleons belong to a short range correlated cluster and exhibit high momenta, well above the Fermi momentum in the nucleus [2].

Short-range correlations (SRC) are now well accepted as a key ingredient in the formulation of realistic nuclear wave functions. This means that the experimental characterization of SRC is crucial to the development of accurate nuclear structure calculations. Recent results from JLab experiment E01-015 [3] confirmed the overwhelming dominance of the proton-neutron pairs in two-nucleon SRCs. These two-nucleon knockout experiments are very sensitive to the isospin structure as they are able to measure both pp and pn correlations. However, they have also to deal with potentially large final state interactions which plague coincidence measurements at high missing momentum.

Although inclusive scattering is typically isospin-blind, isospin sensitivity, also called “tensor dominance”, can be identified through a careful choice of complementary targets. Isospin-independent and isospin-dependent models predict 25% differences in the cross-section ratios of the two medium-weight nuclei, ^{48}Ca and ^{40}Ca . E08-014 complements two-nucleon knockout experiments, for which other physical processes make it difficult to extract a model-independent and precise quantitative measure of the isospin asymmetry. Further insights will be obtained after the JLab 12GeV upgrade from the use of two light mirror nuclei ^3He and ^3H [4]; in addition to further enhanced isospin sensitivity in these light nuclei, realistic theoretical calculations can be performed where the nucleon-nucleon potential components and their amplitudes can be separated.

At $x > 2$, the cross-sections from nuclei heavier than deuterium are expected to be dominated by three-nucleon short-range correlations (3N-SRCs). Results from Hall C experiment E02-019 [5] show a discrepancy with the CLAS results [6] in the $x > 2$ region, while being in very good agreement the 2N-SRC region. E02-019 is at higher Q^2 than CLAS, and this is consistent with the hint of possible Q^2 dependence in the CLAS results (see figure 3 of the original proposal [7]). These new data and observations make our measurement decisive in the effort to map precisely the 3N-SRC region and resolve this new issue. E08-014 will also be the first measurement of isospin dependence of 3N-SRC. The amplitude and properties of SRCs have important implications not only for the structure of the neutron stars and their cooling process [8] but also in the search for neutrino oscillation [9].

3.12.2 Analysis status

JLab experiment E08-014 ran in April-May 2011. This experiment aims at mapping the 2N and 3N-SRC scaling behaviors. It also provides the first test of the SRC isospin dependence in inclusive electron-nucleus scattering by using two Calcium isotopes. This experiment used the standard Hall A high resolution spectrometers configured for electron detection.

The calibrations of all beam diagnostic elements, spectrometer optics and detectors are done and all efficiencies have been evaluated. This past year the analysis efforts were directed on the target density study, complicated by the non-uniformed flow of coolant along the cells. The cooling flow was covering only the upstream half of the cell and therefore the gas/liquid density in this part of the cell was higher than in the downstream half. Also, as expected, this density gradient between the upstream and downstream parts of the cell increases with the beam current. This is mostly an issue for the determination of the target luminosity and the radiative corrections. Data were taken at a range of currents and extrapolated to zero

current to determine the overall density change due to beam heating, while the z-dependence of the density as observed from the data is replicated in the simulation to account for the varying density. The cross section are generated versus the variable x_{bj} with each bin being an average over the target length, i.e. x_{bj} does not depend on the vertex position. However the radiative corrections depend on the location of the reaction. The density distribution along the cell was extracted by fitting the vertex spectra of each cell and then fed into the Monte Carlo simulation to determine the radiative correction factor related to the vertex position.

The analysis of E08-014 is in its final stage for the isospin study with the data on ^{40}Ca and ^{48}Ca . The iteration of the cross section model (Hall C XEM model) has been carried on in order to fit our kinematical region. Corrections for the Coulomb distortion [10] have to be added to the analysis. Then the radiative corrections and cross section model iteration procedure will be finalized. Preliminary results on the isospin ratio are shown in Fig. 57. Recent theoretical work predicts that the probability to find a np pair is the same in ^{40}Ca and in ^{48}Ca [11].

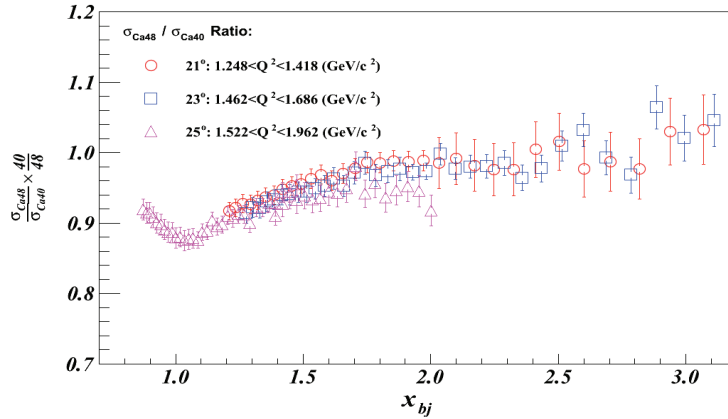


Figure 57: Preliminary results (statistical errors only) on the isospin ratio, i.e. per-nucleon cross section ratio $^{48}\text{Ca}/^{40}\text{Ca}$. Theoretical calculation [11] predicts this ratio to be one in the 2N-SRC region.

For the 2N-SRC and 3N-SRC measurements, special care needs to be taken for these data because of the non-uniformity of the ^2H , ^3He and ^4He target density.

References

- [1] L. Lapikas, Nucl. Phys. **A553**, 297c (1993).
- [2] L.L. Frankfurt, M.I. Strikman, D.B. Day, M. Sargsian, Phys. Rev. C **48**, 2451 (1993).
- [3] R. Shneor *et al*, Phys. Rev. Lett. **99**, 072501 (2007).
- [4] P. Solvignon, J. Arrington, D.B. Day, D. Higinbotham *et al.*, Jefferson Lab experiment E12-11-112.
- [5] N. Fomin *et al*, Phys. Rev. Lett. **108** 092502 (2012).
- [6] K.S. Egiyan *et al*, Phys. Rev. Lett. **96**, 082501 (2006).
- [7] P. Solvignon, J. Arrington, D.B. Day, D. Higinbotham *et al.*, Jefferson Lab experiment E08-014.
- [8] L.L. Frankfurt, M. Sargsian, M.I. Strikman, Int. J. Mod. Phys. **A23** 2991-3055 (2008).
- [9] M. Martini *et al*, Phys. Rev. C **80** 065501 (2009).
- [10] P. Solvignon, D. Gaskell, J. Arrington, AIP Conf. Proc. **1160** 155 (2009)
- [11] M. Vanhalst, J. Ryckebusch and W. Cosyn, Phys. Rev. C **86**, 044619 (2012)

3.13 E08-027: g_2^p

A. Camsonne, J.P. Chen, D. Crabb, K. Slifer, spokespersons,
and
the Hall A Collaboration.
contributed by M. Cummings

3.13.1 Motivation

The deviation of the nucleon's spin dependent properties from point like behavior in inclusive electron scattering can be described by the spin structure functions (SSF) g_1 and g_2 . While g_1 can be expressed in terms of quark distribution functions, g_2 contains contributions from higher order interactions, and so has no simple interpretation in the quark-parton model. Measurements of g_2 for the proton, specifically at low to moderate Q^2 , are scarce; currently, the lowest momentum transfer investigated is 1.3 GeV^2 , by the RSS collaboration [1].

The data from this experiment will provide insight on several outstanding physics puzzles, such as why Chiral Perturbation Theory (χ PT) calculations fail to predict the behavior of the longitudinally-transverse spin polarizability (δ_{LT}) for the neutron [3]; a surprising outcome as δ_{LT} is seen as a good test of QCD dynamics due to its insensitivity to the delta resonance [4, 5, 6]. Additionally, they will provide a test of the Burkhardt-Cottingham Sum rule, which says that the integral of g_2 over the Bjorken scaling variable x is zero. This sum rule has been tested for the neutron, but the lack of data for g_2^p leaves this sum rule largely untested for the proton. Furthermore, a lack of knowledge of the SSF at low Q^2 is a limiting factor of QED calculations of bound-state systems, such as the hydrogen atom. The energy levels of the hydrogen atom can be measured to very high accuracy, to the point where the leading uncertainty of the corresponding QED calculations comes from the finite size of the nucleon as characterized by the SSF and elastic form factors. Finally, recent results from PSI [2] for the proton charge radius $\langle R_p \rangle$ via measurements of the lamb shift in muonic hydrogen suggest a discrepancy from the value obtained from elastic electron-proton scattering. The leading uncertainty in these calculations comes from differing values of the Zemach radius, determined from integrals of the SSF and elastic form factors.

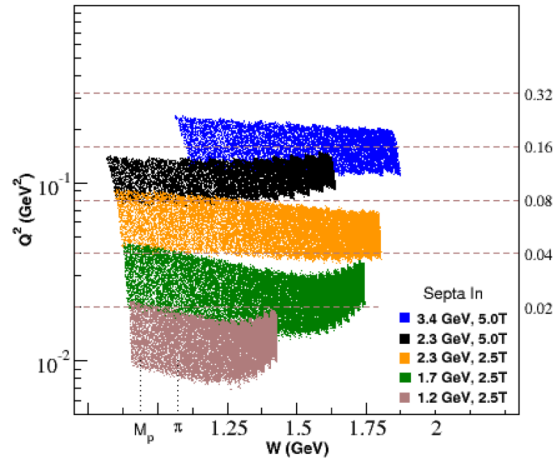


Figure 58: Achieved kinematic coverage during the experimental run period. The vertical axis on the right hand side is the extrapolation to constant Q^2 .

3.13.2 The Experiment

The g_2^p experiment collected data successfully from March-May of 2012. An inclusive measurement was performed in the low Q^2 region $0.02 < Q^2 < 0.20 \text{ GeV}^2$ (see figure 58) at forward angles to obtain the

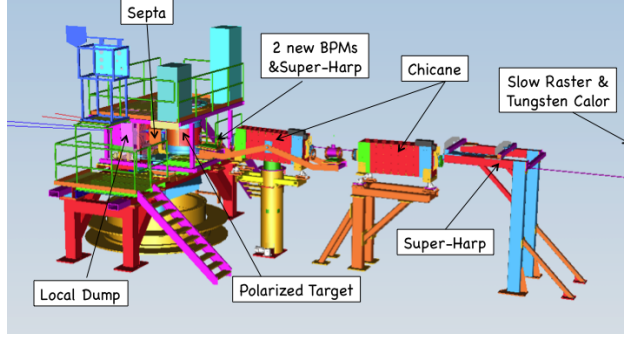


Figure 59: Installation of the g_2^p experiment in Hall A. The third arm detector was located on the left-hand side of the bottom target platform.

proton spin-dependent cross sections. From these data the g_2^p structure function will be extracted along with the longitudinally-transverse spin polarizability δ_{LT} . This experiment required a large scale installation in Hall A, as shown in figure 59. A solid ammonia target was polarized through the process of Dynamic Nuclear Polarization (DNP). In order to compensate for the deflection of the beam by the large target magnetic field, a pair of chicane magnets was installed upstream of the target. To reach the small scattering angle of 5.69° necessary for this kinematic range, a septum magnet was installed downstream of the target. New beamline diagnostics (BPM and BCM) were required due to the low beam current (50-100nA) needed throughout the run to maintain the target polarization. For certain kinematics, a local beam dump was necessary, located just downstream of the septum magnets. Finally, a new scintillator detector, the third arm, was developed specifically for this experiment as a cross check of the product of the beam and target polarization. The third arm was placed on the target platform to collect elastically scattered protons at large scattering angles to provide a measurement of the elastic proton asymmetry.

3.13.3 Status of Analysis

HRS Detector efficiencies are needed as a correction to the cross section. The VDCs provide tracking information for both arms of the HRS, which provides good position and angle reconstruction. However, due to the high event rate, it is possible that multiple particles will pass through the drift chambers simultaneously; as many as 30% of events can have multiple track for certain kinematic settings. This presents a large uncertainty to the cross section if left uncorrected. The multitrack events are carefully examined and resolved, bringing the systematic uncertainty down to below $\sim 1\%$ for all kinematic settings. The total VDC efficiency can be seen in figure 60. Efficiencies from the other spectrometer detectors, including the s1 and s2m trigger scintillators, gas Cherenkov, and lead glass calorimeters were seen to be high ($\sim 99\%$ or higher) throughout the run, indicating good detector performance. PID cuts were determined to minimize the amount of residual pion contamination and maintain an overall detection efficiency of 99%.

The optics calibration without target field has been updated to include beam positions obtained from fitting the focal plane data. Forward and reverse transport functions between the target and focal plane, used to describe the magnetic field system without the target field, were fitted with simulation data from the SNAKE Model. These functions have been incorporated into the g_2^p simulation package to describe the trajectories of outgoing electrons. A comparison between simulation results and optics data at the target plane is being done; the quantities match well, but more tuning to refine the comparison results is currently underway. Additionally, efforts are being focused on optics analysis with the target field on. Due to problems with the right-HRS septum magnet during the run, multiple calibrations will be needed to correspond to the different magnet coil configurations.

A Monte-Carlo simulation program was developed to simulate the affect of the target and septum fields in combination with the HRS. The program is based on the Hall A Single Arm Monte-Carlo (SAMC) package and is extended to work with the target field. The simulation setup has been tuned with our experimental configuration, including two target field settings and several different versions of the septum field model.

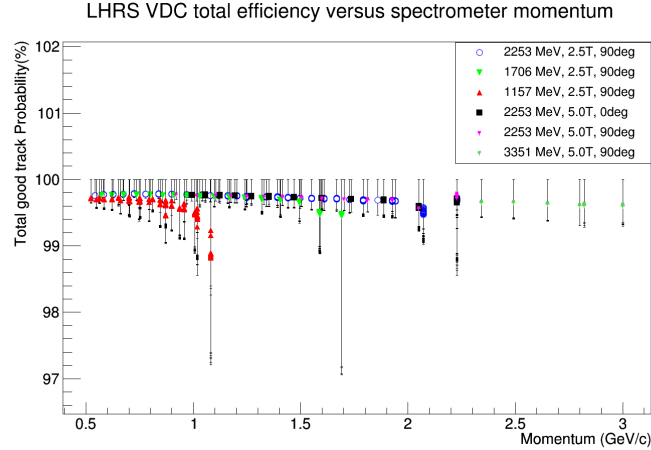


Figure 60: Total VDC efficiency for all LHRs runs, after multitrack events have been accounted for. The efficiency is $> 99\%$ for most kinematic settings.

The programs also include several different cross section models and fittings in the elastic and resonance kinematic regions. The package will be used in the optics calibration with target field and the spectrometer acceptance study.

Beam position information is very important for optimization of the optics. For the straight through calibration, two harps were used to determine the position of the beam. During the course of the run, the BPMB division (attenuation) was changed; present efforts are focused on determining a different calibration method to account for this change. Additionally, a study is underway to understand and account for the fluctuation of the pedestal throughout the run period. The g_2^p experiment is using the same helicity scheme set up by the QWEAK experiment. Both the helicity flip rate and the DAQ rate are high, so a new standalone package was developed to decode the helicity information under these conditions.

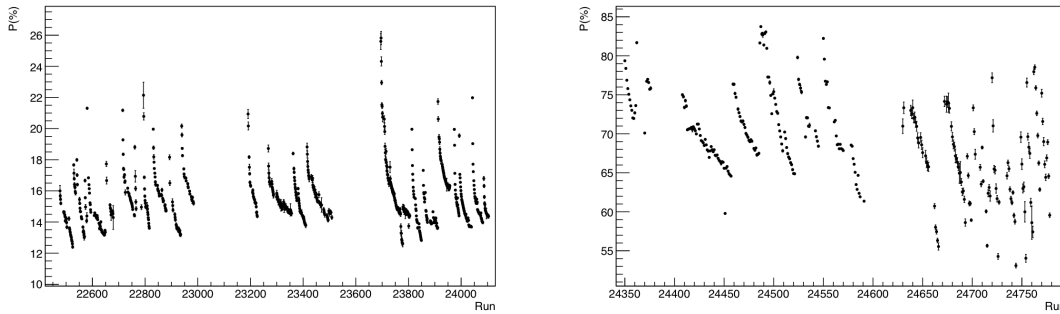


Figure 61: Run by run polarization results for the 2.5T magnetic field setting (**left**) and 5T magnetic field setting (**right**).

A precise measurement of the target polarization is needed to extract the physics asymmetry. During this experiment two different target fields, 2.5T and 5T, were necessary to achieve the desired kinematic range. The calibration constants, used to convert the measured NMR signal into a useable polarization, have been calculated for all ammonia samples and applied to the data to determine the average polarization on a run-by-run basis. The final run polarizations can be seen in figure 61. An average polarization of 70% for the 5T field setting and 15% for the 2.5T field setting were observed. Polarization uncertainties due to measurement precision and statistical fluctuations have been calculated to less than 5%.

Once beam position calibrations, optics with target field and acceptance studies have been completed, the

cross section can be extracted. Studies are underway to calculate the packing fraction and dilution factor, which will determine the percentage of electrons that were not scattered from a proton in the ammonia target. Analysis of data taken with the third arm, which will be used as a cross check of the beam and target polarization, is also in progress. Preliminary physics asymmetries and yields can be seen in figure 62.

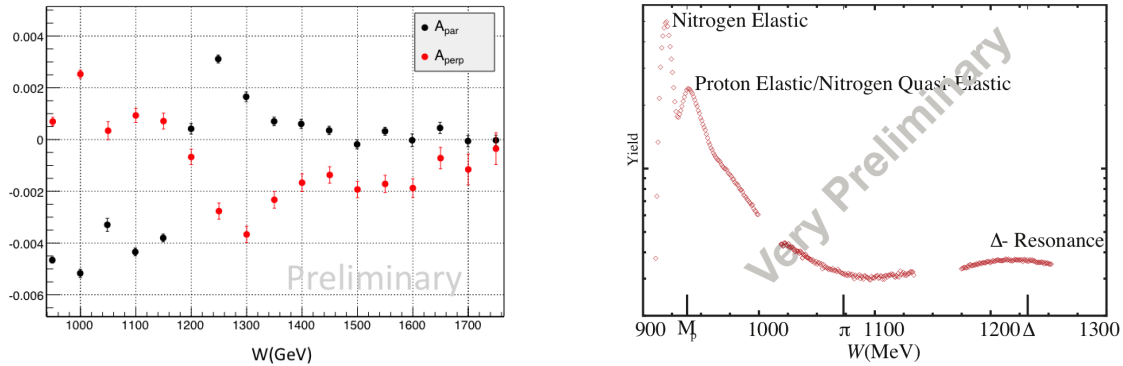


Figure 62: **Left:** Preliminary physics asymmetries for the longitudinal and transverse magnetic field setting. **Right:** Preliminary yields showing the nitrogen and proton elastic peaks.

References

- [1] F. R. Wesselmann *et al.* [RSS Collaboration], Phys. Rev. Lett. **98**, 132003 (2007).
- [2] R. Pohl *et al.*, Nature **466**, 213 (2010).
- [3] M. Amarian *et al.* [Jefferson Lab E94010 Collaboration], Phys. Rev. Lett. **93**, 152301 (2004).
- [4] V. Bernard, T. R. Hemmert and U. G. Meissner, Phys. Lett. B **545**, 105 (2002).
- [5] C. W. Kao, T. Spitzenberg and M. Vanderhaeghen, Phys. Rev. D **67**, 016001 (2003).
- [6] V. Bernard, E. Epelbaum, H. Krebs and U. G. Meissner, arXiv:1209.2523v1 [hep-ph] (2012).

3.14 The Super Bigbite Spectrometer

Progress by the Super Bigbite Collaboration

contributed by S. Riordan
for the Super Bigbite Collaboration.

This a summary of the progress on the DOE funded SBS Project as well as the many separate dependencies, experiments using the same equipment, and collaborative efforts.

3.14.1 Overview

The Super Bigbite (SBS) project is a collection of experiments based around utilizing large-acceptance single dipole spectrometers designed to operate in a high rate environment in conjunction with the upgraded 12 GeV CEBAF accelerator. The types of experiments this is suited for typically require high statistics but only moderate momentum resolution and may either be coincidental electron-hadron scattering (requiring two arms) or single-arm inclusive. The experimental program as a DOE project is formally defined by three high Q^2 elastic form factor measurements, specifically G_E^p/G_M^p , G_E^n/G_M^n , G_M^n , but the collaborative effort also includes A_1^n and SIDIS using a $^3\overline{\text{He}}^7$ target. These experiments are

- E12-07-109, GEp
- E12-09-016, GEn
- E12-09-019, GMn
- E12-09-018, SIDIS
- E12-06-122, A_1^n .

This program is addressing an important part of the Jefferson Lab's 12 GeV goals. It pushes the boundaries of previous high momentum-transfers and large Bjorken- x with what is now kinematically accessible with the 11 GeV beam in Hall A and allows for many tests of theoretical models describing fundamental nucleon structure. In particular, these tests aim towards understanding the nucleon in non-perturbative QCD, mapping out the non-perturbative to perturbative transition, and relating to fundamental questions about the role of angular momentum in nucleon structure.

Over the last year there have been many developments including progress on new hardware systems and structuring of the collaboration. More documentation over the entirety of the project can be found online [\[1\]](#).

3.14.2 Organization

The SBS Collaboration has been formally organized with the adoption of a charter and consists of the overlap of collaborations of experiments using all or parts of the equipment of SBS. This includes those beyond the experiments in the formal DOE project. The coordinating committee for the collaboration consists of two program scientists, the Hall A leader, and a representative from each experiment, one of which acting as the chair. This body consists of

- Gordon Cates, UVA, Program Scientist
- Evaristo Cisbani, INFN, GEp Representative
- Cynthia Keppel, JLab, Hall Leader
- Nilanga Liyanage, UVA, A_1^n Representative
- Andrew Puckett, UConn, SIDIS Representative
- Seamus Riordan, UMass Amherst, GEn Representative
- Brian Quinn, CMU, GMn Representative and Chair

- Bogdan Wojtsekhowski, JLab, Principle Program Scientist

Additionally, outside of the collaboration, in 2014 Mark Jones of Jefferson Lab will replace John LeRose as Project Manager.

3.14.3 Instrumentation Progress

3.14.3.1 48D48 Magnet One critical component of the SBS project is the 48D48 magnet, which serves as the magnetic element for the hadronic arm of these experiments. In the last year, considerable progress has been made in acquiring the existing magnet, designing the iron and coil configuration, as well as simulating magnetic characteristics. The existing magnet iron was acquired from Brookhaven in August. A contract to construct a new power supply was awarded and new coils for the magnet have been ordered. Drawings for the modification of the iron yoke have also been completed. Commissioning of the magnet and power supply is expected to begin later in 2014.

Numerous TOSCA magnetic field simulations have been performed, including analysis of the full magnetic systems of Bigbite and Super Bigbite. These studies are ongoing. This magnetic shielding is particularly important, as the magnet will be situated near the target areas as well as have beamline components run through it when at small angles. Field maps from these simulations have become available and can now be included within detailed Geant4 simulations of backgrounds and counting rates.

3.14.3.2 GEM Detectors Several sets of GEM detectors are being constructed by groups at INFN and UVA and will be used in both the hadron and electron arms of these experiments. In the last year, two full sized $50 \times 50 \text{ cm}^2$ chambers have been built at UVA and one was successfully tested at Fermilab as well as several prototype chambers which have been thoroughly tested with cosmic rays. The UVA contract to produce the first 29 modules was awarded and orders for the GEM components have been placed.

The INFN collaboration has assembled three $40 \times 50 \text{ cm}^2$ “pre-final” modules and have been performing in-beam tests at DESY in magnetic fields up to 500 Gauss. Two full chambers are expected to be produced by the end of 2014. Orders for all GEM components and electronics have been placed.

Testing of two APV25 readout systems are being carried out, using a stand-alone SRS (scalable readout system) at UVA or the VME-based INFN MPD system.

The INFN group is also working on the development of two small silicon microstrip planes ($10 \times 20 \text{ cm}^2$, $50 \mu\text{m}$ pitch) which could improve the tracking of the primary particles in the front tracker. Impact of these silicon planes on the SBS tracking is under careful evaluation.

3.14.3.3 Calorimetry There are two primary calorimetry projects required to fully realize SBS. This includes the electromagnetic calorimeter for the GEp experiment and the hadronic calorimeter, both outside of the DOE project, which is used in the hadron arm in the coincident trigger experiments.

A primary concern for the electromagnetic calorimeter is the darkening of lead-glass blocks as they absorb radiation. The essence of the sensitivity of the lead glass to radiation is due to the heavy metals in the glass and the low electrical conductivity, which leads to the accumulation of ions. Two curing processes have been used in the past and are under investigation. A UV curing process, which typically requires downtime during running is under investigation by collaborators at William and Mary, Norfolk State University, and Christopher Newport University. Continuous UV curing is one of the goals of the group’s effort, in particular finding the appropriate UV source and filters to eliminate visible light. This group has also studied the possibility of using the sampling calorimeter technology, in the form of shashliks to avoid the problem of radiation damage. A viable solution was arrived at, but the current funding situation precludes its use at the present time.

Additionally, a thermal annealing method which operates continuously is under investigation at JLab. The key elements of the annealing concept have been fully tested and engineering aspects of this system are being developed. The use of low-energy but high intensity accelerators at Idaho State University is planned to irradiate blocks for final proof of the annealing methods.

The hadronic calorimeter, HCal-J, is being designed and prototyped at Carnegie Mellon University with support from INFN Catania and is heading to full construction. A design of optical parts of the modules the wavelength shifter and light guides, has been completed as well a concept for the overall support structure.

Samples of specialized plastic scintillator were obtained to determine an optimal PPO concentration to maximize the light yield and production of this scintillator for the full detector has been funded and initiated. A mechanical prototype module is expected to be completed this January, a complete detailed design in June, and full scale construction beginning later in 2014.

3.14.3.4 Polarized ^3He Target The polarized ^3He target is at the heart of the A_1^n , G_E^n , and SIDIS experiments and provides an effective polarized neutron target and has been employed at the lab for many years with beam currents up to $15\ \mu\text{A}$ with 60% polarization. However to reach sufficient luminosity, beam currents up to $60\ \mu\text{A}$ and extending the length to almost 60 cm presents new challenges. To meet these goals, a design that includes metal end-cap windows, a convection design, and two laser pumping chambers is being developed at UVA. In the last year, progress has been made in prototyping this target, in particular testing different glass-to-metal seals which will still maintain high-quality polarization. Additionally, progress has been made in developing a target chamber and holding coils with < 0.1 Gauss/cm field gradient, which is also crucial to achieve high polarization.

3.14.3.5 Gas Cherenkov A 600 PMT gas Cherenkov detector to be used for electron identification is being developed jointly by collaborators at William and Mary, North Carolina A&T State University, University of Glasgow, and James Madison University. Full-scale simulations and a small-scale prototyping is completed and the detector geometry has been frozen. Prototyping of the mirror frame and forming the mirror shape have been completed and development for an LED-based alignment system is also completed. Fabrication and testing will occur in early 2014. A particularly detailed Geant4 simulation has also been developed at William and Mary to study light collection efficiencies down to the PMT level.

In additional particular efforts were made to optimize the design of the PMT array, which requires magnetic shielding. A prototype mu-metal and iron box was produced and tested by North Carolina A&T State University which will allow for $< 10\%$ change of gain in a 30 Gauss environment which was consistent with expectations. James Madison University will be testing the phototubes to be used and front-end electronics are being developed by University of Glasgow.

3.14.3.6 Coordinate Detector A scintillator coordinate detector will serve as a hodoscope to determine the electron position in front of the electromagnetic calorimeter in the GEp experiment. The position resolution of such a detector will allow for a much cleaner identification of proton elastic events than by the calorimeter alone by exploiting the specific electron-hadron kinematic correlation. It consists of two detector planes of $0.5 \times 3 \times 102\ \text{cm}^3$ horizontal scintillator bars split into left and right halves. A set of multi-anode PMTs from FNAL were donated to Jefferson Lab in 2012 and have been tested by collaborators at Saint Mary's University in Halifax for uniformity on gain between pixels. Front-end electronics based on the NINO discriminator chips is being developed at University of Glasgow. Last summer a prototype module was constructed and will be used for mechanical construction tests.

3.14.3.7 Monte Carlo The Geant4 and ROOT-based SBS Monte Carlo simulation, `g4sbs`, included realizing a fully detailed representation of the experiment geometry. In particular, recent descriptions of the 48D48 magnet coil and shielding, cryotarget, and detector stacks were included. The code is now hosted on github [2].

References

- [1] <http://hallaweb.jlab.org/12GeV/SuperBigBite/>
- [2] <https://github.com/JeffersonLab/g4sbs>

4 Publications

Publications published during 2013, either in preprint or finally, based on experiments run in Hall A of Jefferson Lab.

1. Monaghan, P. *et al.*, Measurement of the $^{12}\text{C}(e,e'p)^{11}\text{B}$ Two-Body Breakup Reaction at High Missing Momentum Values, [arxiv:1301.7027](#)
2. Wang, D. *et al.*, Measurement of the Parity-Violating Asymmetry in Electron-Deuteron Scattering in the Nucleon Resonance Region, *Phys.Rev.Lett.* **111** 082501
3. Pomerantz, I. *et al.*, Hard Two-body Photodisintegration of ^3He , *Phys.Rev.Lett.* **110** 242301
4. Wang, Y. *et al.*, A MRPC prototype for SOLID-TOF in JLab, *JINST* **8** P03003
5. Horowitz, C.J. *et al.*, Electroweak Measurements of Neutron Densities in CREX and PREX at JLab, USA, [arxiv:1307.3572](#)
6. Singh, J. *et al.*, The Development of High-Performance Alkali-Hybrid Polarized He-3 Targets for Electron Scattering [arxiv:1309.4004](#)
7. Camsonne, A. *et al.*, JLab Measurement of the ^4He Charge Form Factor at Large Momentum Transfers, [arxiv:1309.5297](#)
8. Katich, J. *et al.*, Measurement of the Target-Normal Single-Spin Asymmetry in Deep-Inelastic Scattering from the Reaction $^3\text{He}^\uparrow(e, e')X$, [arxiv:1311.0197](#)
9. Subedi, R. *et al.*, A scaler-based data acquisition system for measuring parity-violating asymmetry in deep inelastic scattering, *Nucl. Instr. Meth. A* **724** (2013) 90-103
10. Parno, D. *et al.*, Comparison of Modeled and Measured Performance of a GSO Crystal as Gamma Detector, *Nucl. Instr. Meth. A* **728**, 92-96
11. Allada, K. *et al.*, Single Spin Asymmetries of Inclusive Hadrons Produced in Electron Scattering from a Transversely Polarized ^3He Target, [arxiv:1311.1866](#)
12. Zhang, Y. *et al.*, Measurement of pretzelosity asymmetry of charged pion production in Semi-Inclusive Deep Inelastic Scattering on a polarized ^3He target, [arxiv:1312.3047](#)

5 Theses

1. *Measurement of the Neutron Radius of ^{208}Pb Through Parity Violation in Electron Scattering*
Kiadtisak Saenboonruang
https://misportal.jlab.org/ul/publications/view_pub.cfm?pub_id=12303
2. *Short Range Correlations in Nuclei at Large x_{bj} through Inclusive Quasi-Elastic Electron Scattering*
Zhihong Ye
https://misportal.jlab.org/ul/publications/view_pub.cfm?pub_id=12877

6 Hall A Collaboration Member List, 2013

Argonne National Lab

John Arrington
Paul Reimer
Xiaohui Zhan

Brookhaven National Lab

Xin Qian

Budker Institute of Nuclear Physics

Dima Nikolenko
Igor Rachek

Cairo University

Hassan Ibrahim

California State University

Konrad A. Aniol
Martin B. Epstein
Dimitri Margaziotis

Carnegie Mellon University

Gregg Franklin
Vahe Mamyasyan
Brian Quinn

The Catholic University of America

Marco Carmignotto
Tanja Horn
Indra Sapkota

Commissariat à l'Energie Atomique - Saclay

Maxime Defurne
Nicole d'Hose
Eric Fuchey
Franck Sabatie

China Institute of Atomic Energy (CIAE)

Xiaomei Li
Shuhua Zhou

Christopher Newport University

Ed Brash

College of William and Mary

David S. Armstrong
Carlos Ayerbe Gayoso
Todd Averett

Juan Carlos Cornejo

Melissa Cummings
Wouter Deconinck

Keith Griffioen

Joe Katich

Charles Perdrisat

Yang Wang

Huan Yao

Bo Zhao

Duquesne University

Fatiha Benmokhtar

Duke University

Steve Churchwell

Haiyan Gao

Calvin Howell

Min Huang

Richard Walter

Qiuqian Ye

Faculte des Sciences de Monastir (Tunisia)

Malek Mazouz

Florida International University

Armando Acha

Werner Boeglin

Luminiya Coman

Marius Coman

Lei Guo

Hari Khanal

Laird Kramer

Pete Markowitz

Brian Raue

Jeorg Reinhold

Forschungszentrum Rossendorf Institut für Kern- und Hadronenphysik

Frank Dohrmann

Gesellschaft für Schwerionenforschung (GSI)

Javier Rodriguez Vignote

Hampton University

Eric Christy

Leon Cole

Peter Monaghan

Harvard University

Richard Wilson

Hebrew University of Jerusalem

Moshe Friedman

Aidan Kelleher

Guy Ron

Huangshan University

Hai-jiang Lu

XinHu Yan

Idaho State University

Mahbub Khandaker

Dustin McNulty

INFN/Bari

Raffaele de Leo

INFN/Catania

Antonio Guisa

Francesco Mammolit

Giuseppe Russo

Concetta Maria Sutera

INFN/Lecce

Roberto Perrino

INFN/Roma

Marco Capogni

Evaristo Cisbani

Francesco Cusanno

Fulvio De Persio

Alessio Del Dotto

Cristiano Fanelli

Salvatore Frullani

Franco Garibaldi

Franco Meddi

Guido Maria Urciuoli

Institute of Modern Physics, Chinese Academy of Sciences

Xurong Chen

Institut de Physique Nucleaire - Orsay

Camille Desnault

Alejandro Marti Jimenez-Arguello

Carlos Munoz Camacho

Rafayel Paremuzyan

ISN Grenoble

Eric Voutier

James Madison University

Gabriel Niculescu

Ioana Niculescu

Jefferson Lab

Alexandre Camsonne

Larry Cardman

Jian-Ping Chen

Eugene Chudakov

Mark Dalton

Kees de Jager

Alexandre Deur

Ed Folts

David Gaskell

Javier Gomez

Ole Hansen

Douglas Higinbotham

Mark K. Jones

Thia Keppel

John Lerose

Simona Malace

Bert Manzlak

David Meekins

Robert Michaels

Bryan Moffit

Sirish Nanda

Noel Okay

Lubomir Pentchev

Yi Qiang

Lester Richardson

Yves Roblin

Brad Sawatzky

Jack Segal

Dennis Skopik

Patricia Solvignon

Mark Stevens

Riad Suleiman

Stephanie Tysor

Bogdan Wojtsekowski

Jixie Zhang

Jozef Stefan Institute

Miha Mihovilovic

Simon Sirca

Kent State University

Bryon Anderson

Mina Katramatou

Elena Khrosinkova

Richard Madey

Mark Manley

Gerassimos G. Petratos

Larry Selvey

John Watson

Kharkov Institute of Physics and Technology

Oleksandr Glamazdin

Viktor Gorbenko

Roman Pomatsalyuk

Vadym Vereshchaka

Kharkov State University

Pavel Sorokin

Khalifa University

Issam Qattan

Lanzhou University

Bitao Hu

Yi Zhang

Longwood University

Tim Holmstrom

Keith Rider

Jeremy St. John

Vincent Sulkosky

Wolfgang Troth

Los Alamos Laboratory

Jin Huang

Xiaodong Jiang

Ming Xiong Liu

LPC Clermont-Ferrand France

Pierre Bertin

Helene Fonvielle

Mississippi State University

Dipangkar Dutta

Mitra Shabestari

Amrendra Narayan

Nuruzzaman

Massachusetts Institute of Technology

Kalyan Allada

Bill Bertozzi

Shalev Gilad

Navaphon "Tai" Muangma

Kai Pan

Cesar Fernandez Ramirez

Rupesh Silwal

Mountain View Collage

Ramesh Subedi

Negev Nuclear Research Center

Arie Beck

Sharon Beck

NIKHEF

Jeff Templon

Norfolk State University

Wendy Hinton

Vina Punjabi

North Carolina Central University

Benjamin Crowe

Branislav (Branko) Vlahovic

North Carolina A&T State University

Ashot Gasparian

Northwestern University

Ralph Segel

Ohio University

Mongi Dlamini

Norman Israel

Paul King

Julie Roche

Old Dominion University

S. Lee Allison

Gagik Gavalian

Mohamed Hafez

Charles Hyde

Kijun Park

Hashir Rashad

Larry Weinstein

Peterburg Nuclear Physics Institute

Viacheslav Kuznetsov

Regina University

Alexander Kozlov

Andrei Semenov

Rutgers University

Lamiaa El Fassi

Ron Gilman

Gerfried Kumbartzki

Katherine Myers
Ronald Ransome
Yawei Zhang

Saint Norbert College
Michael Olson

Seoul National University
Seonho Choi
Byungwuek Lee

Smith College
Piotr Decowski

St Mary's University
Davis Anez
Adam Sarty

Stony Brook University
Rouven Essig

Syracuse University
Zafar Ahmed
Richard Holmes
Paul A. Souder

Technische Universität München
Jaideep Singh

Tel Aviv University
Nathaniel Bubis
Or Chen
Igor Korover
Jechiel Lichtenstadt
Eli Piasetzky
Ishay Pomerantz
Ran Shneor
Israel Yaron

Temple University
David Flay
Zein-Eddine Meziani
Michael Paolone
Matthew Posik
Nikos Sparveris

Tohoku University
Kouichi Kino
Kazushige Maeda
Teiji Saito
Tatsuo Terasawa
H. Tsubota

Tsinghua University
Zhigang Xiao

Universidad Complutense de Madrid (UCM)
Joaquin Lopez Herraiz
Luis Mario Fraile
Maria Christina Martinez Perez
Jose Udias Moinelo

University of Connecticut
Andrew Puckett

Universitat Pavia
Sigfrido Boffi

University "La Sapienza" of Rome
Cristiano Fanelli
Fulvio De Persio

University of Glasgow
John Annand
David Hamilton
Dave Ireland
Ken Livingston
Dan Protopopescu
Guenther Rosner
Johan Sjoegren

University of Illinois
Ting Chang
Areg Danagoulian
J.C. Peng
Mike Roedelbronn
Youcai Wang
Lindgyan Zhu

University of Kentucky
Dan Dale
Tim Gorringer
Wolfgang Korsch

University of Lund
Kevin Fissum

University of Manitoba
Juliette Mammei

University of Maryland
Elizabeth Beise

University of Massachusetts, Amherst

Krishna S. Kumar
Seamus Riordan
Jon Wexler

University of New Hampshire
Toby Badman
Trevor Bielarski
John Calarco
Bill Hersman
Maurik Holtrop
Donahy John
Mark Leuschner
Elena Long
James Maxwell
Sarah Phillips
Karl Slifer
Timothy Smith
Ryan Zielinski

University of Regina
Garth Huber
George Lolos
Zisia Papandreou

University of Saskatchewan
Ru Igarashi

University of Science and Technology of China (USTC)
Yi Jiang
Wenbiao Yan
Yunxiu Ye
Zhengguo Zhao
Yuxian Zhao
Pengjia Zhu

University of South Carolina
Steffen Strauch

University of Tennessee
Nadia Fomin

University of Virginia
Khem Chirapatpimol
Donal Day
Xiaoyan Deng
Gordon D. Gates
Gu Chao
Charles Hanretty
Ge Jin
Richard Lindgren
Jie Liu
Nilanga Liyanage
Vladimir Nelyubin

Blaine Norum
Kent Paschke
Peng Chao
Oscar Rondon
Kiadtisak Saenboonruang
William “Al” Tobias
Diancheng Wang
Kebin Wang
Zhihong Yi
Zhiwen Zhao
Xiaochao Zheng
Jiayao Zhou

University of Washington

Diana Parno

Yamagata University

Seigo Kato
Hiroaki Ueno

Yerevan Physics Institute

Sergey Abrahamyan
Nerses Gevorgyan
Edik Hovhannisyan
Armen Ketikyan
Samvel Mayilyan
Karen Ohanyan
Artush Petrosyan
Galust Sargsyan
Albert Shahinyan
Hakob Voskanian

Inactive Members

Mattias Anderson
Maud Baylac
Hachemi Benaoum
J. Berthot
Michel Bernard
Louis Bimbot
Tim Black
Alexander Borissov
Vincent Breton
Herbert Breuer
Etienne Burtin
Christian Cavata

George Chang
Nicholas Chant
Jean-Eric Ducret
Zhengwei Chai
Brandon Craver
Natalie Degrande
Rachel di Salvo
Pibero Djawotho
Chiranjib Dutta
Kim Egriyan
Stephanie Escoffier
Catherine Ferdi
Megan Friend
Robert Feuerbach
Mike Finn
Bernard Frois
Oliver Gayou
Charles Glashausser
Jackie Glistler
Greg Hadcock
Brian Hahn
Harry Holmgren
Sebastian Incerti
Mauro Iodice
Riccardo Iommi
Florian Itard
Stephanie Jaminion
Steffen Jensen
Sudirukkuge Tharanga Jinasun-
dera
Cathleen Jones
Lisa Kaufman
James D. Kellie
Sophie Kerhoas
Ameya Kolarkar
Norm Kolb
Ioannis Kominis
Serge Kox
Kevin Kramer
Elena Kuchina
Serguei Kuleshov
Jeff Lachniet
Geraud Lavessiere
Antonio Leone
David Lhuillier

Meihua Liang
Han Liu
Robert Lourie
Jacques Marroncle
Jacques Martino
Kathy McCormick
Justin McIntyre
Luis Mercado
Brian Milbrath
Wilson Miller
Joseph Mitchell
Jean Mougey
Pierre Moussiegt
Alan Nathan
Damien Neyret
Stephane Platchkov
Thierry Pussieux
Gilles Quemener
Abdurahim Rakhman
Bodo Reitz
Rikki Roche
Philip Roos
David Rowntree
Gary Rutledge
Marat Rvachev
Arun Saha
Neil Thompson
Luminita Todor
Paul Ulmer
Antonin Vacheret
Luc Van de Hoorebeke
Robert Van de Vyver
Pascal Vernin
Dan Watts
Krishni Wijesooriya
Hong Xiang
Wang Xu
Jingdong Yuan
Jianguo Zhao
Jingdong Zhou
Xiaofeng Zhu
Piotr Zolnierczuk